LINEAR AND NONLINEAR OPTICAL PROPERTIES OF METAL-DIELECTRIC MULTILAYER STRUCTURES

A Dissertation
Presented to
The Academic Faculty

By

Daniel Owens

In Partial Fulfillment
Of the Requirements for the Degree
Doctor of Philosophy in Electrical Engineering

Georgia Institute of Technology

December 2010

Linear and nonlinear optical properties of metal-dielectric multilayer structures

Approved by:

Dr. Bernard Kippelen, advisor
School of Electrical and Computer Engineering
Georgia Institute of Technology

Dr. Farrokh Ayazi
School of Electrical and Computer Engineering
Georgia Institute of Technology

Dr. David Citrin
School of Electrical and Computer Engineering
Georgia Institute of Technology

Dr. Ken Sandhage
School of Chemistry
Georgia Institute of Technology

Dr. Gee-Kung Chang
School of Electrical and Computer Engineering
Georgia Institute of Technology

Date Approved: August 16, 2010

ACKNOWLEDGEMENTS

The author would first like to thank his wife Sarah, who knew what she was getting into when she married me and did so anyway.

My sincere appreciation goes to my advisor, Prof. Kippelen, for supporting me and keeping me around long enough to finish this work.

Thank you to my committee for taking the time to approve this work.

I am grateful to the Army Evaluation Center, and in particular my supervisor Dr. Brian Hall, for allowing me time to continue writing my dissertation while learning a new job.

This work would not have been possible without the financial support from the NSF through STC-DMR-0120967, ARO through contract/grant 50372-CH-MUR AFOSR (BIONIC Center grant No. FA9550-09-1-0162), and AFOSR (grant No. FA9550-09-1-0418).

Soli Deo Gloria

TABLE OF CONTENTS

LIST OF TABLES

LIST OF FIGURES

LIST OF SYMBOLS

ESA	Excited State Absorption
ITF	Induced Transmission Filter
ITO	Indium Tin Oxide
MDM	Metal-Dielectric-Metal
MDPBG	Metal-Dielectric Photonic Band Gap
MDPC	Metal-Dielectric Photonic Crystal
NLO	Nonlinear Optical
TEM	Transmission Electron Microscopy
THG	Third Harmonic Generation
TTM	Two Temperature Model
TPA	Two Photon Absorption
WLC	White Light Continuum
ε_∞	interband contribution to Drude model
ω_p	bulk plasma frequency
γ	damping parameter
β	frequency dependent damping parameter **or** TPA coefficient
α	absorption coefficient
Ψ, Δ	ellisometric parameters
N	number of free carriers
e	electron charge
m^*	electron effective mass

T_e	electron temperature
T_l	lattice temperature
T_a	ambient temperature
C_e	electron specific heat
C_l	lattice specific heat
$G_{1,2}$	temperature coupling parameters
$P(t)$	power absorption rate

SUMMARY

The object of the present research is to design and fabricate metal-dielectric thin film multilayer structures that make use of the nonlinear optical (NLO) response of Ag for efficient nonlinear absorption for sensor protection. These structures employ structural resonances to overcome the challenges of reflection and absorption that limit access to this large NLO response. The research consists of three parts: first, we present a comprehensive analysis of the contributions to the nonlinear optical response of Ag. Second, we present a systematic investigation of the linear optical properties of Metal-Dielectric Photonic Band-Gap (MDPBG) structures, including optimization of the structure for a particular transmittance spectrum. Third, we study the linear and nonlinear optical properties of Induced Transmission Filters (ITFs). Each of these parts includes experimental results backed by modeling and simulation.

Chapter 1. Introduction and background

1.1 Overview

The object of the present research is to design and fabricate metal-dielectric thin film multilayer structures that make use of the nonlinear optical (NLO) response of Ag for efficient nonlinear absorption for sensor protection. These structures employ structural resonances to overcome the challenges of reflection and absorption that limit access to this large NLO response. The research consists of three parts: first, we present a comprehensive analysis of the contributions to the nonlinear optical response of Ag. Second, we present a systematic investigation of the linear optical properties of Metal-Dielectric Photonic Band-Gap (MDPBG) structures, including optimization of the structure for a particular transmittance spectrum. Third, we study the linear and nonlinear optical properties of Induced Transmission Filters (ITFs). Each of these parts includes experimental results backed by modeling and simulation.

1.2 Sensor protection and nonlinear absorption

The NLO properties of metal, in particular the noble metals (Au, Ag, and Cu), have great promise in the area of optical sensor protection. Every optical sensor, including semiconductor photodiodes, CCD cameras, and even the human eye, has a damage threshold above which the sensor will be damaged. Naturally, it is desirable to have as high a damage threshold as possible. The simplest method of improving the damage threshold is to place a simple absorber in the optical path before the sensor. This is like wearing a pair of sunglasses to limit glare from the sunlight. However, this comes at the cost of reducing the sensor's sensitivity at low intensity and can greatly reduce the effectiveness of the sensor. The ideal solution is to have an attenuator that

is highly transmissive at low intensity but becomes increasingly absorptive at high intensity, as shown in Fig. 1.1. This is like wearing Transitions sunglasses that are transparent in low light but become dark when exposed to sunlight. In this way the sensitivity is preserved at low intensity while protecting the sensor at high intensity. This is essential characteristic of a nonlinear absorber, and it is for this purpose that metals are being investigated.

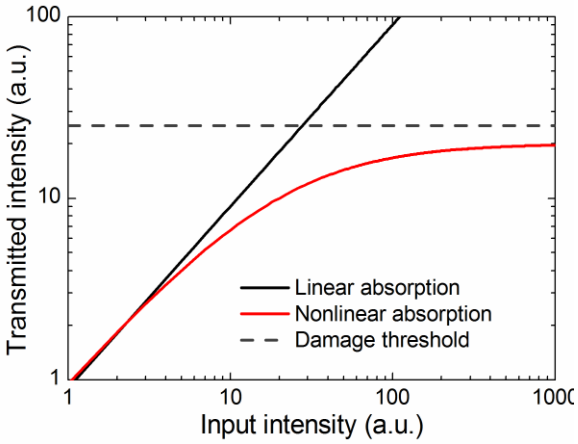

Figure 1.1 Input vs. output intensity of nonlinear absorber

The particular area of interest for this research is in the ultra-fast domain, considering threats such as pulsed lasers that occur on the femtosecond to nanosecond timescale. The challenge is that nonlinear absorption systems with such fast responses typically have very high activation thresholds.

These include systems based on two photon absorption (TPA), which is essentially instantaneous. In a TPA material there exists an electron transition that has an energy gap twice the energy of the incident photons, so that two photons must be absorbed simultaneously in order for the transition to occur. The likelihood of this transition is proportional to the square of the number of incident photons, and so becomes increasingly likely at high intensities. The

absorption coefficient can be expressed as $\alpha + \beta I$, where α is the linear absorption coefficient and β is the nonlinear absorption coefficient. Two photon absorption is common in semiconducting materials such as GaAs and ZnS [1-3] as well as some organic materials [4, 5] with typical β values on the order of 5 GW/cm.

Related to TPA is the phenomenon of excited state absorption (ESA), or reverse saturable absorption [6]. In these materials electrons absorb the incident light and are promoted to a higher energy level. These excited electrons are then able to absorb a second photon of the same energy. If the absorption cross section of the second transition is larger than that of the first, then the material as a whole becomes more absorptive. The efficiency of ESA is also a function of the lifetime of the excited state: the longer the electrons remain in the excited state, the larger the excited state population will be. Example materials include C_{60}, phthalocyanines, and various organic dyes [6-11]. Excited state absorption is a fast process, but not instantaneous because it takes some time to build up the excited state population.

The threshold values of these systems are too high for many practical sensor protection applications. It is desirable to explore alternate systems that can either replace, complement, or enhance TPA and ESA materials. It is in this spirit that we investigate the NLO responses of thin metal films.

1.3 Challenges to accessing the NLO response of metal

Metal has great potential for nonlinear absorption applications because the reported NLO responses are orders of magnitude larger than traditional TPA materials. It should be possible, in theory, to accomplish the same degree of nonlinear absorption with an amount of metal that is far

smaller than the amount of TPA material that would be required. Additionally, metals have the potential to act as broadband nonlinear absorbers because the NLO responses extend over large regions of the spectrum. There are, however, two fundamental challenges that stand in the way of accessing this nonlinearity.

The first challenge is the high reflectance of metal. This high reflectance is caused by the large difference in refractive index between metal and air, for instance, or between metal and SiO_2 or any other dielectric commonly used in optical applications. For example, the reflectance of a bulk slab of Ag is greater than 96% across the visible spectrum. In fact, it is only necessary for an Ag film to be 12 nm thick in order to have 50% reflectance at 600 nm. In order to access the NLO response of any metal it is necessary to create a structure that reduces or eliminates this inherent reflectance.

The second challenge is absorbance. Unlike TPA materials, which can be transparent at their target wavelengths, metals have high absorption across the spectrum. Even if reflectance can be completely eliminated, with skin depths on the order of 10-20 nm in the visible spectrum, film thickness is limited to a few tens of nanometers in order to retain a reasonable degree of transmittance. Figure 1.2 illustrates the reflectance and transmittance of a 100 nm thick Ag film at 600 nm.

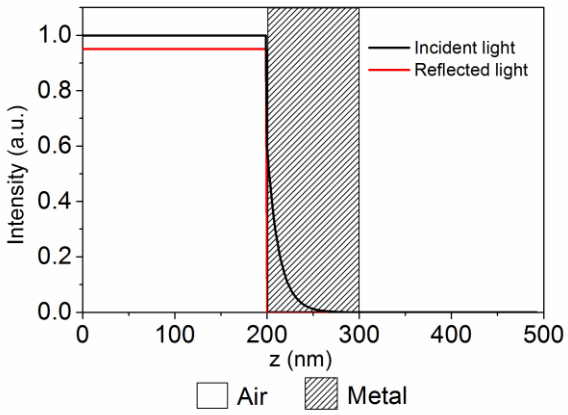

Figure 1.2 and absorption in a thick silver film

Because absorbance is unavoidable, any system that makes use of metal as a NLO material is not scalable. That is, whereas doubling the thickness of a TPA material has the potential of doubling the nonlinear absorption, doubling the thickness of a metal will only increase the linear absorption and may not increase nonlinear absorption at all. Because of this, the challenge becomes maximizing the NLO response of a structure with the least amount of metal possible.

To further complicate matters, the NLO response of metals is an absorption driven thermal process. The incident light that is absorbed by the metal film is converted to heat in a free electron cloud. The heat is then transferred over a timescale of a few ps to the crystal lattice of the metal. The optical properties of the metal are, in turn, a function of the electron temperature and the lattice temperature.

There are several consequences of the fact that the NLO process is absorption driven. The first is that the NLO response is a function of time. If the incident pulse is less than 1 ps in duration, then the initial NLO response (as measured by a low intensity probe) will be due to the initial rapid change in the electron temperature. Over the next few picoseconds the NLO response due

to the electron temperature decreases and the response due to the lattice temperature increases, and once the electrons and lattice reach thermal equilibrium the total NLO response decays slowly as the metal cools down. On the other hand, if the pulse is longer than 10 ps, the electrons and lattice remain nearly in thermal equilibrium throughout the pulse and the subsequent cooling. In order to properly predict this NLO response, it is necessary to understand and take into account this transient behavior.

The second consequence is closely related, in that the total NLO response of metals is a function of the total fluence that is absorbed by the metal rather than the peak intensity of the incident pulse. This is a significant difference between metals and TPA materials because the effective β of the metal is different depending on the duration of the incident pulse. The total fluence of a 1 GW/cm^2, 100 fs pulse is much less than the total fluence of a 1 GW/cm^2, 1 ns pulse, so the observed nonlinearity in the latter is expected to be much greater than in the former.

The third consequence is that it is neither possible nor desirable to eliminate all absorption from the metal. If absorption were completely eliminated, there would be no NLO response at all. Thus, the structure can never have 100% transmittance even at low intensity. The structure must instead be designed to have a certain amount of absorbance, and to make the most efficient use of that absorbance.

The fourth consequence is that any light that is neither transmitted nor absorbed does not contribute to the NLO response. Thus, any reflected light is wasted. This is especially a problem because, as mentioned, the reflection coefficients of metals are quite high, and adds impetus to the challenge of eliminating reflections as much as possible.

These four consequences must form the basis of any discussion of structures using the NLO response of metals.

All of the design work alluded to assumes a thorough understanding of the NLO response of the metal around which the design is built: its magnitude, the relative strengths of the electron and lattice dependent components, the temporal dynamics, and the dependences of all of these attributes on the physical attributes of the metal itself, such as grain size and morphology. Thus, underlying the engineering goals of designing optimal NLO metal structures is the need for fundamental physical work describing the NLO process itself. The next section looks at the nature of the NLO response of metal in the context of prior studies on the subject, highlighting what is known and what remains to be studied. The section following describes the state of the art regarding various structures that have been employed for linear and NLO applications making use of metals in some way.

1.4 The nature of the NLO response of metals

The optical responses of noble metals in the visible part of the spectrum have two components: interband transitions and the free electron contribution.

Individual absorption peaks can be calculated from the band models of the various metals (see, e.g., [12, 13]). For Au and Cu the onset of interband transitions is in the visible region of the spectrum and extends to higher frequencies, while for Ag the onset is in the UV. The thermal dependences of these absorption peaks have been the subject of a number of thermomodulation experiments [14-18] that reveal how the band structure changes with temperature. This

temperature dependence dominates the NLO response of Au and Cu in the visible spectrum, but is only peripheral in the case of Ag.

A review of the free electron contribution to the optical properties of metals begins with the Drude model of free electrons [19], which describes the kinetics of interactions between the free electron cloud and the crystal lattice of the metal (electron-phonon interactions). This model also describes the response of the electron cloud to an oscillating electric field, and so can be used to model the response of metal to light. The complex dielectric permittivity can be expressed as:

$$\varepsilon = \varepsilon_\infty - \frac{\omega_p^2}{\omega^2 + i\gamma\omega}, \tag{1.1}$$

where ε_∞ is the sum of the interband contributions, ω_p is the bulk plasma frequency, and γ is a damping parameter.

The free electron contribution is present at all frequencies starting at DC up through the bulk plasmon frequency. At frequencies below the onset of interband transitions the only remainder of the interband transitions is a tail in the real part of the complex permittivity; the optical response is otherwise determined completely by the free electron contribution, as demonstrated in [20]. The Drude model can be expanded to take into account a frequency dependence in the damping constant γ that has been observed experimentally in a variety of metals by introducing a frequency dependent parameter β [21-24]:

$$\gamma = \gamma_1 + \beta\omega^2 . \quad (1.2)$$

This frequency dependent term is significant in the near infrared and visible portions of the spectrum for the noble metals, which is the region of particular interest in the present work, and as such it is necessary to include this term to have an accurate model for analysis.

The damping parameter in the Drude model is also strongly morphology dependent [22, 25-27]. Surface scattering is a significant contribution to this damping, so film thickness plays a role in this parameter: the thinner a film is, the more significant surface damping becomes. Surface roughness increases this damping further. Thus, it cannot be safely assumed that the Drude parameters are constant for any given metal from one film to the next, or from film to nanoparticle. Thus, it is essential to measure the permittivity of the metal for every sample.

The Drude model parameters exhibit some temperature dependence as well. Temperature dependence in the damping parameter γ has been experimentally demonstrated via thermomodulation experiments [22, 23, 26, 28], and temperature dependence in other parameters has been suggested [23], though there is not sufficient precision in these measurements to determine precisely what this dependence is. It is this temperature dependence that leads to the NLO properties observed in Ag in the visible region of the spectrum, and so constitutes the primary focus of the present research.

All of the studies mentioned to this point were performed at the steady state; that is, the sample was held at each target temperature long enough for the entire system to reach thermal equilibrium. Thus, they do not demonstrate how these metals can be used in ultrafast systems.

The first experiments to measure the response of metal at fast time scales focused on nanoparticles [29-32], and since then many other experiments have measured different variations of nanoparticle systems [33-44]. However, the results of these measurements are often reported in terms of effective β values, as if the response were instantaneous. This does not reflect the true nature of the underlying response because it does not capture transient effects that arise due to differences in electron and lattice temperatures. These transient effects can only be captured properly with time-resolved pump-probe experiments that show how the nonlinear response evolves over time. Several properties of the NLO response of a metal can be learned from pump-probe experiments, depending on the system being tested and the capabilities of the pump-probe setup.

The first transient property that was experimentally determined is the rate of energy transfer from the electron cloud to the lattice [45-51]. It was determined that there is an initial, strong NLO response that decays with a characteristic time scale of 0.5 ps to 4 ps. This decay rate agrees with calculations of electron-phonon interaction rates based on quantum mechanical principles [52], indicating that the initial response is a function of the electron temperature that decays as the energy is transferred to the lattice. This effect was observed both in thin films [46-48] and in nanoparticles [49-51], with generally good agreement on decay rates between the two.

If the pump and probe pulses are short enough, it is possible to resolve the effects of an initial athermal electron population [53-58]. When the electron cloud is heated by the pump pulse, it is not heated equally; there is a small population of electrons that have been heated to a high temperature, while the rest are still cool. Over the first hundred femtoseconds or so the hot

electrons transfer their energy to the full electron population; this is the process of electron thermalization.

Based on these studies, the temporal dynamics of the reaction of a metal to a pulse can be described as follows. Over the duration of the pulse, a small population of electrons is heated to a high temperature. Within the first picosecond this small hot electron population transfers its energy to the full electron cloud, creating a thermal distribution (i.e. one that can be described by a Fermi distribution in energy). Within the first ten picoseconds, the electron cloud transfers the energy to the lattice until thermal equilibrium has been reached. The heat is then dissipated into the surrounding environment over hundreds of picoseconds to nanoseconds.

Slightly more complicated to determine than the temporal NLO metal response is the spectral NLO response. This requires that the probe pulse contain a broad spectrum, or white light continuum (WLC). Experiments can then be performed that span both frequency and time, and it begins to be possible to get a full picture of the dynamics of the NLO response of a metal.

At this point a differentiation must be made between measurements made on thin films and those made on nanoparticle systems. In nanoparticles, the NLO response is amplified by surface plasmons [51, 56-59]. While this is beneficial for increasing the total NLO response, it masks the exact magnitude of the intrinsic NLO response of the metal. For this reason, measurements using thin films are more useful for quantitative analysis of the spectral NLO response.

Quantitative measurements of the spectral NLO response of a metal can more accurately be performed on thin-film systems [47, 54, 57, 60-63]. These systems are simpler than those using

nanoparticles, so the inherent NLO response can be more readily extracted. However, the challenges of reflectance and absorbance described in the previous section come into play so the thickness of the films that can be measured is limited. This limitation may be part of the reason that there significantly fewer pump-probe WLC measurements on thin metal films than on nanoparticles. These studies focus primarily (though not exclusively; see, e.g. [60]) on changes in the interband transitions rather than the free electron contribution. Thus, there is much to be learned yet regarding the free electron contribution to the transient NLO responses of these metals.

This gap provides the motivation for the first objective of the present research. In an effort to begin to close this gap, we developed a comprehensive model that describes the free electron contribution to the NLO response of a thin Ag film. Ag was chosen for this study because it is the simplest of the noble metals to analyze in the visible spectrum because no interband transitions are present within the visible spectrum to mask the free electron NLO contribution. This study gives quantitative analysis of the measured NLO transmission and reflection from a 20 nm thick Ag film, from which the change in the complex permittivity $\Delta\varepsilon$ is extracted. This change in permittivity is related back directly to changes in the Drude model parameters, thereby giving a simple model of the free electron contribution to the NLO response while at the same time giving greater insight into the underlying physical mechanisms that give rise to this nonlinearity. This study has an impact on the NLO responses of Au and Cu, as the same physical mechanisms are present in these metals as well.

This study lays a foundation for the design of multilayer structures that make use of the NLO properties of metals. A history of these multilayer structures, including both linear and nonlinear applications, is the subject of the next section.

1.5 Metal-dielectric multilayer structures

The first metal-dielectric multilayer (MDM) structure that sought to improve the transmissive characteristics of a metal film was the induced transmission filter (ITF), proposed by Berning in 1957 [64] and described extensively in [65]. The ITF consists of a single metal film sandwiched between two dielectric structures that act as antireflection coatings at a particular wavelength. The result is a narrow pass band filter that achieves much higher transmittance at the center wavelength than would be possible in an isolated metal film. An example of this is shown in Fig. 1.3.

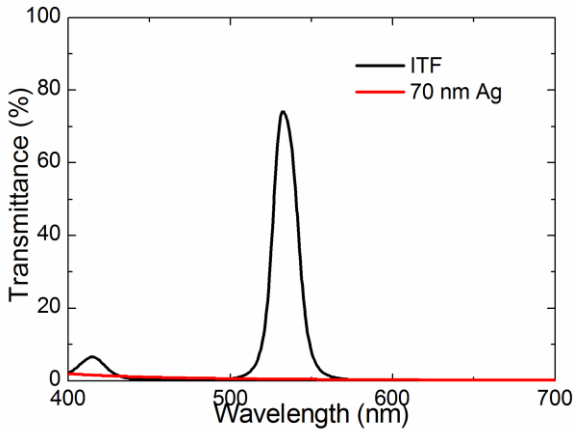

Figure 1.3 Transmittance of a 70 nm thick Ag film compared to an ITF containing 70 nm Ag

Since that time there has been great interest in the use of MDMs for architectural coatings, that is, coatings on windows that manage the relative intensities of visible and infrared light

penetrating into a building [66-68]. MDMs are of great interest in this field because metal is very efficient at reflecting light at infrared wavelengths and beyond; at the same time, it is possible to make fairly efficient band pass filters that are only a few layers thick.

In more recent years MDMs have been reincarnations of one dimensional metal-dielectric photonic crystals (MDPCs) or metal-dielectric photonic band-gap structures (MDPBGs) [69-94], arising in part from the interest in multidimensional MDPCs that arises from the large band gaps that are possible in such structures as well as interest in one-dimensional all dielectric photonic crystals [95]. One dimensional MDPBGs are multilayer structures that typically consist of periodic arrangements of alternating layers of one metal and one dielectric material, with typically no more than five periods. MDPBGs have wider pass bands than ITFs; an example transmittance spectrum is shown in Fig. 1.4. These structures are interesting for several reasons. First, similar to the architectural coatings, they are interesting in their ability to be transparent at visible wavelengths while having strong rejection at wavelengths such as RF [69, 70, 78, 85]. Second, they are candidates for transparent electrodes, making use of the high conductivity of the metal while mitigating the need for transparent conducting oxides such as ITO [73, 75, 81]. Third, and most relevant to the present work, MDPBGs provide direct access to the NLO response of metal by reducing or eliminating reflections over a relatively broad wavelength range [68, 92, 96-100]. Thus, it is conceivable that an MDPBG could be used as a broadband nonlinear absorber.

Various adaptations of a strictly periodic structure geometry have been explored to tailor the linear transmittance for particular characteristics [71, 77, 85]. These focus primarily on structures that make use of high index dielectrics because they generally make it possible to

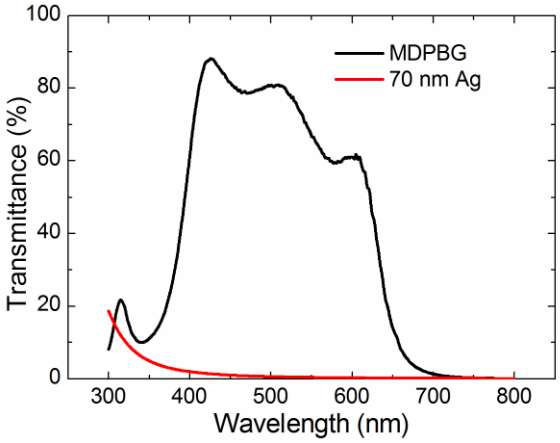

Figure 1.4 Transmittance of a 70 nm thick Ag film compared to an MDPBG containing 70 nm Ag

achieve higher transmittance than with low index dielectrics. However, under some scenarios it may be desirable to use a low index dielectric; for instance to avoid some of the fabrication issues associated with many high index dielectrics [85, 86]. Also, if an organic material is used, it will typically have a low refractive index. Thus, it is worthwhile to explore the design space based on low index dielectrics to determine the potential capabilities and fundamental limitations of such a structure. It is also desirable to be able to have a systematic method to design a structure for an arbitrary transmittance.

To this end we performed, through simulation, a systematic variation of structural parameters in order to qualify and quantify the effects on the resulting transmission and reflection spectra. This aids in the understanding of how an MDPBG could be tailored to a particular desired linear transmittance spectrum and establishes certain fundamental limitations of the structure. Also, we created a routine that demonstrates the ability to optimize the transmittance of an MDPBG for a particular transmittance spectrum. This optimization process uses an algorithm in which the individual thickness layers are allowed to vary independently, resulting in an aperiodic structure. This optimization represents a departure from the standard periodic MDPBG designs and makes

it possible to create much flatter pass band characteristics than a purely periodic structure would be capable of. We validated this process by fabricating and characterizing the resulting structure.

The linear optical properties of MDMs are only the beginning of the story. A small volume of work exists on the NLO properties of these structures, as well. It was not long after MDPBGs were proposed that their potential as nonlinear structures was pointed out [96], suggesting that the potential nonlinear phase shift of a Cu film could be enhanced by a factor of 40. Since that time there have been theoretical and experimental investigations of the amplification of second harmonic generation (SHG) by metal [98], amplification of the NLO response of the dielectric [101], and amplification of the NLO response of the metal itself [68, 92, 97, 99, 100, 102], all using MDPBGs. In general, these structures have demonstrated a significant enhancement of the NLO response of an MDPBG over an isolated metal film, though no systematic studies have been done to determine how to achieve the optimal NLO response. Such a study is beyond the scope of the present work, though it would be a natural extension to combine the optimization of the linear optical properties with the comprehensive studies of the NLO response of a single film.

The only report of a study on the NLO response of a structure resembling an ITF is a theoretical study investigating the potential for bistability in such a structure [103]. This is a significant gap in the body of knowledge of nonlinear MDMs because the ITF has a couple distinct advantages over the MDPBG. First, the ITF is a simpler structure in that it contains only a single layer of metal. This can simplify the fabrication, as some difficulties with combining metals and dielectrics can be avoided. It is also simpler conceptually; there are fewer "moving parts," as it were, because only the NLO response of a single film needs to be considered, so understanding and predicting the NLO response of the full structure is more straightforward. In addition, the

electric field enhancement in the single metal layer of the ITF is greater than the enhancement within each of the layers of an MDPBG. For this reason, the NLO response of the ITF has the potential to be greater than that of the MDPBG – though over a much smaller wavelength range.

In order to address this gap we simulated and experimentally demonstrated the NLO response of an ITF. We first performed a systematic modeling of the NLO response of an ITF. By looking at several different variations of the structure we were able to derive a simple set of rules describing the nature and magnitude of the response. To validate these rules we fabricated two different ITF structures and measured their response using WLC pump-probe measurements.

1.6 Summary

The three research objectives covered in this work are:

1) Develop, through WLC pump-probe measurements and through simulation, a comprehensive model that describes the NLO response of a thin Ag film
2) Perform a systematic study of the linear optical properties of low index MDPBGs, including the development of an algorithm to optimize a structure for an arbitrary transmission spectrum
3) Simulate and experimentally demonstrate the NLO response of an ITF, including a study of sensitivity to design parameters.

This work will be covered in s 2 through 4, respectively.

Chapter 2. Linear and nonlinear optical characterization of thin Ag films

2.1 Introduction

The nonlinear optical properties of noble metals have received great attention because the nonlinearity is orders of magnitude larger than in any other known material, as described in 1 [29, 35, 104]. Silver, in particular, is interesting because the interband absorption peaks lie energetically above the visible spectrum, opening up the possibility of broadband applications in the visible portion of the spectrum [69, 70, 78, 97, 101]. The electronic and thermal properties that contribute to the nonlinearity, however, are not straightforward, and no fewer than five different processes contribute. These include both interband and intraband (free electron) contributions, and contributions that depend on either the electron or the lattice temperature, which are all different from the relatively weak pure $\chi^{(3)}$ processes (on the order of 2×10^{-11} esu measured by third-harmonic generation (THG) at 1064 nm [105]). Understanding the source and nature of these contributions is essential to maximizing the effects of these nonlinear processes in more complex structures such as metal-dielectric photonic crystals [96, 101, 102] or induced transmission filters [64, 103].

With the present experiments we generate a simple model that can be used to predict this response when incorporated into more complex multilayer structures. Such a model could be used to predict the response when thin Ag layers such as the ones discussed in this work are incorporated into more complex multilayer structures. We also discuss the current understanding of the origin of the observed nonlinear optical responses of Ag.

The physical mechanisms that contribute to the nonlinear properties of Ag have, in general, different temporal and/or spectral contributions to either the real or imaginary part of the dielectric permittivity ε, so in theory it should be possible to distinguish among these contributions from a single set of measurements provided they cover sufficiently large spectral and temporal ranges. To this end, we have performed femtosecond white light continuum (WLC) pump-probe spectroscopy in both transmission and reflection modes on thin (20 nm) films of Ag. From these measurements, with full knowledge of the structure, we determined ε across the spectral range of the white light continuum probe for times both during and after the interaction of the pump with the sample. Then, we fitted ε using a two temperature model in the time domain and a modified Drude model in the frequency domain. The Drude model was modified to take into account a limited amount of dispersion in the interband contribution. In doing so we were able to quantify the magnitudes and time scales of each contribution.

The remainder of this is organized as follows. In section 2.2, we describe the fabrication of thin Ag films and discuss some of the physical processes associated with deposition that place constraints on the fabrication process. We then describe in section 2.3 the modeling and simulation tools that were used to characterize the experimental results. In section 2.4, we present the models used to describe the optical properties of the materials. In section 2.5, we detail the linear and nonlinear characterization techniques that were used. In section 2.6, we present the results of the optical characterization. Then in section 2,7 we discuss the underlying physical mechanisms that contribute to this nonlinear optical response.

2.2 Fabrication

2.2.1 Fabrication procedure

All samples were fabricated on 0.16 mm-thick glass cover slips (Ted Pella #260140) that had been cleaned ultrasonically in soap, deionized water, acetone, and isopropanol for 15 minutes each. The films were deposited with a Kurt J. Lesker Axxis electron beam deposition system with a starting pressure of no more than 1.3×10^{-4} Pa (1×10^{-6} Torr). The Ag and SiO_2 layers were deposited at a rate of 0.2 nm/s and the Ti layers at a rate less of than 0.02 nm/s, controlled manually in order to achieve sub-nm thickness. The samples were actively cooled and held at room temperature throughout the deposition, and were rotated during deposition to improve film uniformity. A minimum of 50 nm SiO_2 was first deposited on all samples to provide a consistent starting surface and to mitigate some of the surface roughness of the substrate (though the surface roughness was not specifically measured).

2.2.2 Ag film growth

It is well known that it is not possible to fabricate arbitrarily thin Ag films on most dielectrics because there is a large mismatch in the surface energies of the two materials [106]: the Ag adheres to itself far more readily than it does to the dielectric. Instead, Ag follows a Volmer-Weber growth pattern, in which the Ag first forms nanometer-sized nanoparticles. As more Ag is added, the nanoparticles become interconnected networks that gradually become denser, eventually becoming films with pinholes. Ultimately these pinholes are filled in and fully continuous films are formed. However, this final step does not occur until the film is on the order of 10 to 20 nm thick, depending on the underlying dielectric. This progression can be seen

in Fig. 2.1, which shows SEM images of Ag layers deposited on Al_2O_3 that have nominal thicknesses of 1 nm, 12 nm, and 25 nm.

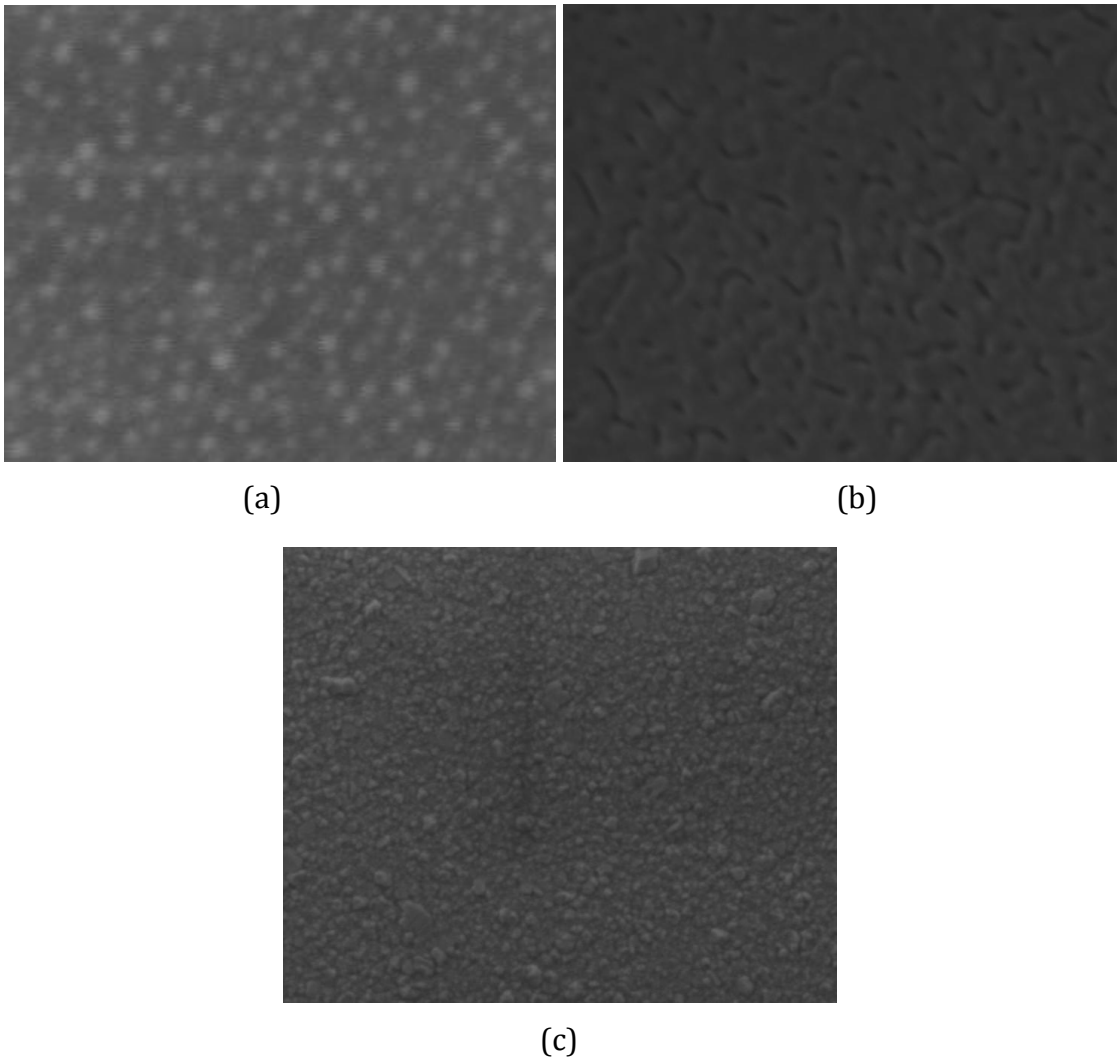

Figure 2.1 SEM images of Ag depositions with nominal thicknesses (a) 1 nm, (b) 12 nm, (c) 25 nm on Al2O3, showing the progression from nanoparticles through interconnected networks to continuous films

The fact that there is a certain minimum Ag film thickness has significant implications in the design of multilayer structures. In some of these structures it is desirable to have Ag films that are as thin as possible, so this growth process is a significant design constraint that must be

considered. It is also noteworthy that this growth process leads to rough films, even when the film is continuous, because individual grains may protrude above the film surface. The film thickness, surface morphology, and grain size could be measured using Transmission Electron Microscopy (TEM) provided that the films are not damaged by the sample preparation process.

2.2.3 Ti adhesion

The mismatch in surface energy and poor adhesion between Ag and the dielectric leaves the Ag film susceptible to damage, as any stress will cause the Ag to detach from the dielectric. In order to mitigate this problem a Ti adhesion layer was introduced before and after each Ag film. The Ti adhesion layer had a nominal thickness of 0.25 nm; the reason why such an adhesion layer is effective is unclear, but it is thought that the Ti oxidizes and forms small islands of TiO_2; these islands act as seed crystals for the growth of Ag [107]. Regardless, the adhesion layer was found in the present measurements to significantly increase the damage threshold of the Ag films.

2.3 Modeling and simulation

2.3.1 Transfer matrix method

The transfer matrix method was used extensively in this research to model the transmittance and reflectance of thin film structures. It is a very useful tool because it can give exact analytical solutions to calculations of transmittance and reflectance; it is at the same time a very fast and simple method. It is based on calculations of the Fresnel reflection and transmission coefficients at each interface within a thin film structure. The equations presented here are for light at normal incidence because this is the simplest case and the only one used in the present work. It can be readily extended to arbitrary angles of incidence.

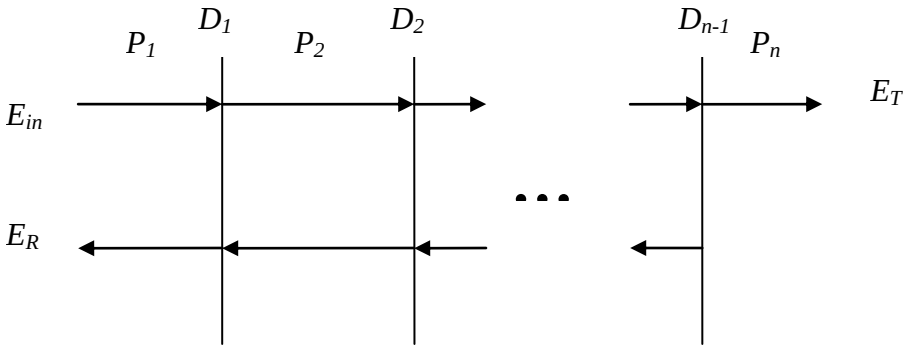

Figure 2.2 Setup for transfer matrix method

The transfer matrix method breaks down the calculation of the transmittance of light into a series of matrices:

$$\begin{bmatrix} E_{in} \\ E_r \end{bmatrix} = P_1 D_1 P_2 D_2 \cdots D_{n-1} P_n \begin{bmatrix} E_t \\ 0 \end{bmatrix}, \tag{2.1}$$

where E_{in} is the incident electric field, E_r and E_t are the reflected and transmitted electric fields, respectively, and P_i and D_i are the transfer matrices. Each D_i represents the reflection and transmission through each interface in the structure, as shown in Fig. 2.2, and each P_i represents transmission within each layer. These matrices take the forms

$$P_i = \begin{bmatrix} e^{i2\pi n_i t_i/\lambda} & 0 \\ 0 & e^{-i2\pi n_i t_i/\lambda} \end{bmatrix} \tag{2.2a}$$

$$D_i = \begin{bmatrix} 1/t_i & r_i/t_i \\ r_i/t_i & 1/t_i \end{bmatrix}, \tag{2.2b}$$

where n_i and t_i are the complex refractive index and thickness of the ith layer, respectively, λ is the free space wavelength, and r_i and t_i are the Fresnel reflection and transmission coefficients of the ith interface, respectively. These coefficients can be expressed in terms of the refractive indices of the two materials as:

$$r_i = \frac{n_i - n_{i+1}}{n_i + n_{i+1}}, \tag{2.3a}$$

$$t_i = \frac{2n_i}{n_i + n_{i+1}}. \tag{2.3b}$$

With full knowledge of the refractive index and thickness of each layer, each of the transfer matrices is fully determined. Eq. (2.1) can be simplified to

$$\begin{bmatrix} E_{in} \\ E_r \end{bmatrix} = M \begin{bmatrix} E_t \\ 0 \end{bmatrix} \tag{2.4}$$

where

$$M = D_1 P_1 D_2 P_2 \cdots D_{n-1} P_{n-1} D_n. \tag{2.5}$$

Then E_t and E_r can be solved for directly. No approximations are made, so these solutions are exact.

The transfer matrix method was extended to take into account reflections from the back side of the substrate. The thickness of the substrate is too large to be treated simply as another layer in the transfer matrix method. Instead, the reflection from the substrate is calculated directly using the Fresnel reflection coefficient and the phase shift within the substrate.

A portion of the light that enters the substrate will be reflected between the structure and the back side of the substrate multiple times. With each reflection the portion grows significantly smaller, so in the present work we consider only up to the second back-reflection; that is, light that enters the substrate, reflects off the structure, reflects off the substrate, reflects off the structure again, and exits. The residual error is well under 1%.

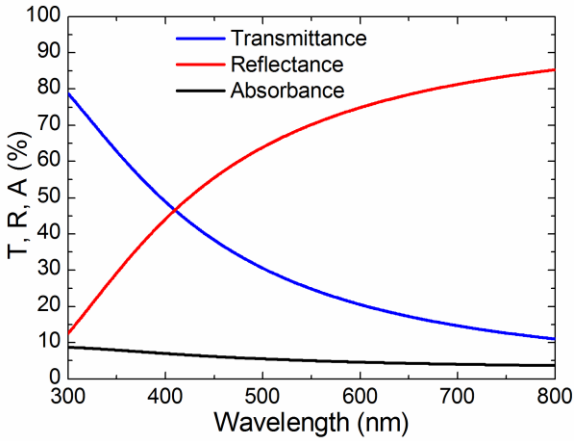

Figure 2.3 Transmittance, reflectance, and absorbance of a 20 nm thick Ag film calculated by the transfer matrix method

Figure 2.3 shows the transmittance, reflectance, and absorbance of a 20 nm thick Ag film as calculated by the transfer matrix method.

2.3.2 Nonlinear transfer matrix method

The transfer matrix method was modified to take into account changes in refractive index over time. This was done by recalculating the transmittance and reflectance over a series of time steps. At each time step the refractive indices of the nonlinear films were recalculated and used to define the transfer matrices for the following time step. The incident pulse was treated as a Gaussian pulse in time. While this method loses the exactness of the transfer matrix method in treating linear problems, if the time step is small enough, the accuracy is sufficient. We describe in detail how this works out if the only nonlinear material present is a single film of metal and all other materials are perfectly transparent, since this is the only scenario for which such calculations are carried out in the present work.

Consider the case where the incident pulse has width w= 50 fs (HW 1/e). Time t_o, the time at which the peak of the pulse interacts with the structure, is chosen to occur at 200 fs. This gives enough lead time so that the leading edge of the pulse is not chopped off. The pulse can then be represented as:

$$I = \frac{I_0}{w\sqrt{\pi}} e^{\left((t-t_0)^2/w^2\right)} \tag{2.6}$$

In the case of metal, as will be explained in detail later, the refractive index is a function of the temperature of the film. The temperature is, in turn, a function of the energy absorbed by the metal film. Specifically, all of the energy absorbed by the film is converted to heat. The equations for calculating the temperature and the refractive index will be given later; at present

the concern is calculating the absorbed energy density E_a [J/m^3] at each time step. This is easily done; since all light that is neither transmitted nor reflected is absorbed, it can be expressed as

$$E_a(t) = \frac{I(t)dt}{t_m} \times (1 - T(t - dt) - R(t - dt)), \tag{2.7}$$

where T and R are the transmittance and reflectance of the structure, as calculated by the transfer matrix method at the previous time step; dt is the time step; and t_m is the thickness of the metal film. From this, the film temperature and refractive index can be recalculated, and the transfer matrix method can be applied to calculate the transmittance and reflectance at the next time step.

2.4 Material modeling

2.4.1 Drude model

The complex permittivity of Ag in the visible region of the spectrum can be described using the Drude model:

$$\varepsilon = \varepsilon_\infty - \frac{\omega_p^2}{\omega^2 + i\gamma\omega}, \tag{2.8}$$

where ε_∞ is the sum of the interband contributions, ω_p is the bulk plasma frequency, and γ is a damping parameter. Equation (2.8) can be decomposed into its real and imaginary components, assuming $\gamma << \omega$:

$$\varepsilon_r = \varepsilon_\infty - \frac{\omega_p^2}{\omega^2}, \quad \varepsilon_i = \frac{\gamma\omega_p^2}{\omega^3}, \tag{2.9}$$

where γ can be separated into a frequency-independent term γ_l and a frequency-dependent term β:

$$\gamma = \gamma_l + \beta\omega^2 . \tag{2.10}$$

Strictly speaking, ε_∞ is a function of frequency. Its dispersion could be calculated using the Kramers-Krönig relation from the interband absorption spectrum, though such calculations are beyond the scope of this research and ε_∞ is approximated as a constant. This dispersion makes it difficult to fully separate the contributions of ε_∞ and ω_p, to ε_r, as will be seen later. However, for the purpose of the linear optical properties, ε_∞ was treated as a constant.

The nonlinear optical response of Ag can be accounted for in the Drude model by introducing a temperature dependence in the parameters ε_∞, ω_p, and γ. The temperature dependence of ε_∞ must include a dispersion term in order to account for some of the behaviors observed in the NLO response, but otherwise this NLO response can be fully described by these temperature dependent parameters.

The complex refractive index is simply the square root of the complex permittivity.

2.4.2 Linear optical materials

The dielectric and the substrate can each be assumed to have negligible NLO response. For these materials it is sufficient to have a tabulation of the refractive index across the spectral region of interest. For those wavelengths of interest that fall between the tabulated values, the refractive index was interpolated using a cubic spline method.

2.5 Characterization techniques

2.5.1 Spectroscopic ellipsometry

The refractive indices of bulk materials were measured by spectroscopic ellipsometry using a Woollam M2000 spectroscopic ellipsometer. Ellipsometry does not directly measure the refractive index of a material; rather, it measures the change of polarization of light as it is reflected off the surface of a film or stack of films. This data is extremely versatile and can be used to extract different information about a structure. For instance, if the refractive index of a thin film is known, ellipsometry can be used to calculate the thickness of the film. The same is true for multilayer structures: if the refractive index of each material is known, then the thicknesses of each layer can be determined. Accuracy will be lost as the number of layers increases, but for structures with only a few layers it can be a very reliable tool. Alternatively, if the thickness of a layer is known, the full complex refractive index can be determined. If the material is fully transparent; that is, the refractive index is purely real, then the thickness and refractive index can be determined simultaneously. However, if the material has some absorption then the thickness and complex refractive index cannot be determined. The solution matching the change in polarization to the thickness and refractive index will not be unique. In

this case, supplemental data such as transmittance would be needed to arrive at the unique solution.

The change in polarization can be represented as:

$$\rho = \tan(\Psi)e^{i\Delta}, \tag{2.11}$$

where Ψ and Δ are the measured ellipsometric parameters and $\rho = r_p / r_s$ is the ratio of the Fresnel reflection coefficients of the *p* and *s* polarizations of the incident light. For the reflection off the surface of an infinitely thick film these reflection coefficients are the same as that used in the transfer matrix method, generalized for the case of arbitrary angle of incidence:

$$r_p = \frac{n_t \cos(\theta_i) - n_i \cos(\theta_t)}{n_t \cos(\theta_i) + n_i \cos(\theta_t)} \tag{2.12a}$$

$$r_s = \frac{n_i \cos(\theta_i) - n_t \cos(\theta_t)}{n_i \cos(\theta_i) + n_t \cos(\theta_t)} \tag{2.12b}$$

where n_i and n_t are the refractive indices of the surrounding medium and the film, respectively; θ_i is the angle of incidence, and θ_t is the angle of propagation through the infinitely thick film. This angle is determined by Snell's law:

$$n_i \sin(\theta_i) = n_t \sin(\theta_t). \tag{2.13}$$

Typically n_i = 1 because the surrounding medium is air. Using these equations, the refractive index of the film can be extracted from the ellipsometric measurements. This is usually done by an iterative approximation method, wherein an initial approximation of the refractive index is given, and the expected ellipsometric parameters are calculated; this approximation is then refined until the resulting ellipsometric parameters match the measurements.

For more complex structures the reflection coefficients of the entire structure must be calculated. These structural reflection coefficients can be calculated using the transfer matrix method generalized for arbitrary angles of incidence, and the iterative approximation method can then be applied to any unknowns within the structure.

2.5.2 Transmittance and reflectance

Transmittance measurements were performed using a Cary 5E UV/Vis/NIR spectrophotometer. The measurements made use of baseline correction, where the baseline used was open air (as opposed to using a bare substrate, as is often done). The use of an open air baseline corresponds with the transmittance calculations that arise from the transfer matrix method with substrate correction described above.

Reflection measurements were made using a Xenon light source and a monochromator; detection was accomplished by a pair of Si photodiodes for signal and reference that were connected to lock-in amplifiers. The standard sample used for the baseline for reflection measurements was the160 nm-thick Ag film covered by 50 nm of SiO_2, and the measurements were corrected to account for the fact that the reflectance of the standard is not exactly 100% but closer to 98%. The correction factor was calculated using the matrix transfer method applied to this structure,

assuming a bulk refractive index for Ag. This resulted in the reflection data being adjusted upward by 1-2% across the visible spectrum. All reflectances were measured at 4° from normal incidence; the difference in reflectance compared to normal is negligible at this angle. Only specular reflectance was measured.

2.5.3 White light continuum pump-probe spectroscopy

Nonlinear optical properties were probed using a commercially available pump-probe spectroscopy system (Helios, Ultrafast Systems). A portion (~5%) of a laser beam from a Ti:Sapphire regenerative amplifier (Spitfire, Spectra-Physics) operating at 800 nm and 1 kHz repetition rate provided the probe pulse to generate a white-light continuum (WLC, 500 – 700 nm) while the remainder of the beam generated the pump pulse, tuned to either 550 nm or 650 nm by an optical parametric amplifier (TOPAS-White, Spectra-Physics). The pump beam was chopped at 500 Hz with a 50% duty cycle, with reference spectra being measured while the pump beam was blocked. The signal and reference data were averaged over a thousand measurements at each probe time delay, and a ΔOD spectrum was generated. The result was a wavelength-versus-time 2-D array of ΔOD values. The transmission mode measurements were converted to ΔT values based on the measured linear transmittance T_l according to

$$\Delta T = T_l\left(10^{-\Delta OD} - 1\right). \tag{2.14}$$

The process was repeated for reflection mode. The size of the pump beam at focus was measured using a knife-edge scan and yielded values of 260 μm (1/e radius) at 650 nm, 234 μm (1/e radius) at 550 nm, and the probe beam was 60 μm (1/e radius). Because the probe is

significantly smaller than the pump, it is assumed that the probe overlaps with a region of constant (peak) fluence from the pump. A chirp correction factor was calculated by measuring the cross phase modulation response in the substrate, and the scattered pump light was subtracted based on measurements where the probe preceded the pump so that there was no observable nonlinear response of Ag. The pump pulse duration was 60 fs and the total instrument response time was 150 fs, precluding the possibility of investigating the initial athermal electronic behavior. For this reason, this work focused on time delays larger than 1 ps, at which point the electrons are expected to have reached a thermal distribution.

2.5.4 Structures for characterization

The characterization of the linear and nonlinear optical properties of Ag films was carried out using two different structures. The first was a 160 nm thick Ag film that was used to characterize the bulk refractive index of Ag. This film was thick enough to be completely opaque across the entire spectral region of interest. The second was a 20 nm thick Ag film sandwiched between two 50 nm thick films of SiO_2, with Ti adhesion layers on each side of the Ag film. Both the linear and nonlinear optical properties of this film were measured, and form the focus of this study.

2.6 Optical characterization

2.6.1 Bulk Ag

The refractive index of the 160 nm thick Ag film was measured by spectroscopic ellipsometry. Because this film is thick enough to be opaque, the light does not penetrate through to the back side of the film so only reflections off the top surface contribute to the ellipsometric

measurements. This means that this film can be treated as an infinitely thick film, and the analysis described in section 2.5.1 applies. The bulk refractive index can be extracted from this film, without regard to the film thickness. The measured ellipsometric parameters Ψ and Δ are plotted in Figs. 2.4 a, b for incident angles of 60°, 70°, and 80°, the complex refractive index is shown in Fig. 2.4 c, and the complex permittivity is plotted in Fig. 2.4 d.

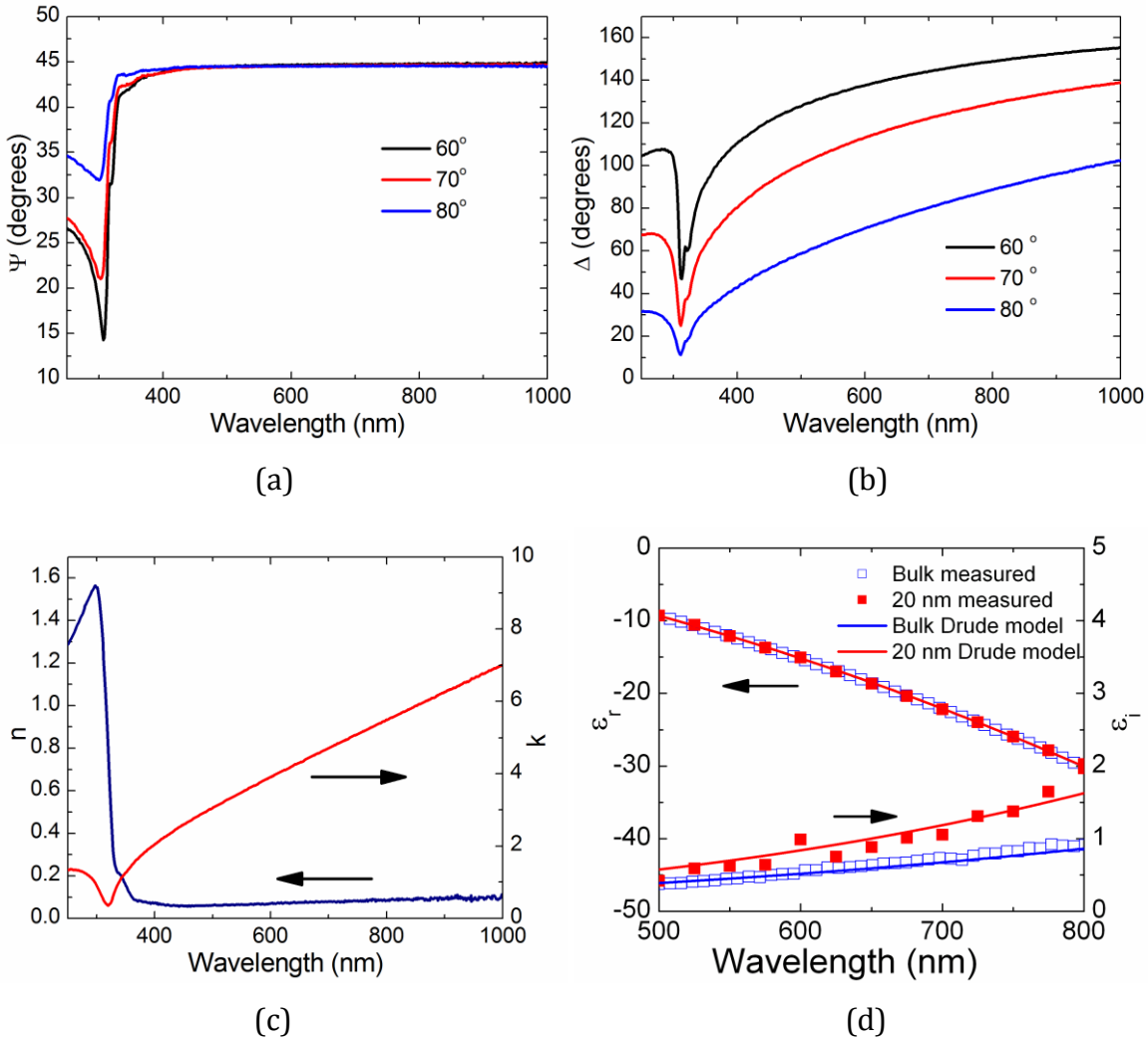

Figure 2.4 (a),(b) Ellipsometry data for bulk Ag film. (c) real (n) and imaginary (k) parts of complex refractive index of bulk Ag film. (d) real and imaginary parts of complex permittivity of bulk Ag film and 20 nm thick Ag film, with Drude model fits to each

The permittivity was fitted to the Drude model with $\varepsilon_\infty = 4$, $\omega_p = 1.38\times10^{16}$ s^{-1}, $\gamma_1 = 2.73\times10^{13}$ s^{-1}, and $\beta = 5.9\times10^{-18}$ s^{-1}. These numbers compare favorably with values from the literature $\omega_p = 1.36\times10^{16}$ s^{-1}, $\gamma_1 = 2.73\times10^{13}$ s^{-1}, and $\beta = 5.8\times10^{-18}$ s^{-1} [20, 23]; ε_∞ differs significantly from the values of 2.7-3.4 reported in [22, 23], though it agrees well with the value of 4 reported in [27]. The variations in this value can be attributed in part to varying densities of the Ag films and to experimental errors either in the present measurements or the cited values; it should be noted that none of these measurements take into account dispersion in ε_∞. If dispersion were included, the value of ω_p would have to be revised downward.

It was shown in [27] that in bulk Ag if the grain size is smaller than the intrinsic mean free path (~52 nm) then γ will increase linearly with the inverse of the grain diameter. This arises from the fact that grain boundaries interrupt the free flow of electrons, so the mean free path is limited by the diameter of the grains. The present value of γ is very close to the damping value of 2.6×10^{13} s^{-1} that would be expected from a large, perfect crystal of Ag, indicating that the grain size is on the order of 50 nm or more. The grain size could be measured through the use of X-Ray Diffraction (XRD), however such measurements are beyond the scope of this work.

The bulk plasma frequency ω_p is defined as:

$$\omega_p = \left(\frac{4\pi N e^2}{m^*} \right)^{1/2}, \tag{2.15}$$

where N is the density of free carriers, e is the electron charge, and m^* is the effective electron mass. Because ω_p is a function of carrier density, its value can be used to estimate the void

fraction in the film. In view of Fig. 4 of ref. [27] (which plots the relationship between the void fraction and ω_p) it can be seen that the present film appears to be void free. If dispersion in ε_∞ were taken into account and ω_p were revised downward, it may be found that the film has as much as 5% void.

2.6.2 Thin Ag film

Because the 20 nm thick Ag film is thin enough to be transparent, film thickness must be accounted for in analysis of ellipsometric measurements. As described previously, if a film has a complex refractive index then the refractive index and thickness cannot all be uniquely determined from ellipsometry alone. Also, the thicknesses of the dielectric layers are not known precisely; this introduces two additional unknowns into the analysis. To further complicate matters ellipsometric measurements taken on transparent substrates are less accurate than those taken on Si wafers. All of these factors combine to make analysis of ellipsometric measurements impractical.

For this reason, the refractive index of the thin Ag film was calculated using a combination of transmittance and reflectance. The permittivity was fitted using an iterative numerical fitting routine based on the Newton-Raphson method in which the matrix transfer method was used to calculate the transmittance and reflectance of the structure. The starting point for the fitting routine was the measured bulk permittivity of Ag and, with each iteration, the permittivity was adjusted to minimize the discrepancy between the model and the measured data. In only a few iterations it was possible to match the model to within the measurement error. This point by point fitting routine was repeated independently for each wavelength.

In this way, the thickness of the Ag film was determined to be 19.7 nm and the permittivity was fitted to the Drude model. The Drude parameters used were identical to the bulk film except for $\gamma_1 = 8 \times 10^{13}$ s^{-1}. This difference is due to either increased surface scattering in the thinner film or a smaller grain size. The complex permittivity is shown in Fig. 2.4 (d), and the transmittance and reflectance are shown in Fig. 2.5. These values form the basis of the nonlinear characterization of these films by pump-probe spectroscopy.

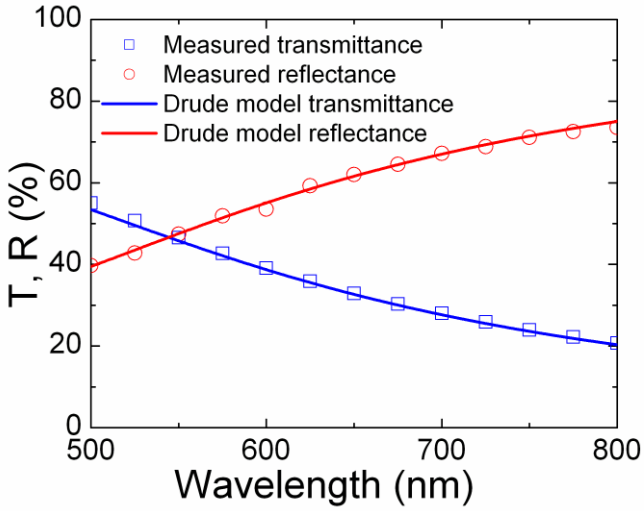

Figure 2.5 Measured transmittance and reflectance of 20 nm Ag film, with Drude model fit

2.6.3 Nonlinear characterization

WLC pump-probe measurements were carried out on the thin Ag film with incident fluences of 50, 37.5, 25, and 12.5 J/m^2 at a pump wavelength of 650 nm and 68 J/m^2 at 550 nm; all measurements were taken at a single spot on the Ag film. Figure 2.6 a, b shows the evolution of the nonlinear transmission and reflection of the film with a pump wavelength of 650 nm and a

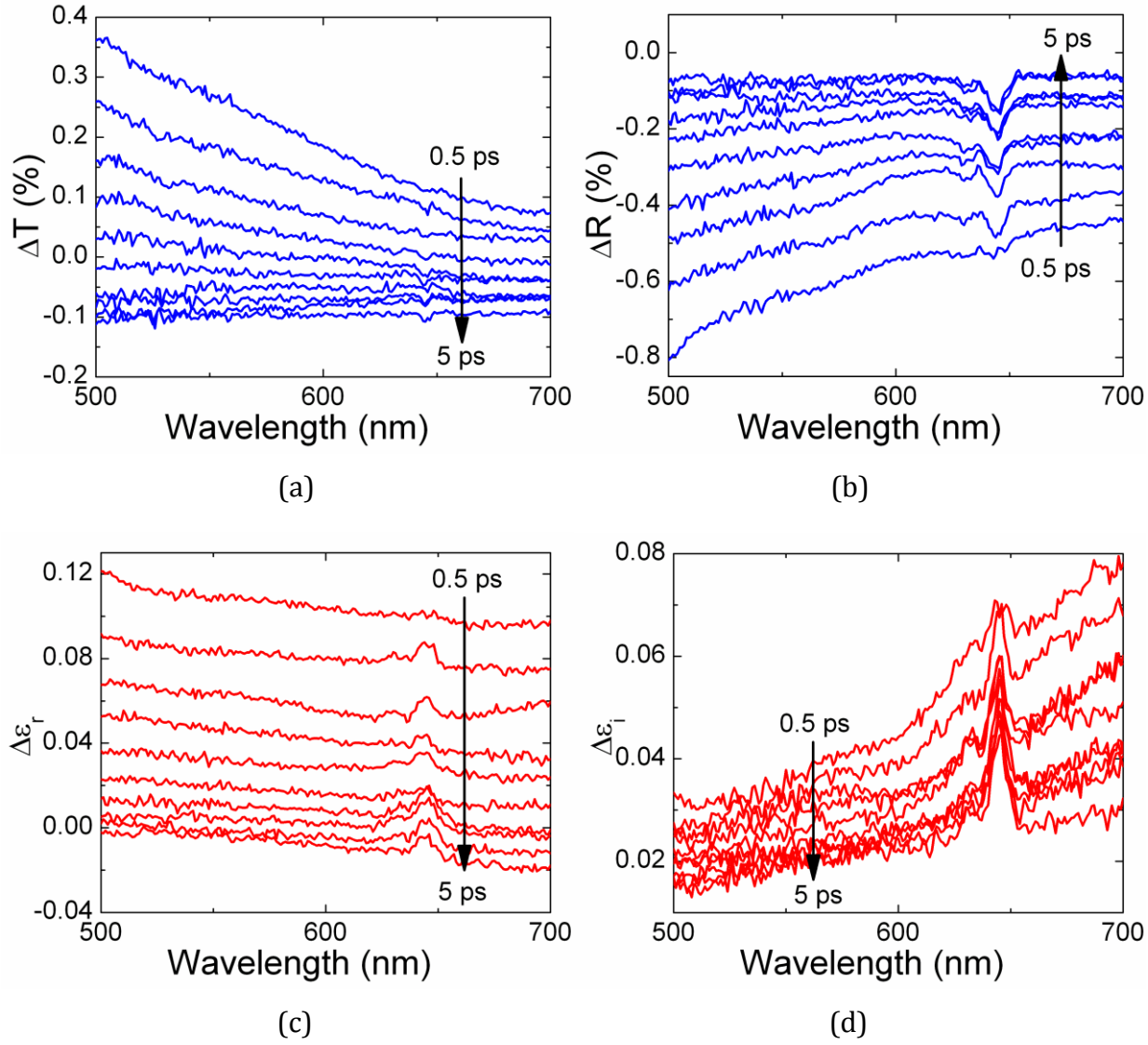

Figure 2.6 Evolution of (a) transmittance, (b) reflectance, (c) real part of permittivity, (d) imaginary part of permittivity of 20 nm thick Ag film from 0.5 ps to 5 ps after 50 J/m^2 pulse

fluence of 50 J/m^2, starting at a delay of 0.5 ps and ending at a delay of 5 ps. The corresponding evolutions of ε_r and ε_i as shown in Fig. 2.6 c, d were calculated using the same point-by- point fitting routine as for the linear data: at every wavelength and time delay the values of ε_r and ε_i were fitted to the modified transmittance and reflectance. This fitting is more robust than the commonly used method introduced by Rosei [14, 57], in which the change in permittivity is

calculated directly from the gradients of the transmittance and reflectance because the present method takes the reflectances of the entire structure into account, not just that of the Ag film. Also, it is not limited to small perturbative changes. The features in the spectra at 650 nm in these measurements are caused by scattered light from the pump beam that could not be perfectly subtracted.

From this complex permittivity data the temporal and spectral behavior can be extracted. The temporal behavior can be described entirely in terms of the two-temperature model (TTM) [57]:

$$C_e(T_e)\frac{dT_e}{dt} = -G_1(T_e - T_l) + P(t) \tag{2.16a}$$

$$C_l\frac{dT_l}{dt} = G_1(T_e - T_l) - G_2(T_l - T_e) \tag{2.16b}$$

where T_e, T_l, and T_a are the electron, lattice, and ambient temperatures, $C_e(T_e)= 65\times T_e$ [J/m^3 K] is the temperature dependent electron specific heat , C_l =2.4× 10^6 [J/(m^3 K] is the lattice specific heat, G_1 and G_2 [W/(m^3 K)] are the electron-phonon coupling and ambient coupling constants, and $P(t)$ [W/m^3] is the absorbed power density. The equation for C_e holds for temperatures less than about 5000 K [108], which is true for all measurements made here; the maximum electron temperature reached in the present experiments is on the order of 1400 K. Heat diffusion is neglected in the transverse dimension of the Ag film, which is assumed to have constant temperature. This is a good approximation because, with a Fermi velocity of 1.38 μm/ps [27], there is sufficient time for the hot electrons to distribute through the thickness of the film at time scales shorter than can be resolved with the present setup. Lateral heat diffusion is included in

the G_2 term of Eq. (2.16b). This term is included in the lattice temperature equation even though it is dominated by electron heat diffusion because electrons traveling near the Fermi velocity require on the order of 40 ps to traverse the probe region. Since it is assumed that the temperature seen by the probe is constant, thermal diffusion is only relevant at time scales longer than it takes for the electrons and phonons to reach thermal equilibrium. By including this term in the equation governing the lattice temperature instead of that for the electron temperature, spurious transient effects are avoided and the effective system behavior is captured. Figure 2.7

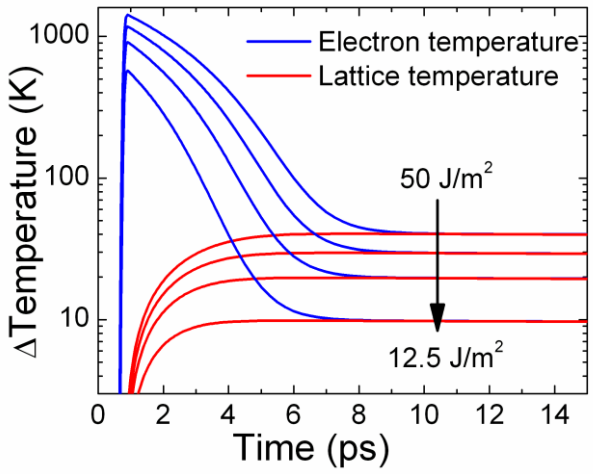

Figure 2.7 Evolution of electron and lattice temperatures of 20 nm thick Ag film calculated by the two temperature model for pump fluences 50, 37.5, 25, and 12.5 J/m^2 (semilog scale)

shows the TTM dynamics for each of the input fluences used, assuming initial temperatures $T_e = T_l$ = 300 K. These curves were calculated assuming that all the energy that is not transmitted or reflected is absorbed and converted directly into thermal energy in the electron motion.

The coupling constants for the TTM were extracted from the decay rates of the complex permittivity shown in Fig. 2.6 using a global fitting routine where the kinetics were assumed to

be governed by similar decay processes across the different wavelengths and only the time constants were allowed to vary. Based on these measurements the electron-phonon coupling rate was found to be $G_1 = 3.0\times10^{16}$ W/(m^3 K), which is somewhat smaller than the value 3.5×10^{16} reported previously in the literature [51, 109]. The rate of dissipation from Ag phonons to the surrounding environment is strongly dependent on the structure, film thickness, and dielectric material; in this particular film the rate is $G_2 = 5\times10^{14}$ W/(m^3 K).

In the frequency domain, the measured complex permittivity $\varepsilon_r + i\,\varepsilon_i$ was fitted at each time delay to the Drude model by allowing the parameters ε_∞ , ω_p, and γ to vary with electron and lattice temperature. This was accomplished in two stages. First, the response due to the electron temperature was extracted from the measurements in the neighborhood of 1 ps delay, at which time the change in electron temperature is near its maximum and the change in lattice temperature is still small. Second, the response due to the lattice temperature was extracted from the measurements after 6 ps, when the electrons have reached thermal equilibrium with the lattice.

The response of ε_i is treated here first. At both time scales the response of ε_i was determined to be due primarily to the temperature dependence of γ, which can be described as:

$$\begin{aligned}\gamma_1\left(T_l(t),T_e(t)\right) = 5.12\times10^{13} + (8.5\pm1.0)\times10^{10}T_l(t) \\ + (3.0\pm0.2)\times10^{6}T_e^2(t)\end{aligned}. \qquad (2.17)$$

The interband contribution to ε_i that has been investigated in depth in other studies [57, 60, 63] does not contribute to the present measurements because the interband contribution is highly

localized around the interband transition frequencies, outside the range of the present measurements.

The response of ε_r is more complex, and involves contributions from ε_∞ and ω_p. First, ω_p was assumed to be independent of electron temperature, so the response at 1 ps could be attributed solely to changes in ε_∞. This is physically reasonable because changes in ε_∞ should mainly arise from interband contributions while changes in ω_p could arise from effects such as band shifting that are more closely related to changes in the lattice temperature. Due to the Kramers-Krönig relation, changes in ε_i induce a spectral dispersion in ε_r that can not be reproduced by assuming that ε_∞ is frequency independent. Including the exact contributions of the different interband transitions would add additional complexity to the model and is out of the scope of this paper. Instead a frequency dependent term was introduced:

$$\varepsilon_\infty\left(\omega, T_e(t)\right) = 4.0 + \left(\left(3.0 \pm 0.2\right)\times 10^{-8} + \left(1.3 \pm 0.1\right)\times 10^{-39}\omega^2\right)\times T_e^2(t). \qquad (2.18)$$

The frequency dependent term is in the form of a two-term Cauchy equation. This dispersion depends strongly on the fact that there is no electron temperature dependent component of ω_p; if such dependence exists, this dispersion will change significantly.

After 6 ps, changes in ε_∞ and ω_p, both contribute to the response of ε_r. Since both terms have a frequency dependence, it is difficult to distinguish between the two. However, there must be two different origins to changes in ε_r because the response changes from positive to negative at about 5 ps and because the response is stronger at lower frequencies after this point. Thus, it seems clear that changes in ε_∞ are not enough to explain the observed response of ε_r.

In order to place bounds on the relative magnitudes of the contributions of ε_∞ and ω_p, it was assumed that the slope of the dispersion of ε_∞ due to the change in lattice temperature would be greater than zero and within a factor of two of the dispersion due to electron temperature. The measured frequency dependence of ε_r was then fitted with ε_∞ and ω_p. If ε_∞ is assumed to be dispersionless, the resulting expressions are:

$$\varepsilon_\infty\left(T_l(t)\right) = 3.94 + (1.7 \pm 1.2) \times 10^{-4} T_1(t) \tag{2.19a}$$

$$\omega_p\left(T_l(t)\right) = 1.374 \times 10^{16} + (1.8 \pm 0.5) \times 10^{11} T_l(t) \tag{2.19b}$$

If, on the other hand, the slope of the dispersion of ε_∞ is assumed to be double that of the electron temperature dependence, the resulting expressions are:

$$\varepsilon_\infty\left(\omega, T_l(t)\right) = 3.94 + \left(0.4 + 6.0 \times 10^{-32} \omega^2\right) \times (1.5 \pm 1.0) \times 10^{-4} T_1(t) \tag{2.20a}$$

$$\omega_p\left(T_l(t)\right) = 1.374 \times 10^{16} + (1.6 \pm 0.4) \times 10^{11} T_l(t) \tag{2.20b}$$

where the dispersion term in ε_∞ was chosen so that its magnitude would be 1 in the center of the frequency range, so that the magnitudes of the dispersive and non-dispersive temperature dependences can be directly compared. As expected, the uncertainty in these equations is quite large. However, it is apparent that uncertainty in the degree of dispersion in ε_∞ is less a contributing factor than the uncertainty in the measurements themselves. This is due to the fact that changes in ω_p appear to have a greater contribution to the nonlinear response than changes in

ε_∞ after the electrons and lattice have reached thermal equilibrium. The dominance of ω_p also explains why there is a sign change in $\Delta\varepsilon_r$.

The constant terms in Eqs. (2.18-2.20) were set so that at room temperature (T_l = T_e = 300 K) the Drude parameters would have the values ε_∞ = 4 and ω_p = 1.38×10^{16} s^{-1} taken from the linear characterization measurements in the preceding section.

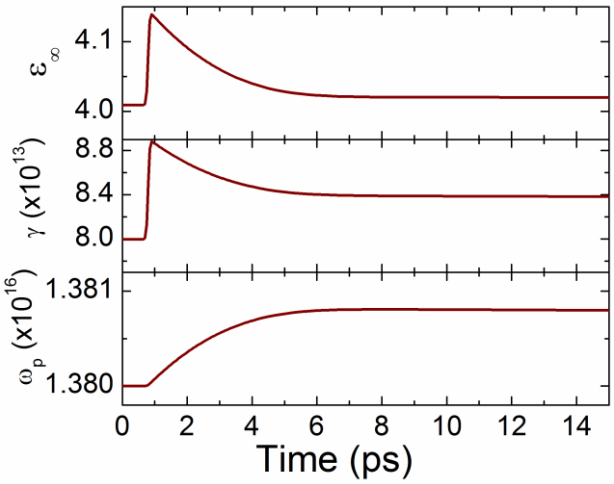

Figure 2.8 Evolution of Drude parameters (upper) ε_∞, (middle) γ, and (lower) ω_p in 20 nm thick Ag film for 50 J/m^2 pump fluence

Equations (2.17-2.20) can be combined into a single set of equations to describe the full nonlinear response in terms of electron and lattice temperatures:

$$\varepsilon_\infty\left(\omega, T_l(t), T_e(t)\right) = 3.94 + \left(-0.26 + 4.0\times10^{-16}\omega\right)\times \left\{(1.5\pm1.0)\times10^{-4}T_1(t) + (4.5\pm0.5)\times10^{-8}T_e(t)\right\} \tag{2.21a}$$

$$\omega_p\left(T_l(t)\right) = 1.374\times10^{16} + (1.6\pm0.4)\times10^{11}T_l(t) \tag{2.21b}$$

$$\gamma_1(T_l(t), T_e(t)) = 5.12\times10^{13} + (8.5\pm1.0)\times10^{10}T_l(t) + (3.0\pm0.2)\times10^{6}T_e^2(t) \quad (2.21c)$$

The error bars in these equations represent the range of values for each of these parameters that bound the measured results; that is, all of the measured data falls within the region defined by the ranges of these parameters. A more accurate estimate of the fit of these equations could be accomplished using mean square error; however, these calculations were not done here because of the difficulty of filtering out the error due to leaking pump energy (observable as a peak in the data around 650 nm) and because of a periodic variation that appears in the data (not shown here) that is most likely attributable to noise in the probe beam.

The temporal evolution of these parameters can be seen in Fig. 2.8 for a pump fluence of 50 J/m^2. As shown in Fig. 2.9, these equations, which were extracted from the 50 J/m^2 pump fluence, also describe well the changes in both the time and frequency domains for all the other pump fluences at both pump frequencies. The measurement at 550 nm demonstrates the consistency of the above model across pump wavelengths, confirming the fact that the observed effects are purely thermal in character. Hence, though there is some uncertainty in the exact magnitudes of the individual contributions this set of equations can be used to describe the nonlinear optical response of this thin Ag film. As such, it is useful for designing more complex multilayer structures incorporating this nonlinear optical response.

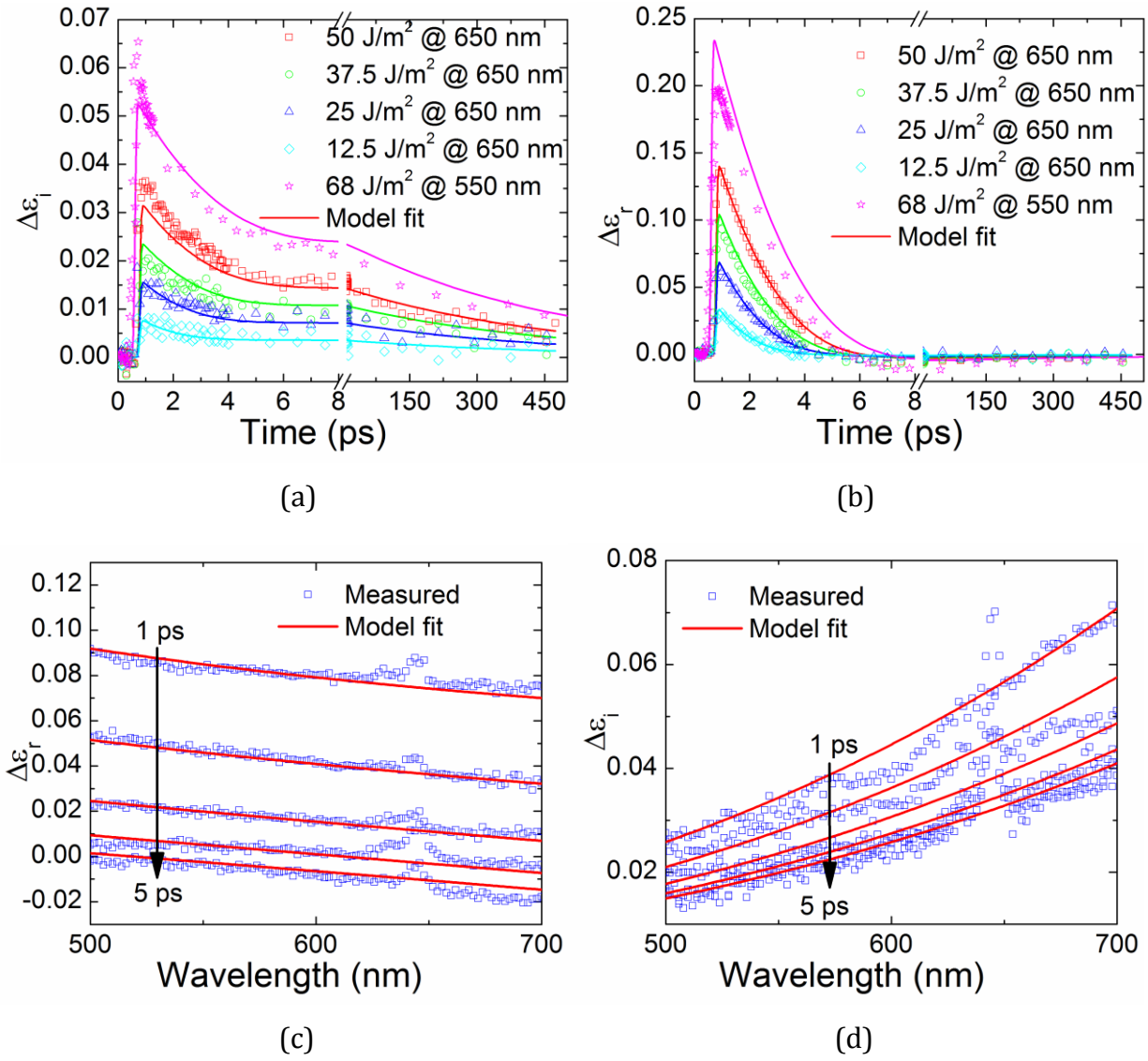

Figure 2.9 Evolution of (a) real and (b) imaginary parts of Δε of 20 nm thick Ag film with specified pump wavelength and fluence; probe wavelength is 500 nm. Solid lines represent Drude/TTM fits. (c) Real and (d) imaginary parts of Δε at various times after pump pulse for 50 J/m^2 pump at 650 nm

The values of the parameters reported from these measurements are expected to change slightly from film to film due to variations in deposition conditions, film thickness, and exposure to air. Measurements of comparably thick Ag films on glass with no protective coating have shown identical qualitative behavior with similar magnitude to the present measurements. Hence, we are

quite confident about the reproducibility of the contributions to the NLO response measured in our samples.

Further discussion of the nature and physical cause of each of these effects follows in the next section.

2.7 Nonlinear optical processes in Ag

There are at least five distinct contributions to the nonlinear response of a thin Ag film; these contributions correspond to the five temperature dependent terms found in Eq (2.21). Figure 2.10 illustrates, using the model of a 50 J/m^2 pump pulse at 650 nm, how each of these terms contributes uniquely to the observed changes in the complex permittivity.

First, Figs. 2.10a, b show the distinction between the contributions to the permittivity that are dependent on the lattice temperature $T_l(t)$ and those dependent on the electron temperature $T_e(t)$. The change in permittivity was calculated as follows. First, $T_l(t)$ and $T_e(t)$ were calculated from the TTM (corresponding to the top curves of Fig. 2.7). From these, the Drude parameters were calculated using Eq (2.21). For instance, $\varepsilon_\infty(\omega, T_l(t), T_e = 300)$ was used to isolate the lattice temperature dependent contribution of ε_∞, and $\varepsilon_\infty(\omega, T_l = 300, T_e(t))$ was used to isolate the electron temperature dependence. The other two Drude parameters, ω_p and γ_1, were calculated similarly. The Drude parameters were then inserted into Eq. (2.6) to calculate the change in complex permittivity over time. It can be seen that before thermal equilibrium is reached the high temperature of the electron cloud produces a large effect, but after equilibrium the lattice contribution is the dominant one.

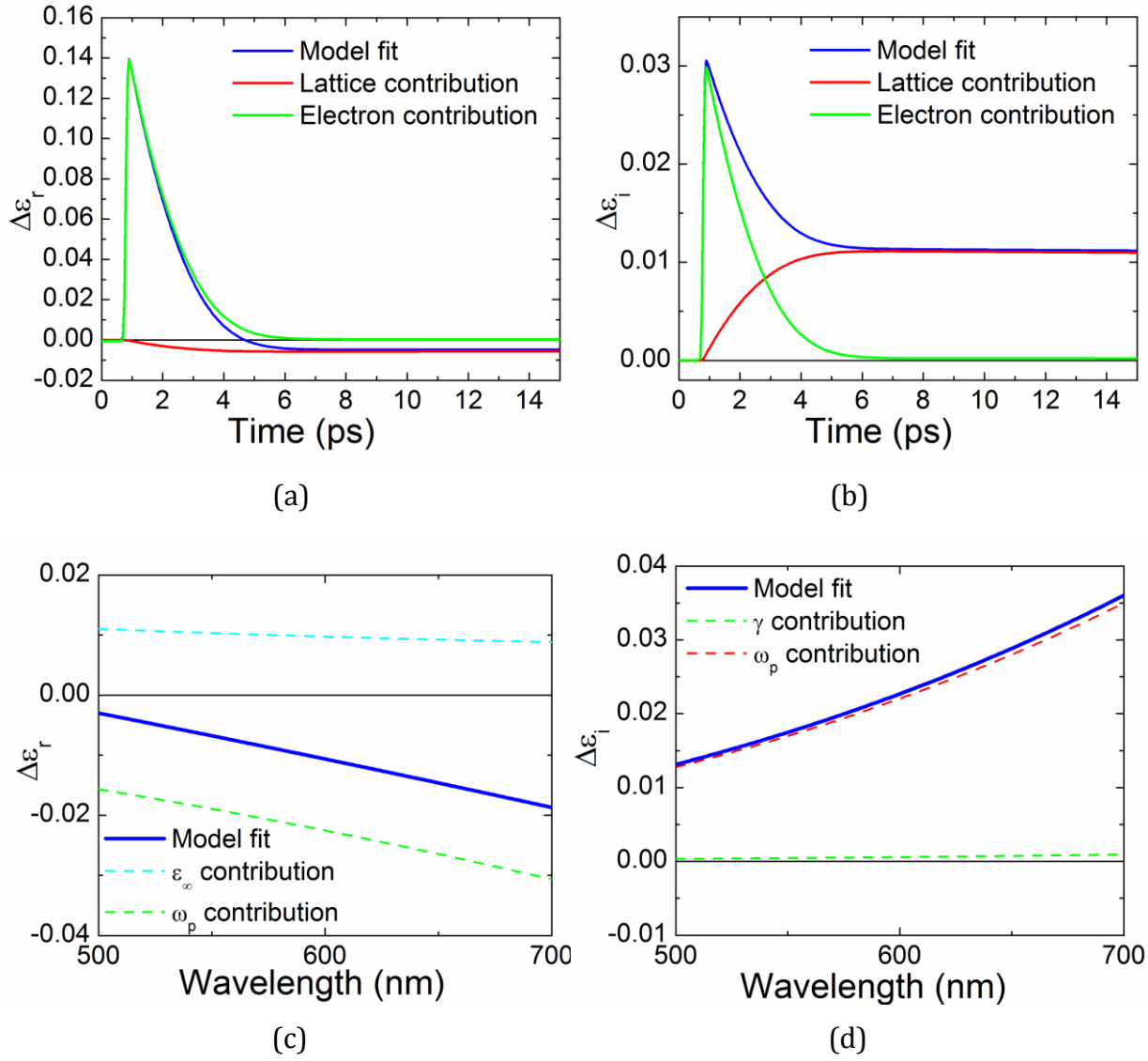

Figure 2.10 Evolution of (a) real and (b) imaginary parts of Δε of 20 nm thick Ag film over time for 50 J/m^2 pulse, and breakdown of electron and lattice contributions to nonlinearity. (c) Real and (d) imaginary parts of Δε 1 ps and 10 ps after pump pulse and breakdown of Drude parameter contributions to nonlinearity

Figures 2.10c, d show the contributions of each of the Drude parameters. Spectra of ε_r and ε_i are shown at a delay of 10 ps, after thermal equilibrium between the lattice and electron cloud has been reached. Figure 2.10c shows that the contribution due to ω_p is dominant over that of ε_∞ in the response of ε_r, as was described earlier. Figure 2.10d shows that, while there is some slight

contribution of ω_p to the response of ε_i, it is negligibly small. Thus, the assumption that the nonlinear response of ε_i can be calculated solely based on changes in γ is justified.

The physical cause of each contribution is now discussed in turn.

2.7.1 Interband effects

In the interband regime the behavior is typically attributed to three transitions. Two transitions, namely from the *d*-band to the *p*-band and from the *p*-band to the *s*-band, occur near the *L* point in the Brillouin zone [16, 17, 57]; the third transition is near the *X* point [18, 110]. All of these transitions fall well inside the ultraviolet spectrum, so for applications in the visible spectrum the only observable effect is via the Kramers-Krönig relation. This is the ε_∞ term of ε_r, [22, 55, 110].

Several different temperature dependent interband effects contribute to the observed optical properties [15]. The first is Fermi smearing, in which the distribution of electron energies around the Fermi energy is spread out. This leads to a broadening of the absorption band with increasing temperature [16, 17, 55, 57, 111] and an increase in the value of ε_∞. It has been shown [55] that the change in permittivity is proportional to the total energy contained in the electron cloud. An important distinction is that the energy is not directly proportional to the electron temperature because the electron specific heat is itself a function of temperature. Neglecting the electron-lattice coupling in Eq. (2.16a) and integrating gives

$$\frac{65T_e^2}{2} = E_e \tag{2.22}$$

where E_e is the total thermal energy contained in the electron cloud. In terms of temperature, then, Fermi smearing follows T_e^2, as can be seen in Eq. (2.21a).

The second interband effect is band shifting, which is caused by thermal expansion in the silver crystals and follows the lattice temperature [18]. As the crystals heat up and expand, the energy levels of the valence and conduction bands, as well as the Fermi energy, shift. This leads to a corresponding shift in the absorption spectrum, which can again be observed in ε_∞ through the Kramers-Krönig relationship. The specific heat of the lattice is constant within this temperature range, so it is expected that this effect follows T_l; this again can be seen in Eq. (2.21a).

Other effects, such as those listed in [15], may contribute to the interband nonlinear response, but in this wavelength range their effects can not be separated from Fermi smearing and band shifting for the present set of measurements.

2.7.2 Intraband effects

The intraband regime is described by the Drude model, as shown above, with temperature dependent parameters γ and ω_p.

At least three mechanisms, electron-phonon scattering, electron-electron scattering, and electron-surface scattering, contribute to γ. Electron-phonon scattering is the mechanism by which energy is transferred between electrons and the lattice and vice versa, and is the largest contribution to damping at room temperature. The scattering rate is proportional to the lattice temperature T_l due to an increase in the number of phonons [22, 55, 57, 109, 111]. Holstein's expression for the temperature dependence of electron-phonon interaction is [22]:

$$\gamma_{e-ph} = \gamma_0 \left(\frac{2}{5} + 4 \left(\frac{T_l}{\Theta} \right)^5 \int_0^{\Theta/T_l} \frac{z^4 dz}{e^z - 1} \right), \tag{2.23}$$

where Θ = 220 K is the Debye temperature. For $T_l > \Theta$, this equation can be approximated well by a linear function of T_l:

$$\gamma_{e-ph} = \gamma_0 \left(7.5 \times 10^{-2} + 4.43 \times 10^{-3} T_l \right) \tag{2.24}$$

The value for γ_0 can be extracted from the Drude parameters of bulk Ag, in the temporal range where the electron-electron contributions are negligible. As stated previously, γ_1=2.73×10^{13} s^{-1} for our bulk film, so γ_0=1.94×10^{13} s^{-1}. Assuming that this value holds for the 19.7 nm-thick film as well, then $\Delta\gamma_1/\Delta T_l$ = 8.6×10^{10} s^{-1}K^{-1}. This matches well with the calculated value of 8.7×10^{10} s^{-1}K^{-1} from Eq. (2.21c).

Electron-electron scattering is expected to have a thermal dependence based on T_e^2 [22]:

$$\gamma_{ee} = \frac{1}{12} \pi^3 \Gamma \Delta \left(1/\hbar E_F \right) \left[\left(k_B T_e \right)^2 + \left(\hbar\omega / 2\pi \right)^2 \right], \tag{2.25}$$

where Γ = 0.55 is the average of the scattering probability over the Fermi surface, Δ = 0.75 is the fractional Umklapp scattering, and E_F = 5.5 eV is the Fermi energy. Typically the temperature dependent term is neglected because it does not become significant until T_e > 1000; since this threshold is exceeded in the present system, this temperature dependence must be considered. It follows from Eq. (2.25) that $\Delta\gamma/\Delta T_e^2$ = 2.2×10^6 s^{-1}K^{-2}, compared to 2.9×10^6 s^{-1}K^{-2} from Eq.

(2.21c). A surface scattering contribution may in part make up some of this discrepancy; it would require taking a series of measurements on samples with carefully controlled surface morphologies to verify this.

Surface scattering results from diffuse reflection of electrons off the surface of the film; the strength of this contribution is morphology and thickness dependent, affected particularly by the surface roughness [26]. This accounts for a large part of the difference in γ between the bulk Ag film and the thin Ag film; however, the nonlinear contribution is unclear.

The thermal dependence of ω_p is not a well documented phenomenon because it is difficult to distinguish from other thermal effects, as stated earlier. Different values have been reported at different temperatures, but the precision has been low [23]. Variations in ω_p have been attributed as the cause of certain "ringing" phenomena in nanoparticles, but it is difficult to quantify the effect from such experiments [112]. Considering Eq. (2.15), there are two possible explanations for the variation: a change in carrier concentration and a change in electron effective mass. Considering the thermal expansion of Ag, the carrier concentration might be expected to decrease with increasing lattice temperature. However, only an increase in ω_p is observed in the present experiments so this is not a sufficient explanation. It is possible that as the band structure changes the effective mass is also modified; the precise determination of the causes of this effect will require further experiments and is beyond the scope of this research.

The contributions to the nonlinear response of Ag can be categorized in several different ways: (1) whether it arises from interband or intraband effects; (2) whether it is electron temperature or

lattice temperature dependent; and (3) whether the observed change occurs predominantly in the real or imaginary permittivity. Table (2.1) gives a summary of the nature of each contribution.

Table 2.1 Summary of contributions to nonlinearity in Ag

Source	Drude parameter	Interband/ Intraband	Electron/ Lattice	Effect observed in $\varepsilon_r/\varepsilon_i$
Fermi smearing	ε_∞	interband	electron	ε_r
Band shifting	ε_∞	interband	lattice	ε_r
Electron-phonon	γ_1	intraband	lattice	ε_i
Electron-electron	γ_1	intraband	electron	ε_i
Plasma frequency	ω_p	intraband	lattice	ε_r

The WLC pump-probe measurements presented in this were used to identify five different contributions to the nonlinear processes of Ag: Fermi smearing, band shifting, electron-phonon scattering, electron-electron scattering, and changes in bulk plasma frequency. Open questions remain about the contributions of electron-surface scattering and the cause of the shift in the bulk plasma frequency. The model developed based on these measurements describes well the behavior of a semi-transparent 20 nm Ag sample under different pump fluences and excitation wavelengths. The results of this analysis will aid in the rigorous design of more complex structures that take advantage of the nonlinear optical properties of Ag, such as one dimensional metal-dielectric photonic crystals or induced transmission filters.

Chapter 3. Optical properties of one-dimensional metal-dielectric photonic band-gap structures with low index dielectrics

3.1 Introduction

The large difference in permittivity between metals and dielectrics makes it possible to create compact structures, such as metal-dielectric photonic band gap (MDPBG) devices [113], that have larger optical band gaps than is possible with combinations of dielectrics [114, 115]. These structures consist of a set of resonant metal/dielectric/metal Fabry-Perot resonators with very low finesse. In spite of containing a total thickness of metal much greater than its skin depth at visible wavelengths, at the proper dielectric thicknesses, resonant tunneling opens up transmission windows that allow for high transmission to be achieved in regions where metals are typically opaque [70]. Outside this range the MDPBG acts largely as a bulk metal, thus reflecting any incoming electromagnetic field with a frequency smaller than the edge of the band gap. This makes MDPBGs attractive for a wide variety of applications such as heat and electromagnetic shielding, for sensor and eye protection, as transparent electrodes, and as more recently suggested, superlenses permitting optical imaging at length scales well below the diffraction limit [116], or as highly nonlinear optical filters [96]. For linear filtering applications MDPBGs offer a tradeoff with conventional dielectric/dielectric multilayer filters in that, while the peak transmission will be lower in an MDPBG because of absorption in the metal, the MDPBG is able to give better out of band rejection over a larger spectral range.

The variety of applications in which MDPBGs could be used makes it desirable to develop a better understanding of the design paths to produce a given set of optical properties. As with any other optical window, high transmission with controlled spectral and angular bandwidth are

commonly sought properties. While the reports of fabricated MDPBGs are relatively scarce, e.g. [69, 75, 78, 79, 81, 82, 85-88], the highest transmission and broadest spectral bandwidths have been reported in structures that use high refractive index dielectric materials, such as TiO_2 [85] and Indium Tin Oxide (ITO) [81]. The use of these oxides with a large refractive index reduces the electric field density within the absorptive metal layers and allows for high transmission to be achieved. However, they also require a partial pressure of oxygen in the deposition chamber for consistent depositions because they dissociate during evaporation, leading to the potential of oxygen diffusion and the eventual corrosion of the metal layers in the MDPBG unless anticorrosion layers are used. On the other hand, with lower index dielectrics such as SiO_2 or Al_2O_3, the conditions for resonant tunneling tend to cause several narrow band transmission peaks to appear within the spectral range of the structure. The spectral characteristics of such MDPBGs are less desirable for most of the proposed applications, in particular those requiring large spectral and angular bandwidths. The limited pool of high index materials also makes it desirable to explore the limitations of the use of lower index materials, which for a range of applications, such as nonlinear optical filters, may have more favorable characteristics in terms of optical activity, processibility and long term stability.

In this we explore some of the consequences of using lower index dielectric materials and describe design techniques to minimize some of the detrimental effects. The high index contrast between the metallic and dielectric layers in all MDPBGs makes it possible to easily tune the spectral characteristics of the transmission window without increasing the number of layers required for a particular design that matches a given bandwidth. To illustrate this flexibility, we describe and demonstrate a method for producing 1D MDPBG structures containing Ag and relatively low refractive index dielectric layers that show the characteristics of a flat-passband

optical filter. Such a structure would have a transmission comparable to that of a periodic structure but would minimize the effects of the individual resonance peaks that are characteristic of moderate refractive index dielectrics, and lead to transparent optical filters with a large field of view (FOV) that are capable of broadband applications within the visible spectrum. To validate this approach we fabricated an MDPBG using Al_2O_3 as the dielectric. The fabricated structure shows 53% ± 3% transmission over a 150 nm bandwidth between 475 nm and 625 nm, with an angular change of less than 5% when the angle of incidence was varied by ± 30^o with respect to normal incidence. We also show that the optical properties of such devices are insensitive to temperature changes up to 150 ^oC and demonstrate environmental stability over a period of ten months.

3.2 Thin film fabrication and characterization

3.2.1 Materials

For the present work Ag was again used because, in contrast with Au or Cu, the onset for interband transitions lies well into the UV at 3.9 eV. Its optical properties from the visible throughout the IR range are therefore dominated by the free-electrons in the conduction band, which assures a very low refractive index throughout this range. We chose Al_2O_3 as the dielectric because it has a moderate refractive index and does not require a partial pressure of oxygen during electron-beam (e-beam) deposition. Such oxygen is required for some dielectrics, but it can cause significant corrosion of underlying Ag layers if the Ag is exposed directly to the oxygen.

3.2.2 Deposition

Thin films of the selected materials were fabricated on 1 mm thick glass slides or on Si wafers using a Kurt J. Lesker Axxis e-beam deposition system. The substrates were cleaned ultrasonically in deionized water, acetone, and isopropanol, then annealed in a vacuum oven at 105° C for one hour. During all e-beam depositions the substrates were actively cooled and held at room temperature. Depositions were made in vacuum with pressure less than 2×10^{-6} Torr at a rate of 0.1 nm/s for Al_2O_3 and 0.02 nm/s for Ag. No Ti adhesion layer was used.

3.2.3 Determination of optical constants

The optical constants of the selected materials were measured using spectroscopic ellipsometry, as described in 1. The refractive index of Al_2O_3 was obtained from a 30 nm thick film deposited on Si. The refractive index of Al_2O_3 can vary significantly depending on deposition and environmental conditions [117], so it is necessary to characterize it for each deposition system. For our system the ellipsometric data was fitted using a Cauchy model of the form $n = A + B/\lambda^2$, where A = 1.601 and B = 5.924x10^{-3} μm^2, plotted in Fig. (3.1). The imaginary part of the refractive index was found to be negligible in the measured range.

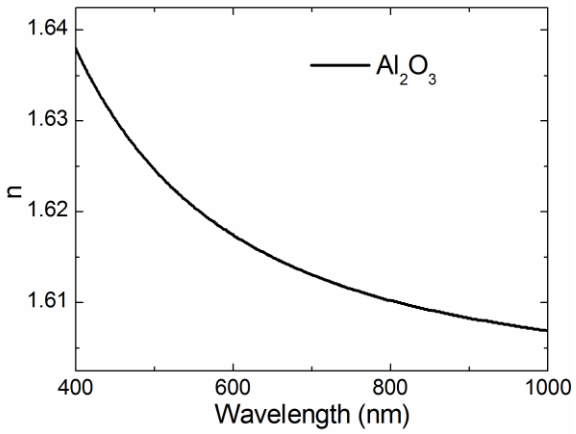

Figure 3.1 Measured refractive index of Al_2O_3

The refractive index of Ag was measured by depositing a 12 nm thick film on top of the 30 nm thick Al_2O_3 film. This was done to mirror the conditions that would be present in an MDPBG as closely as possible, since the refractive index is strongly dependent on the film thickness and the material upon which it is deposited. An SEM image of this film is shown in Fig. 3.2b. It can be seen that the film is not completely continuous, and that significant voids are present within the film. In spite of these voids the film exhibits bulk-like optical properties, as can be seen from the refractive index.

The refractive index was calculated from ellipsometric measurements and compared to the bulk refractive index of Ag from Fig. 2.4c. As can be seen in Fig. 3.2a, while both the real and imaginary parts show non-trivial departures from the bulk values, the essential trends are the same. There is no evidence of surface plasmons, which would appear as a strong increase in the real part and decrease in the imaginary part, particularly at the longer wavelengths. For the present study 12 nm was set as the minimum "continuous" film thickness because thinner films showed larger voids and greater evidence of surface plasmons.

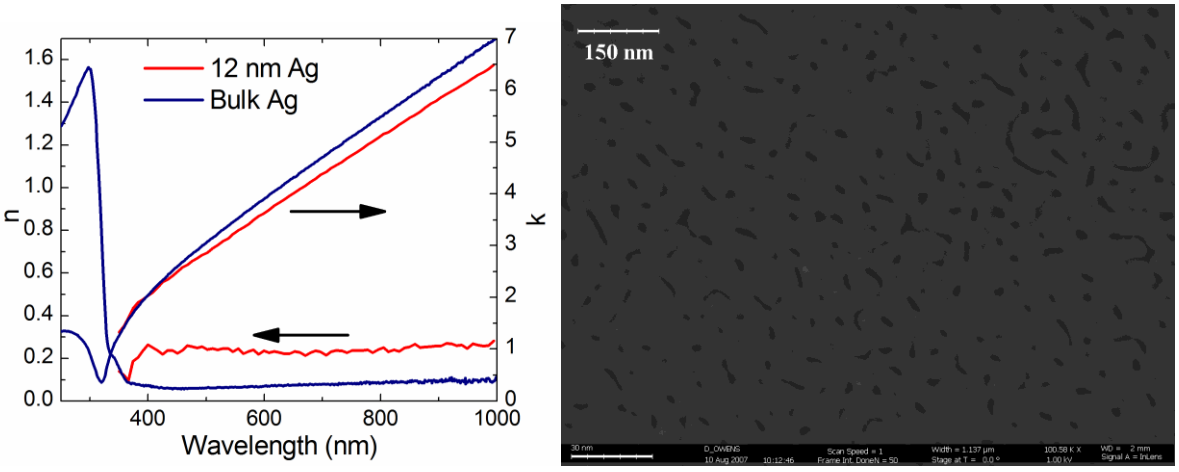

(a) **(b)**

Figure 3.2 (a) Measured refractive index of 12 nm Ag film compared to bulk Ag. (b) SEM image of 12 nm Ag film on Al_2O_3

The observed difference in the imaginary part of the refractive index of the 12 nm thick Ag film can be attributed to the presence of the voids. As described in section 2.6.1, the bulk plasmon frequency is proportional to the density of free carriers in the film; the presence of voids naturally causes this density to drop. The change in the real part is due to an increase in the damping parameter of the Drude model, similar to what was observed in section 2.6.2. The damping parameter increases as the film gets thinner because electron surface scattering plays an increasingly important role. The presence of voids also limits the mean free path of the electrons, further contributing to the increase in damping.

It should be noted that the analysis of the ellipsometric data of the Ag film is a best effort process. As noted in section 2.5.1, it is impossible to uniquely determine the thickness and complex refractive index of a thin absorbing film such as this one. The fit was chosen based on what is physically possible; the refractive index must be positive at all wavelengths, for instance, and the trends in refractive index are expected to be smooth and without sudden jumps above a

wavelength of 400 nm. However, though the refractive index may not be exact, it still gives a very good starting point for the analysis and design presented in the next two sections.

3.3 MDPBG design

In order to come to a better understanding of the principles of MDPBG design and the effects of individual design parameters on the resulting transmission and reflection spectra, we first performed systematic studies by varying individual design parameters. We followed this up with an optimization process that improves the transmission spectrum by independently adjusting the thickness of each layer in the structure. All simulations were done using the transfer matrix method described in section 2.3.1.

3.3.1 Design variations

The following periodic structure will be used in the discussion throughout this section:

$$\text{Air } |D^{1/2}\ M\ D^{1/2}|_n\ G \tag{3.1}$$

where M stands for a metal layer of refractive index n_m and thickness d_m, $D^{1/2}$ stands for a dielectric layer with refractive index n_d and thickness $d_d/2$, and G stands for the glass substrate. The subscript n indicates that the unit cell $|D^{1/2}\ M\ D^{1/2}|$ is repeated n times. This unit cell is commonly used to increase transmission over a unit cell of the form |DM| because the $D^{1/2}$ layers at each end of the MDPBG act as antireflection coatings[79, 81, 85].

The reference point for all simulations in this section uses n = 5 periods, n_m is the measured refractive index of bulk Ag, and n_d is the measured refractive index of Al_2O_3. The Ag thickness

d_m = 14 nm; this gives a total Ag thickness of 70 nm. The dielectric layer thickness d_d = 125 nm allows the pass band to be centered in the visible part of the spectrum. A graphical representation of this structure and the simulated transmittance, reflectance, and absorbance are shown in Fig. 3.3.

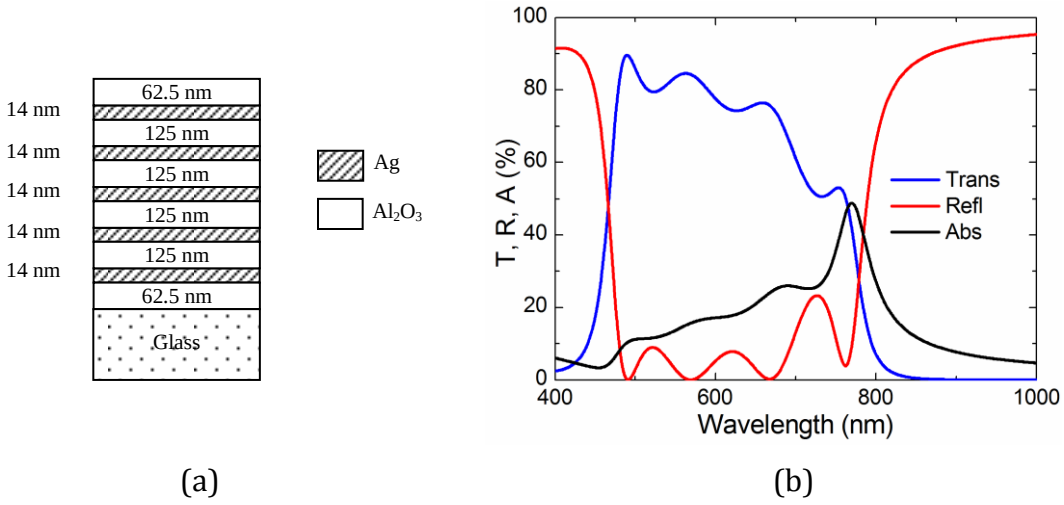

Figure 3.3 (a) Standard structure for studies of variation of parameters. (b) Transmittance, reflectance, and absorbance of standard structure

An important basic principle of MDPBG operation can be illustrated with this structure. An MDPBG can be treated as a series of resonant cavities in the dielectric layers with lossy coupling through the metal layers, and the structural resonances can be described by the tight-binding model [80, 118]. The tight binding model describes how the response of a resonant structure changes as lossy coupling is introduced. For instance, if two cavities with identical resonant frequency are joined with a lossy coupler, then in the combined response of the two cavities the shared resonance peak will split into two adjacent peaks. The distance between the peaks is governed by the amount of loss in the coupler. This effect scales with the number of cavities that

are joined together; each cavity introduces a new peak. This principle can be seen in the example MDPBG, which has four dielectric cavities and four corresponding transmission peaks.

Also, the reflectance at each transmission peak drops near to zero. This means that all of the light at these wavelengths is either transmitted or absorbed, which is one of the aspects of the ideal scenario for NLO applications (see Section 1.3).

3.3.1.1 Variation of number of periods

The first property that was varied was the number of periods; Fig. 3.4 shows the transmittance and reflectance of structures with between three and seven periods, with the five period example being the same as that shown in Fig. 3.3. As expected from the above discussion, each additional period increases the number of structural resonances; the bandwidth, however, does not change significantly. At the same time, the increasing amount of Ag in the structure leads to a decrease in the transmittance across the spectral range, particularly at longer wavelengths—though this is not as significant as might be expected, since the total thickness of Ag doubles from 56 nm in the 3 period structure to 112 nm in the 7 period structure. The advantages of using more periods are that the out of band rejection is stronger and the roll off at the band edge is steeper, particularly at the lower wavelength edge.

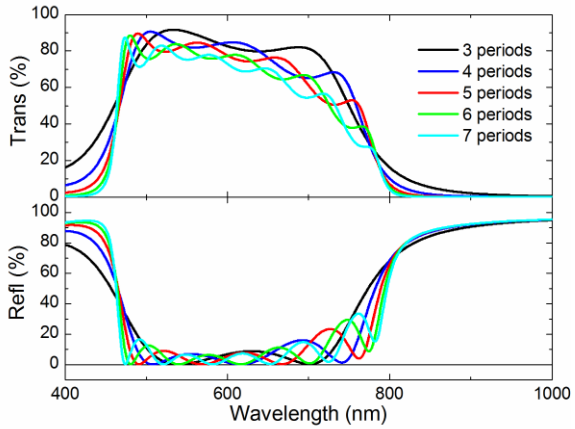

Figure 3.4 Transmittance and reflectance of structures with 3 to 7 periods

3.3.1.2 Variation of dielectric refractive index

Second, we investigated the impact of variation of the refractive index of the dielectric material. One might expect that increasing the refractive index of the dielectric will lead to a larger index mismatch between the dielectric and metal, resulting in greater reflectance at each metal/dielectric interface. We saw above that increasing the reflectance of each film increases the reflectance of the whole structure, so it might be expected that low index dielectrics would produce structures with the highest transmittance. This is not, in fact, the case. MDPBGs that make use of a low index dielectric have been shown to have lower transmission and higher reflection and absorption than their high index counterparts. To illustrate this effect, we have simulated the transmission, reflection, and absorption at normal incidence in four MDPBGs with various refractive indices. The refractive index of the dielectric layers in each of the four instances was changed by multiplying the refractive index from the Cauchy model obtained for Al_2O_3 in section 3.2.3 by constant factors s = 0.75, 1, 1.25 and 1.5. To isolate the effects of the refractive index change, we have adjusted the thickness of the dielectric layers to keep the optical path length (OPL), n_d*d_d, constant.

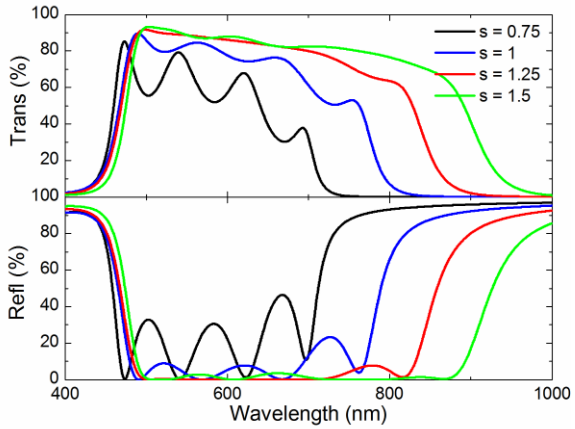

Figure 3.5 Transmittance and reflectance of structures with dielectric refractive index ranging from 0.75 to 1.5 times refractive index of Al_2O_3

The resulting trend can be seen in Figure 3.5, which shows an increase in reflection and a decrease in transmission and bandwidth as the refractive index of the dielectric layer decreases. This decrease is accompanied by an increased strength of the resonance peaks of the structure.

This counterintuitive dependence of the optical transmission can be understood as follows. The transmission through a thin metal film can be calculated from the Fresnel coefficients as

$$T = \left(\frac{4 n_d n_m \alpha}{\left(n_d + n_m\right)^2 + \left(n_d - n_m\right)^2 \alpha^2} \right)^2, \tag{3.2}$$

where

$$\alpha = e^{-i 2\pi n_m d_m / \lambda} \tag{3.3}$$

and λ is the wavelength. Throughout the visible and infrared spectra n_m is complex and dominated by the imaginary term, as can be seen from Fig. 3.2. If n_m is treated as purely imaginary then α is real, so T can be rewritten as

$$T = \left(\frac{4 n_d n_m \alpha}{\left(n_d^2 + n_m^2\right)\left(1+\alpha^2\right) + 2 n_d n_m \left(1-\alpha^2\right)} \right)^2, \tag{3.4}$$

where the first term in the denominator is real and the second term is imaginary. It can be shown that T is maximized when the real term of the denominator vanishes; that is, $(n_d^2 + n_m^2) = 0$. This index matching condition will occur around $n_d = 2.78$ for $\lambda = 500$ nm, and grows increasingly large as the wavelength increases. It can similarly be shown that reflection is minimized at this same point. Thus, since dielectrics with a high refractive index more closely approximate the index matching condition, the structural resonances are reduced so the reflection of the entire structure decreases and transmission increases.

Notably, the absorption within the structure does not change as much as the reflection, implying that there may still be room for improving the transmission through the use of more elaborate antireflection coatings. As is clear from these simulations, a unit cell of the form $|D^{1/2}\ M\ D^{1/2}|$ will produce MDPBGs with high transmission windows and moderate spectral resonances only if a small reflectivity throughout the transmission window is achieved. This is not the case when low-refractive index dielectrics are used.

3.3.1.3 Variation of dielectric thickness

The third property under consideration is the dielectric thickness. The transmittance and reflectance of structures with thicknesses ranging between 100 and 200 nm are shown in Fig. 3.6. As expected, increasing the dielectric thickness moves the resonances to longer wavelengths. At the same time, the maximum peak transmittance remains nearly constant but the average transmittance across the pass band decreases and the height of the ripples associated with the resonance peaks increases. These changes are caused by the change in the index matching condition as described in the previous section; the further into the infrared the pass band moves, the worse the index matching is between the metal and the dielectric. This indicates that these structures are most useful at shorter wavelengths; in particular, they are more suitable for visible wavelength applications than for infrared. This decrease in transmittance is due to the fact that the reflectivity of Ag increases toward longer wavelengths. The increase in reflectivity decreases the coupling from one cavity to the next, so the transmission of light through the structure is impeded. More light reflects back off the structure.

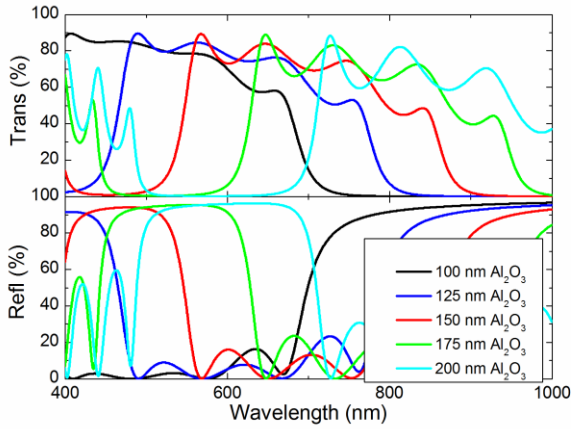

Figure 3.6 Transmittance and reflectance of structures with dielectric thicknesses ranging from 100 nm to 200 nm

3.3.1.4 Variation of Ag refractive index

The fourth parameter of interest is the refractive index of the Ag. Variations in the refractive index of the metal films may arise from the fabrication process, or may be induced in the process of NLO applications, so considering the effects of variations of this property is important. The parameter that changes most significantly from both fabrication issues and NLO response is the damping parameter γ, so the primary change in refractive index is in the real part. We studied the effects of changing the real part of the refractive index by factors of s=0.5, 1, 1.5, and 2.

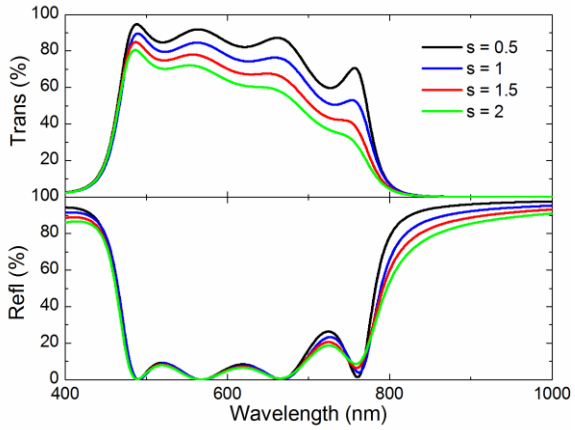

Figure 3.7 Transmittance and reflectance of structures with metal real refractive index ranging from 0.5 to 2 times that of Ag

Figure 3.7 shows the effects of this change in refractive index. The transmittance drops as the refractive index increases but the reflectance doesn't change significantly, indicating that the absorbance must increase. This is in line with the increase in absorbance of a single Ag film observed in section 2.7.

3.3.1.5 Variation of Ag thickness

The fifth variation under consideration was that of the thickness of the Ag films. The effects of this property are straightforward, as seen in Fig. 3.8 for structures with Ag layer thicknesses of 10 nm, 14 nm, 20 nm and 25 nm: increasing Ag film thickness leads to decreasing transmittance, decreasing bandwidth, and increasing reflectance. Thicker metal films are naturally more reflective. If the metal films are thick, the cavities are nearly uncoupled; thus, their resonance peaks are closely aligned and the bandwidth narrows.

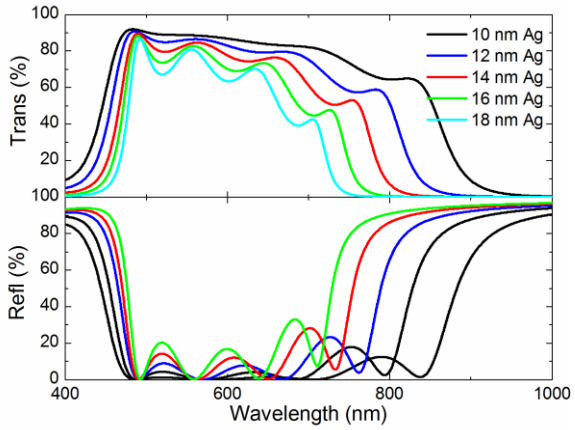

Figure 3.8 Transmittance and reflectance of structures with Ag thickness ranging from 10 nm to 18 nm

3.3.1.6 Variation of Ag film thickness and number of periods, with constant total Ag

For some applications such as RF shielding it is necessary to maintain a minimum total Ag thickness in the structure. In this section we consider the special case of maintaining a constant total amount of Ag while simultaneously varying the number of periods and the thickness of each Ag layer. In particular, we consider three structures that have four, five, and six periods with Ag film thicknesses of 17.5 nm, 14 nm, and 11.7 nm respectively; each has a total thickness of Ag equal to 70 nm. The transmittance and reflectance of each are shown in Fig. 3.9.

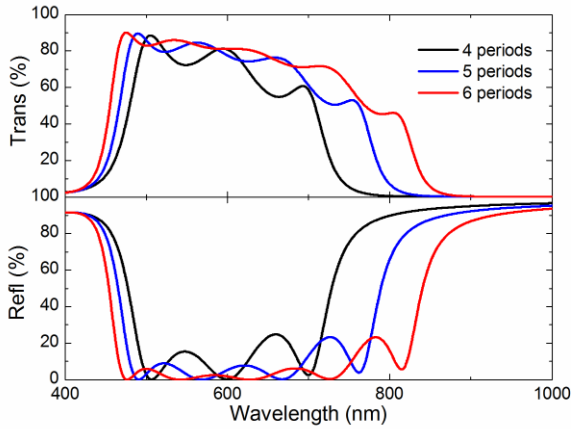

Figure 3.9 Transmittance and reflectance of structures with 4, 5, and 6 periods, each with a total Ag thickness 70 nm

The combination of decreasing the Ag thickness and increasing the number of periods has the sum effect of increasing the bandwidth and smoothing out the transmission spectrum without a decrease in total transmittance. The increase in bandwidth and smoothing of the transmission band are direct consequences of thinning the Ag layers, and the decrease in transmittance caused by increasing the number of periods is offset by the increase in transmittance caused by thinning the Ag layers. Also, the out of band rejection is approximately the same for all three structures. For this reason a structure with a greater number of thin metal layers will produce a wider bandwidth than the corresponding structure with fewer, thicker layers. The only limit to this trend is the physical limitation on the achievable minimum Ag film thickness.

3.3.2 Design optimization

The high index contrast inherent to the MDPBG and strong coupling between the resonant cavities forming it makes it possible to tune the spectral characteristics of the structure by varying the thicknesses of each individual layer, making an aperiodic structure. In this way it is possible to make a filter with desirable spectral characteristics without sacrificing the total

transmission of the structure, for instance, by smoothing out the variations caused by the resonance peaks. While analytic solutions are possible, they quickly become intractable for optimization of complex structures across a wide wavelength band so the process is better handled by a numerical algorithm.

In order to demonstrate this approach we design a structure with flat passband transmission in the wavelength range of 475-625 nm using an iterative optimization process. The optimization process first adjusts the thickness of each layer in turn with the goal of maximizing the transmission within the desired band [λ_{min}, λ_{max}], which is quantified by the metric

$$M = \sum_{\lambda_{\min}}^{\lambda_{\max}} T \,. \tag{3.5}$$

The process continues adjusting the thicknesses of each layer until the metric is maximized. The resulting structure is then used as the starting point for the second stage of optimization, which repeats the process of the first stage with the goal of minimizing the variance within the band,

$$M = \frac{1}{n-1} \sum_{\lambda_{\min}}^{\lambda_{\max}} (T - \overline{T})^2 \,. \tag{3.6}$$

The resulting structure (**AP**) and its transmission spectrum are shown in Fig. 3.10, along with the equivalent periodic structure (**P1**) of the form described in Eq. (3.1) and a periodic structure with an asymmetric unit cell (**P2**):

$$\text{Air } |DM|_5 \tag{3.7}$$

In this case the average transmission of structure **AP**, 65.3%, is slightly less than the 69.3% average for the structure **P1**; however, the variance of **AP**, 0.75%, is a significant improvement over the variance in **P1** of 24.9%. The inset of Fig. 3.10 shows the angular dependence of these three structures; structure **AP** has less than 5% variation over a 60 ^{o} field of view.

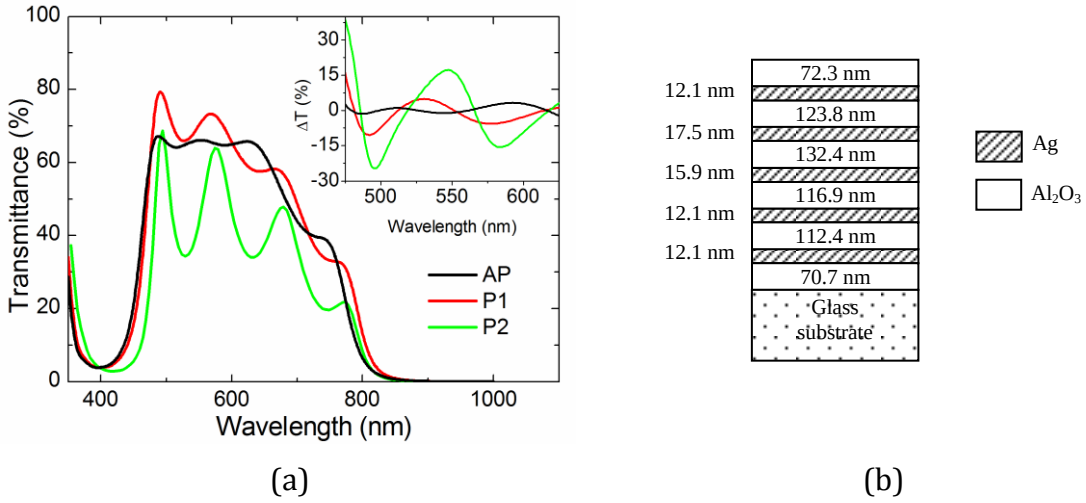

(a) (b)

Figure 3.10 (a) Transmission of aperiodic MDPBG (AP) with structure (b), along with two periodic structures (P1 and P2). (inset) Change in transmission at 30 degree angle of incidence for periodic (P1 & P2) and aperiodic (AP) MDPBGs

Given the nature of our optimization method and arbitrary selection of the metrics, it is not expected that the thickness distribution of structure **AP** will be unique. Although its optical properties cannot be correlated to changes of the thickness of individual layers, based on the properties of MDPBGs discussed in this section and on the comparison provided in Fig. 3.10, we can rationalize its structure as follows: a) the presence of thicker inner metal layers is expected to reduce the coupling strength between cavities and yield resonant peaks that are more closely

spaced together than they appear for **P1** and **P2**; b) selective thickening of dielectric layers should help in equalizing the strength of these resonance peaks; and c) because the outer layers of Al_2O_3 are still of order $D^{1/2}$, they are expected to reduce reflections between resonant peaks, similar to structure **P1**.

3.4 MDPBG Fabrication and characterization

We fabricated the aperiodic structure with flat pass band transmission from section 3.5, as well as a set of substructures, by a series of depositions as described in section 3.2.2. All transmission measurements in the visible spectrum were taken with a Cary 5E UV-vis-NIR spectrophotometer, as described in section 2.5.2.

Substructure *n* has the form

$$\text{Air } |\text{DM}|_n \text{ DG}, \tag{3.8}$$

so the first substructure consists of the initial $Al_2O_3/Ag/Al_2O_3$ layers and each subsequent substructure includes an additional Ag/Al_2O_3 pair. Figure 3.11 shows the measured transmission of each substructure compared to the simulated transmission. The transmission of the 1x substructure is less than expected because of voids and roughness in the Ag film, as seen in Fig. 3.1b. This shortfall carries through the other substructures, though the general trend clearly follows the simulations.

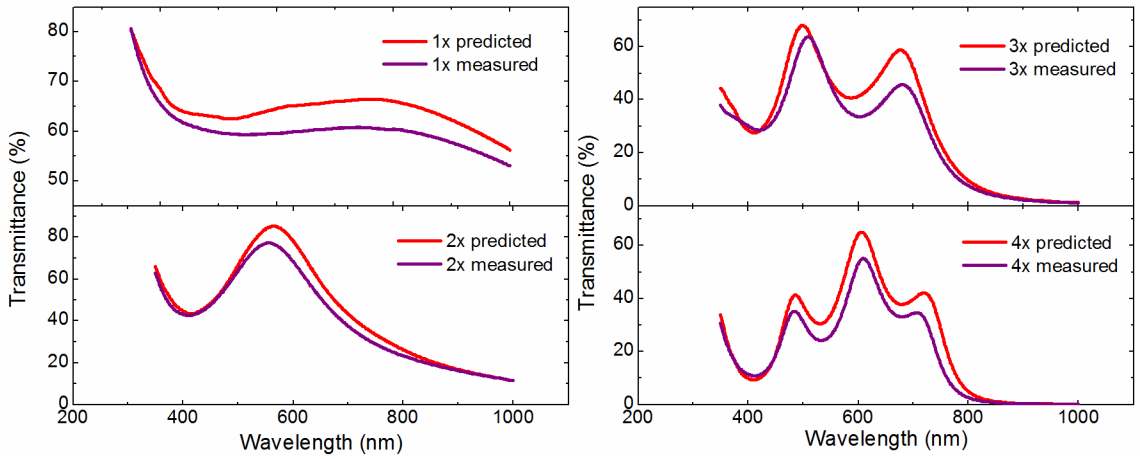

Figure 3.11 Predicted and measured transmittance for substructures of the AP MDPBG

The transmission of the full fabricated **AP** structure is shown in Fig. 3.11. This structure shows transmission of 53% ± 3% transmission with a 150 nm bandwidth between 475 nm and 625 nm. The transmission measurement, extended out to 5 μm through the use of a Shimadzu IR Prestige Fourier Transform Infrared (FTIR) spectrophotometer, shows that the structure displays excellent rejection of IR wavelengths beyond 800 nm. The measured transmission drops below 10^{-4} between 1 μm and 5 μm, giving excellent out of band rejection through the infrared, where the MDPBG behaves like bulk Ag.

Figure 3.12 shows the measured transmission spectrum of structure **AP** at varying angles of incidence. As the angle of incidence is increased the passband shifts toward shorter wavelengths due to the negative permittivity of the metal [94]. It can be seen that the measured magnitude of the angular dependence matches well with the predicted values. Transmission in structure **AP** changes by less than 5% over almost the entire range of the filter, giving a field-of-view that is more than 60 degrees wide.

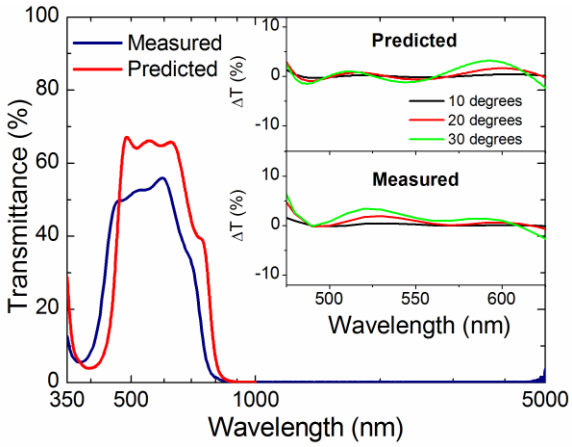

Figure 3.12 (a) Predicted and measured transmission of AP MDPBG. (inset) Predicted and measured change in transmission at 10, 20, and 30 degree angles of incidence for AP MDPBG

Finally, Fig. 3.13 shows the environmental stability of the fabricated structure. Figure 3.13a shows the transmission of an **AP** structure immediately after fabrication compared to the transmission after having been exposed to air for ten months. The transmission changes less than

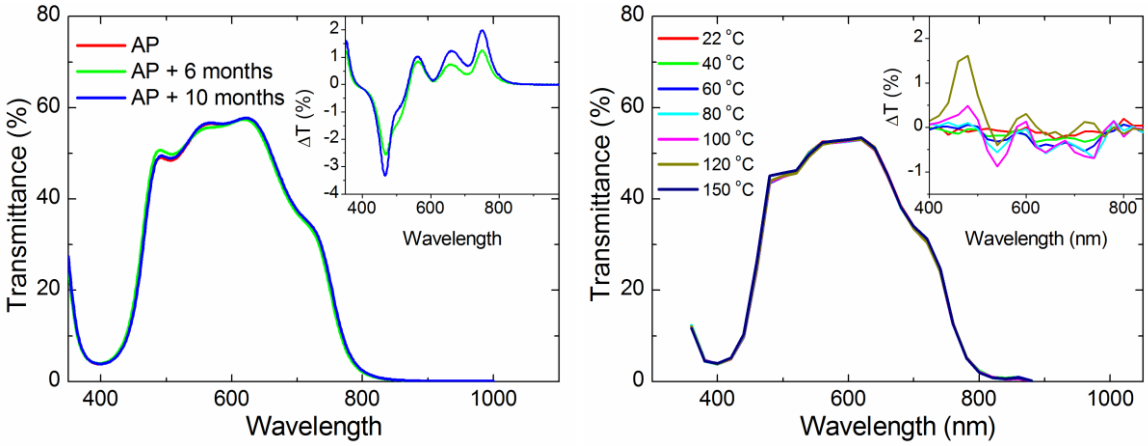

(a) (b)

Figure 3.13 (a) Transmission of AP MDPBG measured over ten months of exposure to air. (b) Transmission of AP MDPBG measured over temperatures up to 150° C

4%, demonstrating that the Al_2O_3 acts as an effective barrier to the diffusion of oxygen into the metal. Figure 3.13b shows the transmission of the structure at temperatures ranging from room temperature up to 150° C. In this case, the transmission changes by less than 2%.

3.5 Conclusion

We have described and discussed some of the effects that using low-refractive index dielectric materials in MDPBG structures have on their optical properties. We demonstrated that the inherent high index contrast in these structures makes is possible to tailor the spectral characteristics of the passband window by moving away from structures with thickness distributions that are strictly periodic. To illustrate this approach we designed and fabricated, by electron beam deposition, an aperiodic MDPBG using Ag and Al_2O_3, and compared its transmission and angular dependence to the predicted values, validating the design and demonstrating that such structures can be fabricated. The optical properties of the fabricated devices show little signs of degradation over a ten month period of time and are thermally stable at temperatures up to 150° C. The strong increase in the reflection losses, as opposed to absorption losses, when low-refractive index dielectrics were used, suggests that there may be design routes for further optimization of the overall transmission of MDPBGs.

Chapter 4. Nonlinear optical properties of induced transmission filters

4.1 Introduction

The metal-dielectric photonic band-gap (MDPBG) structures described in the previous present interesting opportunities for NLO applications because they are able to achieve high transmittance and low reflectance through a significant thickness of metal. However, the fact that they contain more than one Ag layer, and that each layer would contribute separately to the NLO response of the structure, makes them more challenging to analyze in this context. For this reason we turn our attention in the current to induced transmission filters (ITFs), which were described in section 1.5. Two example ITF structures are shown in Fig. 4.1. For the purposes of the present discussion, an ITF is defined as a multilayer structure that contains a single metal film surrounded by a dielectric structure that reduces reflectance and enhances transmittance at a particular wavelength. Because it contains only a single layer of metal, the NLO response is simpler to analyze and predict than for MDPBGs. As such, the study of ITFs also lays a foundation for understanding the NLO response of MDPBGs. The NLO properties of ITFs are interesting in their own right as narrow band nonlinear absorbers as well, and the presence of a single layer of Ag should not be viewed as a handicap in producing substantial enhancements of NLO behavior, as will be seen in this study.

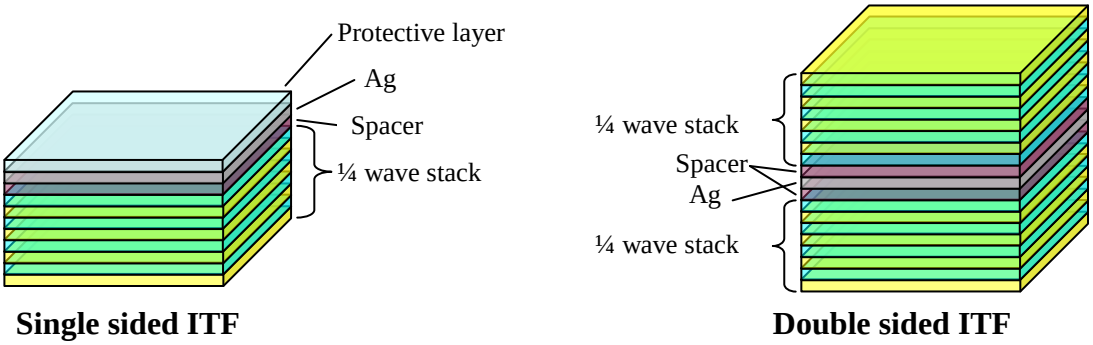

Figure 4.1 Schematics of single and double sided ITFs

We begin in section 4.2 by experimentally demonstrating the NLO responses of two ITFs in comparison with a single, isolated film of Ag, where the magnitude of the NLO response of the ITF is shown to be significantly larger than that of the standalone film. In section 4.3, we describe general design principles that affect the linear transmittance properties of ITFs, supported by a series of simulations of structures using the transfer matrix method. In section 4.4, we show how these design principles affect the NLO response of an ITF, and derive some conclusions on how to maximize the total NLO response.

4.2 Experimental procedure

4.2.1 Fabrication

The ITFs were fabricated using Ta_2O_5 as the high index material, SiO_2 as the low index material, and Ag as the metal. The fabrication processes, including the use of Ti adhesion layers, were the same as those described in section 2.2.1, with the additional note that the structure was removed from the vacuum chamber and annealed at 200 °C for one hour after every layer of Ta_2O_5. This was done to restore the proper ratio of Ta:O in the layer, because the process of e-beam deposition causes a small degree of dissociation of the Ta_2O_5 molecules. The annealing process

restores the lost oxygen, resulting in a film with a refractive index that is more consistent from run to run and is slightly higher than in non-annealed films.

4.2.2 Linear and nonlinear optical characterization

The refractive indices of the dielectric materials were determined from thin films deposited on Si wafers using spectroscopic ellipsometry as described in section 2.5.1. The methods used for measuring transmittance and reflectance were the same as those described in section 2.5.2 and the nonlinear characterization was the same as in section 2.5.3, except that the pump wavelength was 600 nm and the pump beam radius was assumed to be 247 μm (1/e radius).

4.2.3 Simulation of linear optical properties

The linear optical properties of the structures presented in this were simulated using the transfer matrix method as described in section 2.3.1, in which the complex permittivity of the Ag layer is represented according to the Drude model with parameters taken from the 20 nm thick Ag film in section 2.6.2:

$$\varepsilon = \varepsilon_\infty - \frac{\omega_p^2}{\omega^2 + i\omega\left(\gamma_1 + \beta\omega^2\right)}, \tag{4.1}$$

where ε_∞ = 4.0, ω_p = 1.38×10^{16} s^{-1}, γ_1 = 2.73×10^{13} s^{-1}, and β = 5.9×10^{-18} s^{-1}. Because these numbers were taken from a thinner film than is present in the ITFs, and because the permittivity of Ag is thickness dependent, these numbers do not necessarily reflect the actual permittivity of the present films. However, it serves as a good estimate.

4.2.4 Simulation of nonlinear optical properties

The NLO properties were simulated from the linear optical properties as follows. First, the temperature dependence of the Drude parameters was extracted from the WLC pump-probe measurements of the 30 nm thick Ag film in a manner similar to what was described in section 2.6.3, albeit with certain simplifying assumptions. Since the present study focuses only on the moment of maximum NLO response, which occurs before any energy is transferred from the electron cloud to the lattice, the lattice temperature is assumed to be constant at 300 °C. Thus, the temperature dependence of ω_p can be neglected, and only the electron temperature dependences of ε_∞ and γ_1 need to be considered. The resulting temperature dependences are:

$$\varepsilon_\infty = 4 + 4.4\times10^{-8}\left(0.7 + 3\times10^{-32}\omega^2\right)T_e^2, \tag{4.2}$$

$$\gamma_1 = 7.97\times10^{13} + 2.9\times10^{6}T_e^2. \tag{4.3}$$

The fits to the complex permittivity are shown in Fig. 4.3b below. In order to model the NLO responses of the ITFs, it was assumed that all of the energy that was neither transmitted nor reflected by the structure was absorbed by the Ag layer and converted to heat in the electron cloud. The electron temperature was them calculated as:

$$C_e\left(T_e\right)\frac{dT_e}{dt} = P(t), \tag{4.4}$$

where *P(t)* is the absorbed power as a function of time and

$$C_e(T_e) = 65T_e \tag{4.5}$$

is the temperature dependent specific heat of Ag. Integrating Eq. (4.4) and solving for the final value of T_e (assuming an initial T_e = 300) gives

$$T_e = \sqrt{\frac{2E_e}{65} + 300^2}\,, \tag{4.6}$$

where $E_e = \int P_e(t)$ is the total thermal energy absorbed by the electron cloud.

The measured temperature dependence of the Drude model parameters was then used to recalculate the complex permittivity of Ag at the point in time when all of the pulse energy has been absorbed by the electron cloud, before it is transferred to the lattice. The transmittance, reflectance, and absorbance of the structure were then calculated using the modified complex permittivity of Ag, and the changes in transmittance and reflectance were extracted.

4.3 Experimental results and simulation

4.3.1 Experimental results

In order to demonstrate the NLO response of an ITF we fabricated two ITFs with the structure

$$G\ (HL)_x\ S\ Ag\ P, \tag{4.7}$$

where *G* represents the glass substrate; *H* and *L* represent a ¼ wave layer of the high index and low index materials, in this case Ta_2O_5 and SiO_2, respectively; *S* represents a spacer layer of 75

nm SiO_2; *Ag* represents a 30 nm layer of Ag; and *P* represents a 410 nm protective coating of SiO_2. The parameter *x* defines the number of periods in the ¼ wave stack; for ITF 1, $x = 5$, and for ITF 2, $x = 4$. This is the only difference between the structures. The structures were designed to have center wavelengths at 600 nm, so using the measured refractive index values of 2.03 for Ta_2O_5 and 1.46 for SiO_2, the ¼ wave thicknesses were 74 and 103 nm, respectively. The thickness of the protective layer was chosen to be equal to a full wavelength so that it does not affect the transmittance at the peak wavelength.

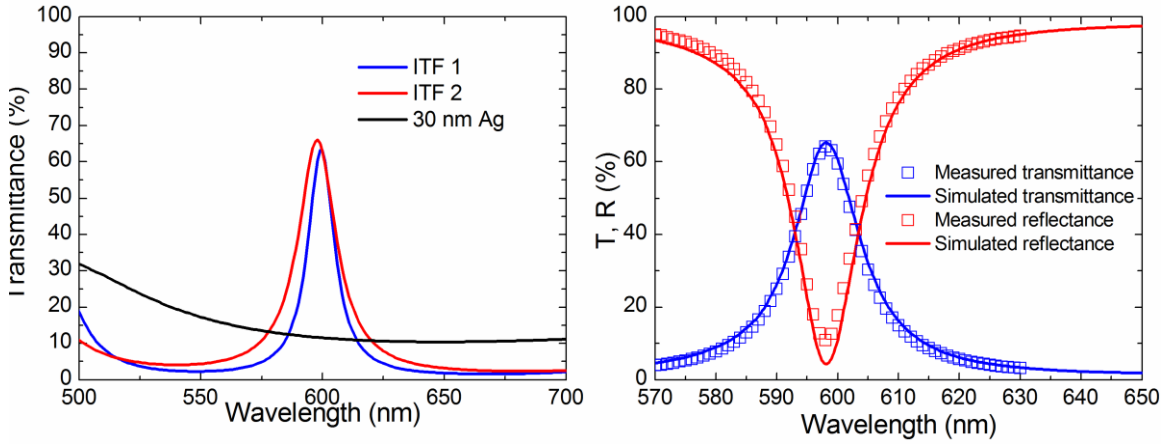

(a) (b)

Figure 4.2 (a) Measured transmittance of fabricated structures (b) Measured and simulated transmittance and reflectance of ITF 1

Figure 4.2a shows the measured linear transmittance of all three structures, and Fig. 4.2b shows the measured transmittance and reflectance of ITF 1 compared with simulations. It can be seen that the ITF greatly enhances the transmittance of the Ag film over a narrow bandwidth. The peak wavelengths of the two ITFs were measured to be at 598 nm, which is in good agreement with the design.

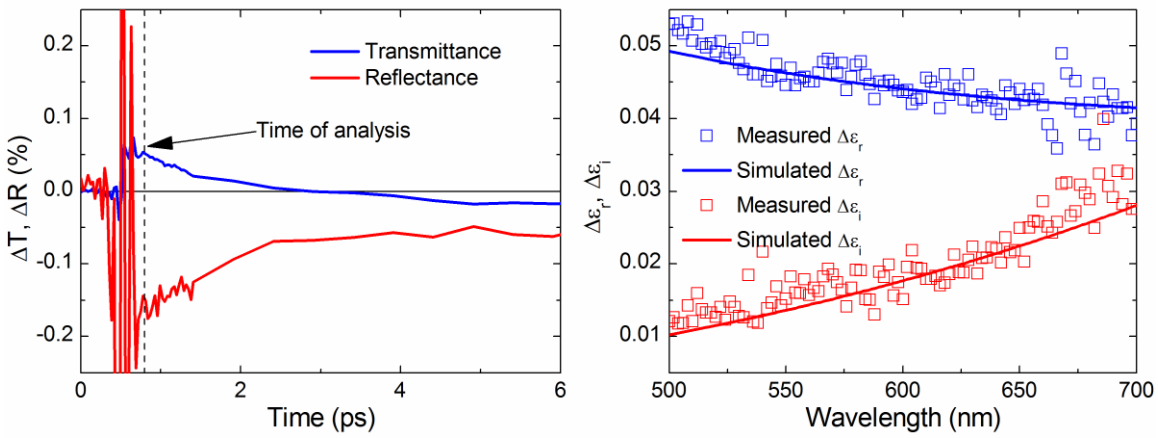

(a) (b)

Figure 4.3 (a) Measured change in transmittance and reflectance over time of a 30 nm Ag film at 600 nm with a pump fluence of 32 J/m^2. (b) Measured and simulated change in complex permittivity of Ag at 0.8 ps time delay

The change in NLO response with time of the 30 nm Ag film is shown in Fig. 4.3a, with a pump fluence of 32 J/m^2 and a probe wavelength of 600 nm. The first 0.7 ps is dominated by the instantaneous nonlinear contribution of the glass substrate. The remaining time shows the initial strong response of the metal that can be attributed to an increase in the electron temperature, followed by a decay as the electrons cool down and the lattice heats up, as has been observed many times previously [45-51]. For the present study we are interested only in the initial strong response, particularly the moment after the substrate contribution has passed but before the electrons begin to cool down. To this end, all of the analysis in this section is performed at time *t* = 0.8 ps, as shown in the graph.

Figure 4.4 shows the changes in transmittance and reflectance of the two ITFs due to a 32 J/m^2 pulse compared to the response of the Ag film. The magnitude of the responses of the two ITFs is significantly stronger than that of the film, even at the peak wavelength of 598 nm. Also, the

large peak and valley shape of the NLO response indicates that a red shift occurs in the transmittance peak of the ITF.

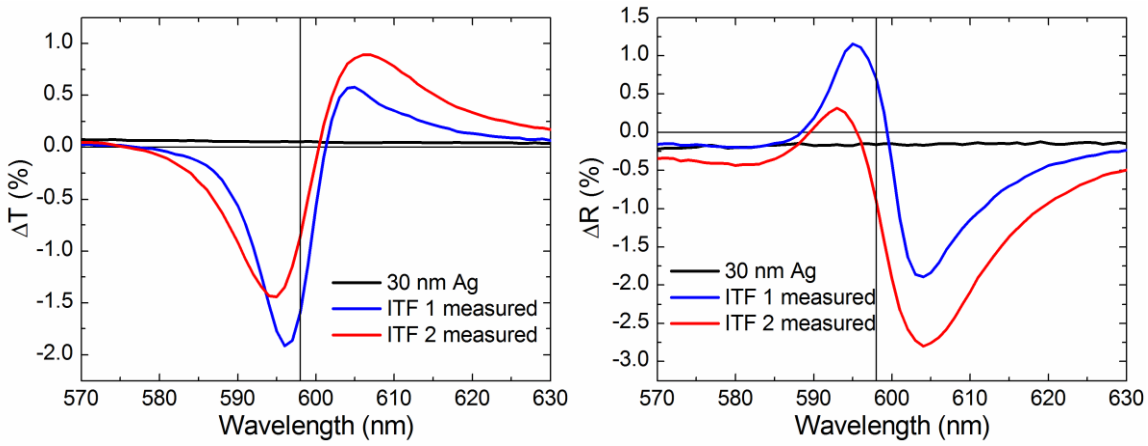

(a) (b)

Figure 4.4 Measured changes in transmittance and reflectance of 30 nm thick Ag film and ITFs 1 and 2 at t = 0.8 ps due to 32 J/m^2 pump pulse at 600 nm

The signs of each response are worth noting. As with the 20 nm thick Ag films studied in 2, it is expected that the absorbance of the 30 nm thick Ag film should increase as the film heats up. It would seem to follow naturally that this should lead to a decrease in transmittance; however, this is not the case. Instead, there is a large decrease in reflectance that more than compensates for the change in absorbance and leads to an increase in transmittance. The situation is different in the two ITFs at the peak wavelength. In both cases the magnitude of the increase in absorbance is larger than the change in reflectance, so there is a decrease in transmittance. ITF 1, in fact, shows an increase in reflectance, which leads to an even greater decrease in transmittance. The reason for this increase in reflectance, and other attributes of the nonlinear response, is explored in greater detail in section 4.4.2 below.

4.3.2 Simulation of fabricated ITFs

Figure 4.5 shows the simulations of ITF 1 and 2 compared with the measured data.

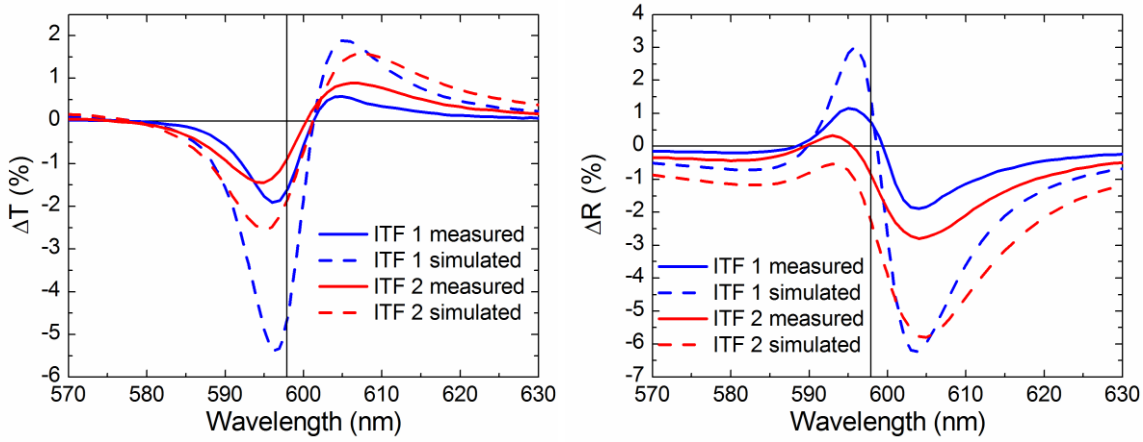

(a) (b)

Figure 4.5 Measured and simulated transmittance and reflectance of ITFs 1 and 2 at t = 0.8 ps due to 32 J/m^2 pump pulse at 600 nm

The magnitude of the NLO response deviates significantly between the measurements and the simulation, though the essential behavior is the same. The increase in reflectance at the peak wavelength in ITF 1 is predicted, as is the decrease in reflectance of ITF 2.

The difference in magnitude of the response could be for several reasons. The most likely is that the pump wavelength is not perfectly aligned with the peak of the ITF. A deviation of only a few nanometers can cut the response in half or more because the amount of energy absorbed by the Ag falls off rapidly with transmittance. Approximations made in deriving Eqs. 4.2 and 4.3 also likely contribute. Regardless, the simulations are in good qualitative agreement with the experiments.

4.4 ITF design and optimization

4.4.1 Design for linear optical properties

There are several different ways of conceptualizing the ITF. The first way, looking at a double sided ITF, is to consider the dielectric structures as antireflection coatings matched to the reflectivity of each Ag surface [64, 65]. The Ag film itself is a highly reflective, but only moderately absorptive, film; if the reflections can be eliminated then a fraction of the incident light will be absorbed but the majority will be transmitted. The second way, looking at a single sided ITF, to consider an ITF as a metamaterial with an interface between an ε-negative material (Ag) and an effective μ-negative material (dielectric structure). It has been shown [103] that such a structure shows improved transmittance and significant field enhancement at the target wavelength, leading to the amplification of NLO properties.

The third way to consider an ITF (again focusing on single sided ITFs), and the way that will be used here for design and analysis, is as a Fabry-Perot cavity where the Ag film is one mirror, albeit somewhat lossy, and the ¼ wave stack is the other. The remaining thickness of dielectric is the cavity spacer. In an ideal Fabry-Perot, where the total reflection at the peak wavelength is zero, two conditions must be met. First, the reflectances of the two mirrors must be equal; second, the round-trip phase within the cavity must be a multiple of 2π. If an ITF is to be an ideal Fabry-Perot, then, the number of periods and the refractive indices of the ¼ wave stack will be chosen such that the reflectivity is equal to that of the Ag film (alternatively, the thickness of the Ag film can be chosen to match the reflectivity of the dielectric structure). Also, since the reflection of the Ag film has non-zero phase shift, the thickness of the spacer will be chosen to

compensate. In this way, the ITF can be designed to have zero, or near zero, reflectivity at the peak wavelength.

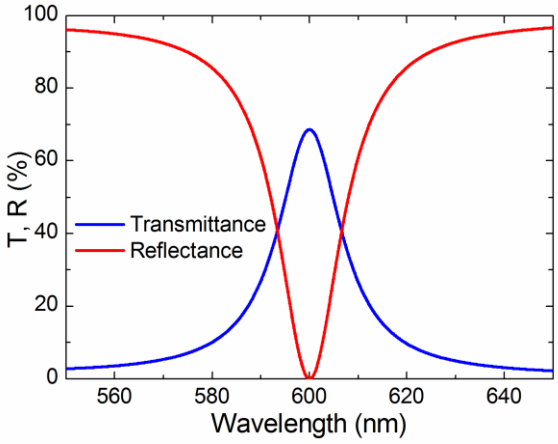

Figure 4.6 Transmittance and reflectance of perfectly matched ITF

Figure 4.6 shows the transmittance and reflectance of an ITF that is designed to be an ideal Fabry-Perot cavity with a center wavelength of 600 nm. For the sake of this and all following simulations, it is assumed that there is no substrate; that is, the ITF is surrounded by air on both sides, so reflections off the back side of the substrate can be ignored; thus, the structure is

$$\text{Air } (\text{HL})_x \text{ S Ag Air.} \tag{4.8}$$

For this structure, which is called a perfectly matched structure because the reflectance of the ¼ wave stack is designed to match the reflectance of the Ag, $n_l = 1.5$, $n_h = 2.109$, $S = 73.65$ nm, and Ag = 300 nm. As can be seen, the reflectance of this structure goes to zero at 600 nm. At this wavelength the reflectances of the Ag structure and the ¼ wave stack are 83.94% and 83.97%, respectively. The phase shifts of the reflections off the Ag and the ¼ wave stack are 2.314

radians and 0 radians, respectively, and the phase shift through the spacer is -1.157 radians, giving a net round trip phase shift of 0 radians.

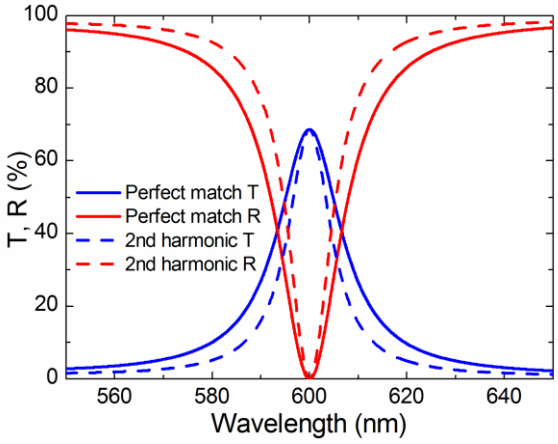

Figure 4.7 Transmittance and reflectance of 2nd harmonic ITF compared to perfectly matched ITF

Similarly, as shown in Fig. 4.7, the same matching conditions can be met by adding ½ wavelength to the spacer thickness with the obvious result that the finesse increases. This structure is called the 2nd harmonic ITF because it has the second shortest possible period.

The next parameter that we considered for variation was the degree of matching between the reflectance of the Ag compared to the reflectance of the ¼ wave stack. For this discussion, if the ¼ wave stack has lower reflectance then it is considered an under-matched structure; otherwise, it is an over-matched structure. The matching is changed by adjusting n_h, which affects the reflectance of the ¼ wave stack. Figure 4.8 shows the transmittance and reflectance of structures with n_h varying from 1.9 to 2.3.

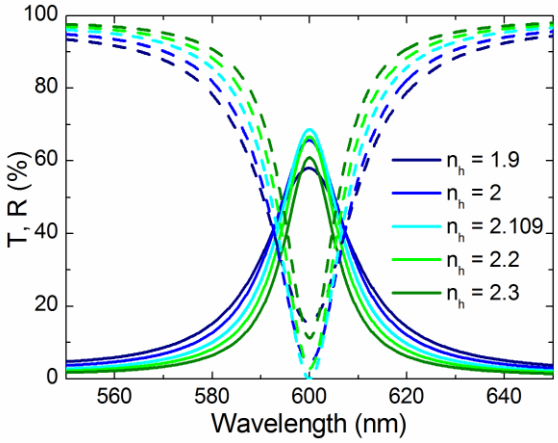

Figure 4.8 Transmittance and reflectance of variously matched structures with n_h ranging from 1.9 to 2.3

For both under-matched and over-matched structures, the reflectance at the peak ceases to be zero and there is a slight drop in peak transmittance. Over-matched structures have higher finesse than under-matched structures because the reflectance within the cavity is greater.

We next consider the impact of varying the thickness of the spacer layer. Figure 4.9 shows the transmittance and reflectance of structures with layers ranging between 0 nm (no spacer) and 150 nm.

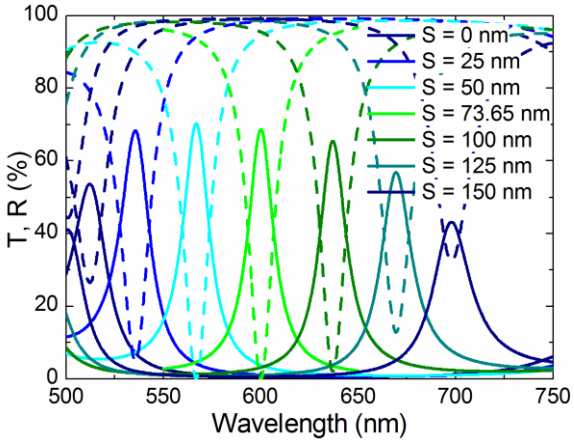

Figure 4.9 Transmittance and reflectance of phase shifted structures with spacer thicknesses ranging from 0 nm to 150 nm

These structures are called phase shifted structures. The location of the transmittance peak tracks closely with the wavelength at which the round trip phase shift within the cavity is zero, as shown in Fig. 4.10a. The strengths of the transmittance and reflectance at the peak are functions of how well the reflectances of the ¼ wave stack and the Ag film match. These reflectances are shown in Fig. 4.10b. As can be seen, the structures with peak wavelength below 575 nm and above 600 nm are under-matched.

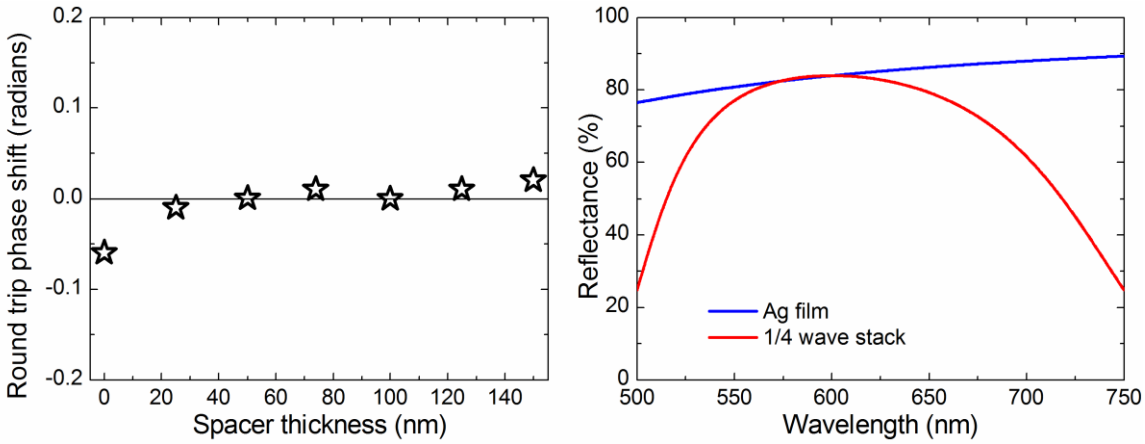

Figure 4.10 (a) Round trip phase shift of phase shifted ITFs at transmittance peak. (b) Reflectances of Ag film and ¼ wave stack

The next two structures under consideration are perfectly matched structures in which the matching condition is fulfilled at a wavelength other than the center wavelength of the ¼ wave stack. These structures are generated as follows. First, the reflectance of the ¼ wave stack is enhanced by adding two additional periods. The resulting reflectance is shown in Fig. 4.11a. As can be seen, the matching condition is fulfilled at 535.7 and 668.6 nm. The thickness of the spacer is then set so that the center wavelength aligns with these two matching points. The resulting thicknesses are 19.1 and 129.1 nm for the two structures. The transmittance and

reflectance of each is shown in Fig. 4.11b. Because the matching condition is met in both of these structures, the reflectance at the peak goes to zero.

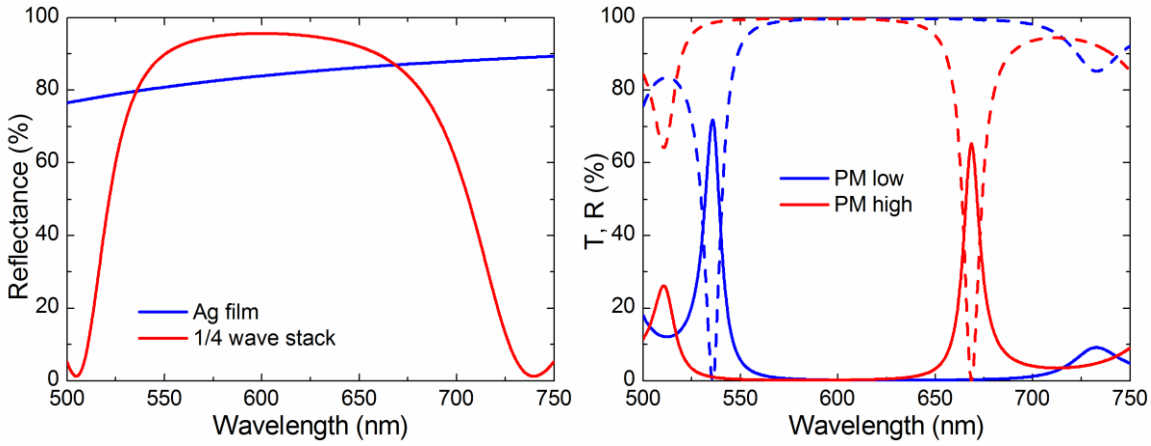

(a) (b)

Figure 4.11 (a) Reflectance of Ag film and ¼ wave stack with two additional periods. (b) Transmittance and reflectance of two shifted perfectly matched structures

The final two structures bridge the gap between single sided ITFs and double sided ITFs. They are both perfectly matched structures, designed to have transmittance similar to that of the original perfectly matched structure, though one has a 15 nm thick Ag film and the other has a 52.5 nm thick Ag film. The transmittance and reflectance of each is modified by adding a second dielectric structure on the top side of the Ag film. Figure 4.12 shows the transmittance and reflectance of these two structures compared with the original perfectly matched structure.

These two structures have the form

$$\text{Air } (HL)_x \, S_1 \, \text{Ag} \, S_2 \, (LH)_y \, \text{Air}, \tag{4.9}$$

where $x = 4$ and $y = 2$ for both structures. For the first structure, S_1 = 69.74 nm, Ag = 15 nm, and S_2 = -45 nm; the negative value on S_2 simply indicates that the last layer of the low index material is thinned down by 45 nm. For the second structure, S_1 = 76.43 nm, Ag = 52.5 nm, and S_2 = 173.5 nm. These two structures demonstrate the flexibility of a double sided ITF: simply by adjusting the thickness of S_2, it is possible to get nearly identical transmittance from structures with Ag thicknesses that differ by a factor of 3.5. The only other difference is a minor change in the thickness of S_1.

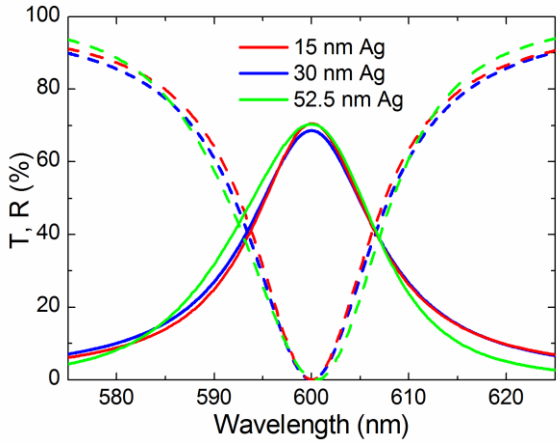

Figure 4.12 Transmittance and reflectance of structures with different Ag film thicknesses

For the double sided ITF, the ITF can be treated as a Fabry-Perot by considering the bottom ¼ wave stack as one mirror and the Ag layer plus the top dielectric structure as the other mirror. In other words, the top dielectric structure exists to modify the reflectance of the Ag layer. For the structure with the 15 nm thick Ag film, the top dielectric structure serves to enhance the reflectance of the Ag; for the structure with the 52.5 nm thick Ag film, the structure inhibits the reflectance. The end result is that both have the same reflectance as the unmodified 30 nm thick Ag film. Thus, all three structures have very similar transmittance and reflectance in spite of the large differences in Ag thickness.

The properties of each of the structures in this section result directly from basic theory of Fabry-Perot structures. They are presented here as illustrations of what is possible to achieve in terms of linear transmittance and reflectance with an ITF. More importantly, though, they provide a foundation to demonstrate the NLO properties of ITFs, and they will be used in the next section to reveal the various processes that contribute to this NLO response.

4.4.2 Design for nonlinear optical properties

In this section each of the designs from the previous section are simulated using the process described in section 2.3.2 to demonstrate their NLO responses. From these responses we can separate the individual processes that contribute to the NLO behaviors of ITFs and begin to formulate methods by which this NLO response can be maximized. The object of this study is to maximize the change in transmittance at the peak wavelength. It will be seen from these simulations that the essential nature of the NLO response is a function only of whether the structure is under- or over-matched, and the strength of the response is a function only of the thickness of the metal and the magnitude of the linear absorbance.

As discussed in section 1.3, it is impossible and undesirable to eliminate absorbance from structures that are designed to take advantage of the NLO response of metal. To this end, each of the structures in the preceding section (with the exception of the more extreme phase shifted structures) is designed to have approximately 70% transmittance and little to no reflectance.

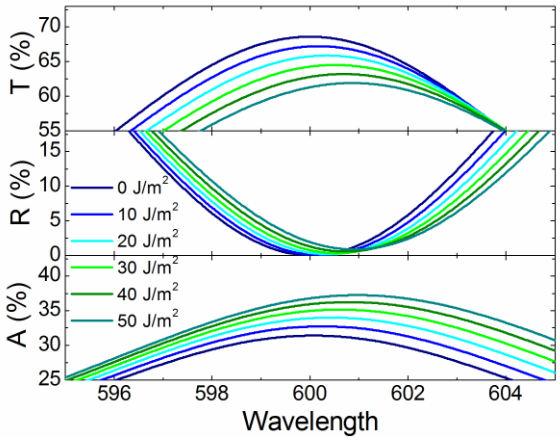

Figure 4.13 Transmittance, reflectance, and absorbance of perfectly matched structure under illumination by pump pulses with fluences ranging from 0 to 50 J/m^2 at 600 nm

We begin by considering the response of the perfectly matched structure to a pump pulse with fluences up to 50 J/m^2. Figure 4.13 shows the changes in transmittance, reflectance, and absorbance for this structure.

Two features can be observed from these measurements. First, a red shift can be observed in the transmittance peak. The red shift is a function of the change in phase of the reflection off the Ag film. The peak wavelength is located at the point where the round trip phase shift within the cavity is zero; that is,

$$\Phi_{Ag} + \Phi_D + 2 \times \Phi_S = 0, \tag{4.10}$$

where Φ_{Ag} is the phase shift of the reflection off the Ag film, Φ_D is the phase shift of the reflection off the dielectric mirror, and Φ_S is the phase shift within the spacer. As the phase shift in the Ag film changes, the peak wavelength shifts to maintain zero round trip phase. The shift in the peak wavelength, $d\lambda$, can be calculated using the equation

$$dT_e^2 \frac{\partial \Phi_{Ag}}{\partial T_e^2} + d\lambda \left(\frac{\partial \Phi_{Ag}}{\partial \lambda} + \frac{\partial \Phi_D}{\partial \lambda} + 2 \times \frac{\partial \Phi_S}{\partial \lambda} \right) = 0 . \tag{4.11}$$

The individual differential terms can be approximated in the neighborhood as:

$$\frac{\partial \Phi_D}{\partial \lambda} = 0.0167 \, \text{rad/nm} \tag{4.12}$$

$$\frac{\partial \Phi_{Ag}}{\partial \lambda} = 0.0015 \, \text{rad/nm} \tag{4.13}$$

$$\frac{\partial \Phi_{Ag}}{\partial T_e^2} = -10^{-9} \, \text{rad/K}^2 \tag{4.14}$$

$$\frac{\partial \Phi_S}{\partial \lambda} = 0.0020 \, \text{rad/nm} \tag{4.15}$$

Since the final electron temperature is approximately 4000 K, the peak wavelength shift is expected to be 0.8 nm; this is what is observed in Fig. 4.13.

The second feature that can be observed is the increase in absorbance. Because there is a relatively small change in reflectance at the peak wavelength, this increase in absorbance leads to a decrease in transmittance. These two effects, the nonlinear absorbance and the phase shift, combine to create the observed NLO response.

We next consider the NLO response of the 2nd harmonic ITF. Figure 4.14 shows the nonlinear transmittance, reflectance, and absorbance of this structure.

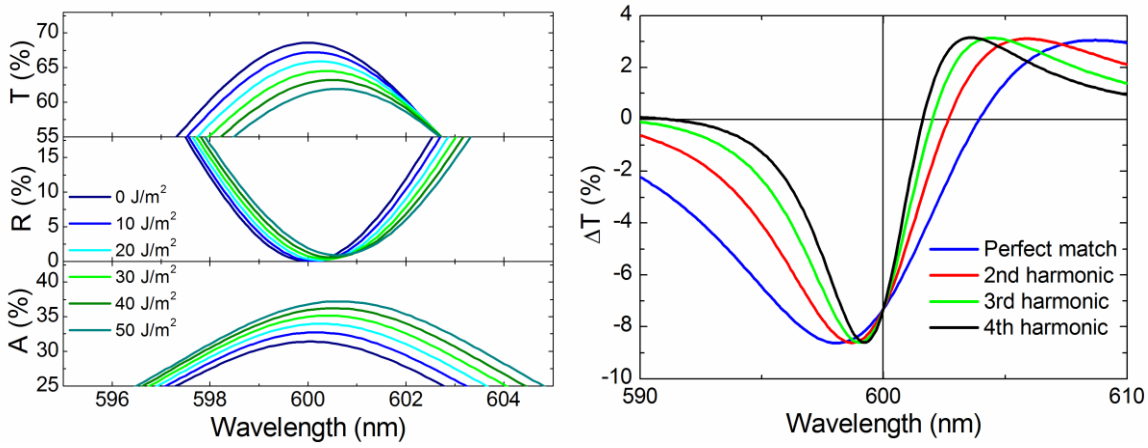

(a) (b)

Figure 4.14 (a) Transmittance, reflectance, and absorbance of 2nd harmonic structure under illumination by pump pulses with fluences ranging from 0 to 50 J/m^2 at 600 nm. (b) Change in transmittance for harmonic structures with 50 J/m^2 pump pulse

The wavelength dependence of the phase shift in the spacer increases to

$$\frac{\partial \Phi_S}{\partial \lambda} = 0.0072\ \text{rad/nm} \tag{4.16}$$

so that the peak wavelength shift drops to only 0.63 nm. However, because the finesse of the 2nd harmonic structure is greater than that of the perfectly matched structure, the net effect on the transmittance at 600 nm is the same. In fact, as can be seen from Fig. 4.14, the change in transmittance at the peak wavelength remains the same through at least the 4th harmonic.

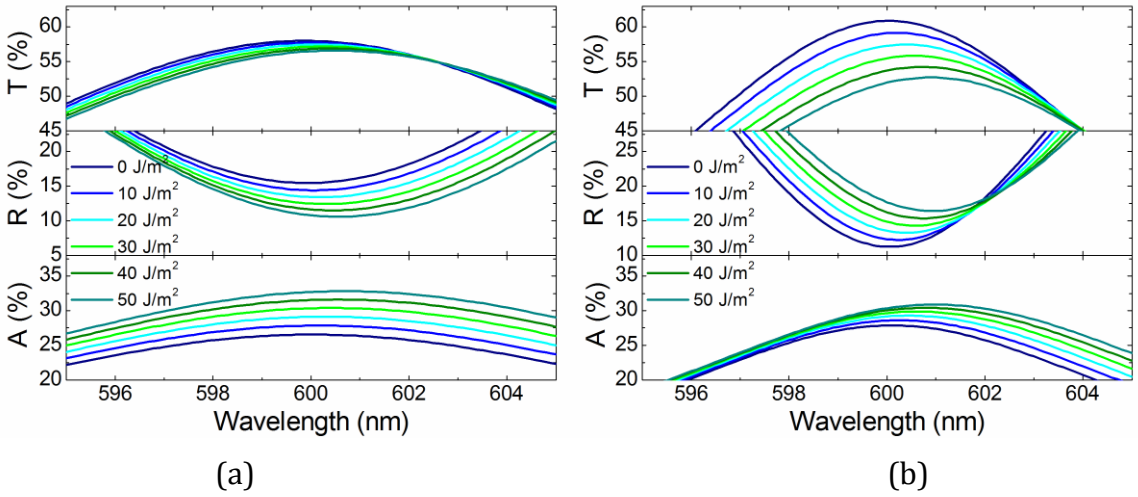

Figure 4.15 Transmittance, reflectance, and absorbance of (a) under-matched and (b) over-matched structures under illumination by pump pulses with fluences ranging from 0 to 50 J/m^2 at 600 nm

We next consider the under-matched and over-matched structures. Fig. 4.15 shows the evolution of the transmittance, reflectance, and absorbance of the structures with n_h = 1.9 and n_h = 2.3. The greatest difference between these two structures is the change in reflectance: for the under-matched structure, the reflectance drops; for the over-matched structure, the reflectance increases. The reason for this difference arises from the fact that the reflectance of the Ag film decreases as it heats up. The reflectance of the full structure is a function of how well the reflectance of the Ag film matches with that of the ¼ wave stack. For the under-matched structure, this matching improves as the reflectance of the Ag decreases and becomes more like that of the ¼ wave stack. For the over-matched structure, the matching condition gets worse and the reflectance of the structure increases.

The effects of this difference can be seen in the changes in transmittance as well. In the under-matched structure the change in reflectance nearly balances out the change in absorbance, so the

transmittance changes very little. In the over-matched structure the changes in reflectance reinforces the change in absorbance, so the transmittance drops considerably more.

The perfectly matched structure marks a midpoint between these two structures. Because the reflectance of the Ag matches that of the ¼ wave stack, the reflectance of the full structure changes little. It begins to increase eventually as the perfectly matched structure slowly becomes over-matched. In fact, an under-matched structure, if heated far enough, will become a perfectly matched structure and then an over-matched structure.

Figure 4.16 shows the changes in transmittance and reflectance for each of the variously matched structures from Fig. 4.8 above for a 50 J/m^2 pulse. The increase in change in transmittance for over-matched structures can be seen; though from these simulations it is apparent that there is a limit to how far this improvement can be taken. This limit arises because over-matching a structure comes at the cost of decreased linear transmittance and increased linear reflectance.

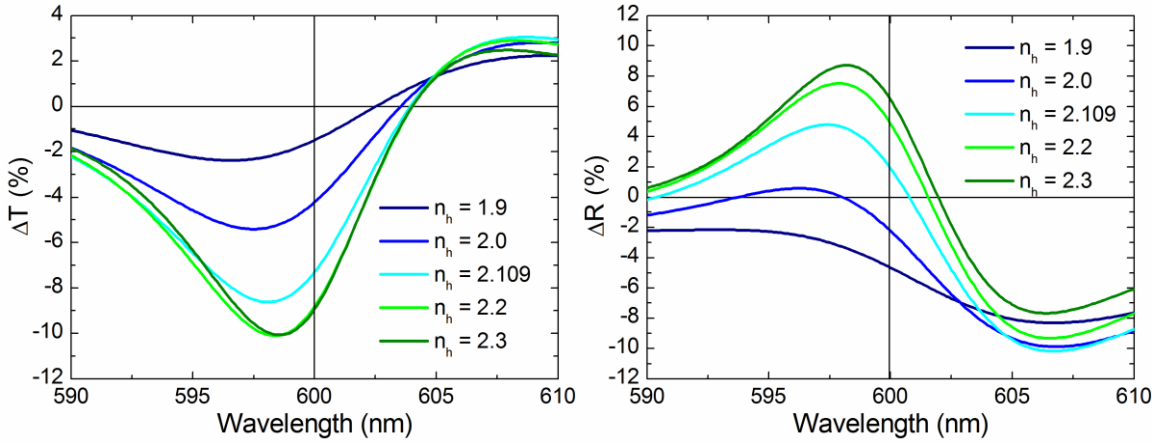

(a) (b)

Figure 4.16 Changes in transmittance and reflectance for variously matched structures with 50 J/m^2 pump pulse

Following the order of structures from the previous section, we come to the phase shifted structures. The changes in transmittance and reflectance are shown in Fig. 4.17, in which the center wavelength was shifted to line up at 600 nm. As can be seen from the change in reflectance, all the structures except the ones with S = 50 nm and S = 73.95 nm behave as under-matched structures. The structure with S = 73.95 nm is, of course, the perfectly matched structure. The structure with S = 50 nm is slightly under-matched, but as the Ag film heats up it passes through the point of perfect matching to become over-matched; hence the increase in reflectance at the peak wavelength. The drop in transmittance predictably grows weaker as S deviates from the perfect matching condition, and actually becomes an increase in transmittance when S = 0 nm. This trend is expected because the extreme structures are the most strongly under-matched.

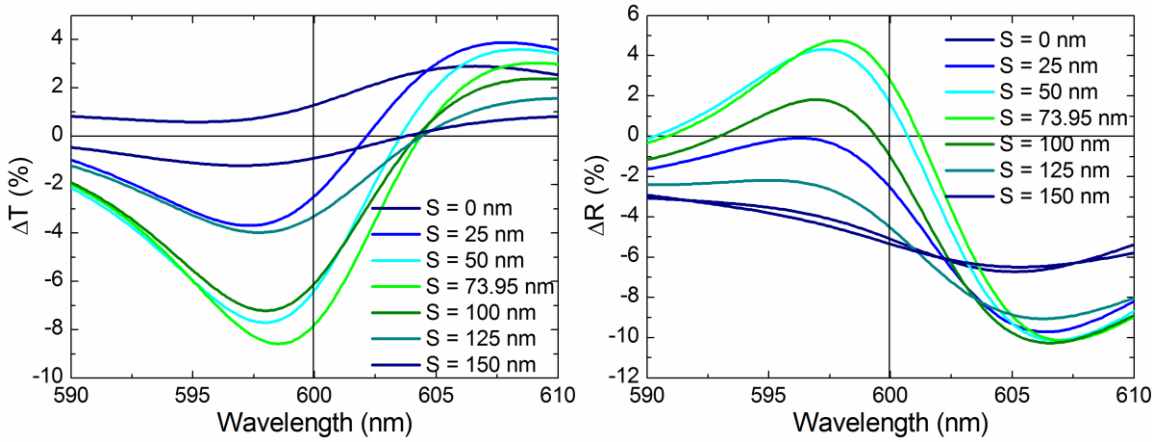

(a) (b)

Figure 4.17 Changes in transmittance and reflectance for phase shifted structures with 50 J/m^2 pump pulse; peak wavelength of each structure has been shifted to 600 nm

The next two structures under consideration are the alternate perfectly matched structures. The changes in transmittance and reflectance are shown in Fig. 4.18 compared to the perfectly

matched structure, where the peak wavelengths were all shifted to line up at 600 nm. The essential responses of all three structures are very similar. The minor difference in the magnitude of the change in transmittance at the peak wavelength is due to the fact that the peak transmittance is slightly lower in PM high and slightly higher in PM low. This means that the absorbance at the peak is slightly higher in PM high and slightly lower in PM low. Since the temperature change follows the absorbance, the response is strongest in PM high. The remaining differences in the responses of the three structures arise from the fact that the bandwidth is about 30% narrower in PM low and PM high compared to the perfectly matched structure.

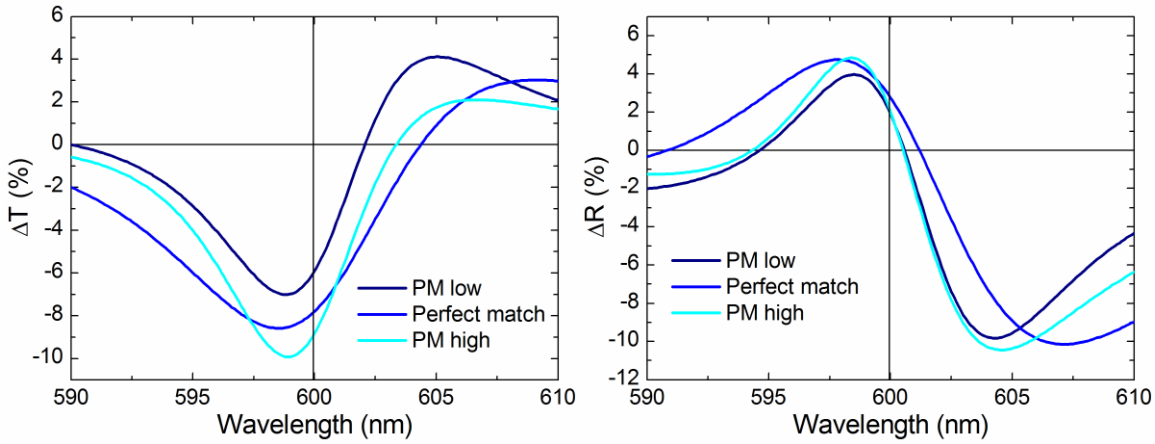

(a) (b)

Figure 4.18 Changes in transmittance and reflectance for alternate perfectly matched structures with 50 J/m^2 pump pulse; peak wavelength of each structure has been shifted to 600 nm

It can be concluded from the simulations to this point that the character of the response of an ITF, regardless of the exact structure, is a function simply of whether the structure is under-matched, perfectly matched, or over-matched.

The final set of structures measures the effects of changing the thickness of the Ag film. Figure 4.19 shows the changes in transmittance and reflectance of the double sided ITFs described at the end of the previous section compared with the perfectly matched structure.

As can be seen, the nonlinear transmittance and reflectance go opposite the thickness of the Ag film: the response of the 15 nm Ag film at the peak wavelength is 1.9 times the strength of the 30 nm Ag structure and 4.3 times the strength of the 52.5 nm Ag structure. Such a large difference in response is remarkable considering the fact that the transmittances of each structure are nearly identical. The difference arises from the fact that there is a significant variation in the change in temperature of the Ag film. All three structures absorb the same amount of energy, but this energy is much more concentrated in the structure with 15 nm Ag than it is in the other two. Thus, the Ag heats up more and produces a larger NLO change. This enhancement of the NLO response comes at the cost of structural complexity, though, since it is necessary to use a double sided structure to realize it.

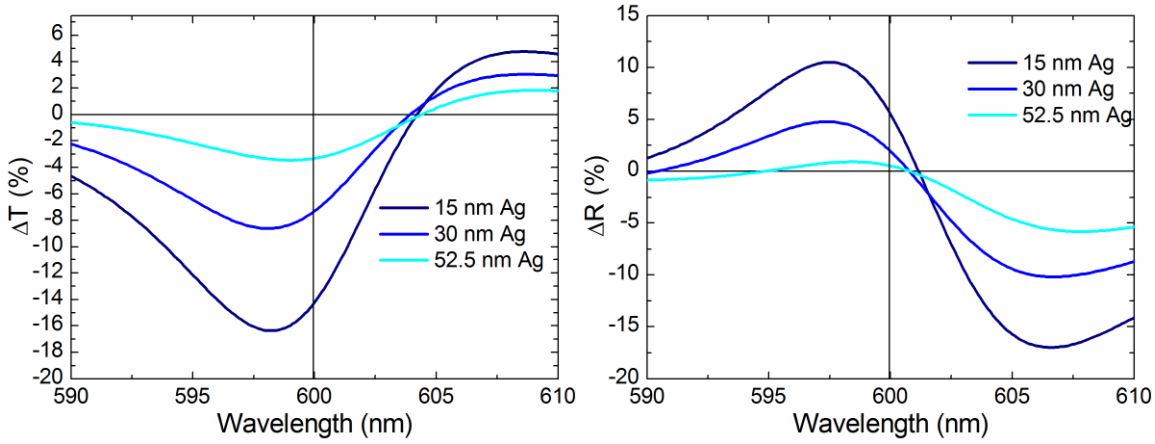

(a) (b)

Figure 4.19 Changes in transmittance and reflectance for structures with different thicknesses of Ag with 50 J/m^2 pump pulse

This analysis does not take into account the fact that the refractive index of Ag is dependent on the film thickness, as described in previous s. It may be that the increase in damping in the thinner films will mitigate the advantages of having a thinner film; this, though, is beyond the scope of the current research.

4.4.3 Maximizing nonlinear optical properties

In this section we design a structure that maximizes the change in transmittance of an ITF that has 70% transmittance at its peak. It is assumed that 15 nm is the minimum achievable thickness for Ag. The response is compared to the equivalent isolated Ag film.

Based on the results of the previous section, the NLO response can be maximized by using a structure with the minimum achievable thickness of metal and by slightly over-matching the structure. Figure 4.20 shows the changes in transmittance and reflectance of such a structure compared to the perfectly matched structure and to the structure with 15 nm Ag. This optimized structure was designed by taking the 15 nm Ag structure and increasing n_h in the lower ¼ wave stack (but not in the upper ¼ wave stack). It turns out that the best response is when n_h is within the range of 2.2 to 2.3; within this range it does not make a large difference what the exact value is. For this structure, $n_h = 2.2$.

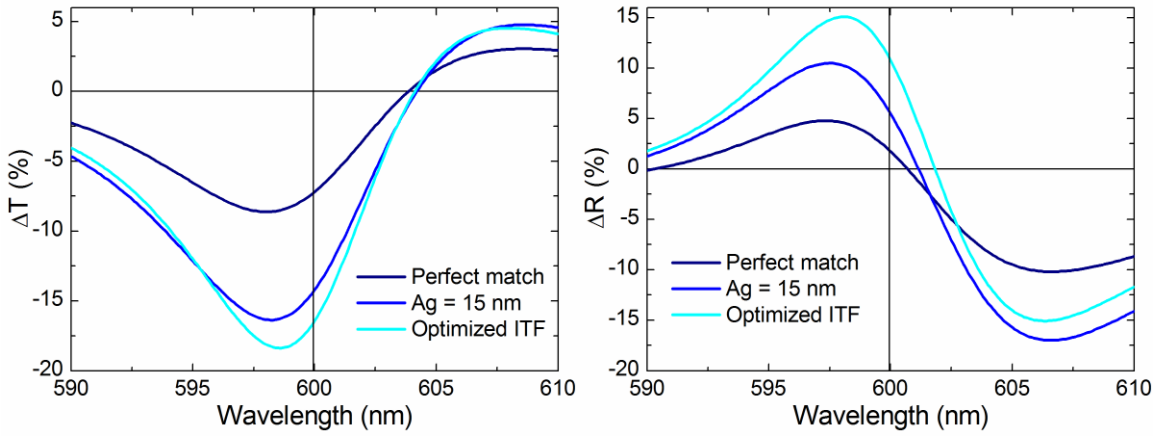

(a) (b)

Figure 4.20 Changes in transmittance and reflectance for optimized structure with 50 J/m^2 pump pulse, compared to perfectly matched structure and 15 nm Ag structure

At the peak wavelength, the change in transmittance in the optimized structure is larger than that of the perfectly matched structure by a factor of 2.3. Further enhancements could be made if the Ag films could be further thinned; however, the challenge of fabricating thinner layers must first be overcome.

4.5 Conclusion

We have explored the linear and nonlinear optical properties of ITFs. We fabricated two different ITF designs and measured both the linear and NLO properties. The NLO response was qualitatively in line with theory, though the magnitude was not as large as predicted. We also simulated a number of different designs of ITFs and discussed the effects each design variation has on the linear and NLO properties. The principles of under-matched, perfectly matched, and over-matched structures were discussed, and it was determined that this matching condition is the primary driver of the nature of the NLO response. The impacts of varying the thickness of the Ag film and adding a top dielectric structure were also investigated, and it was shown that the

magnitude of the response is primarily a function of this film thickness. Structures with thin Ag layers and compensating top dielectric structures were shown to produce significantly stronger responses. Based on these studies, an optimized ITF was simulated and shown to have a response 2.3 times that of the perfectly matched structure.

Chapter 5. Conclusions and future work

5.1 Conclusions

Thin metal films are interesting for both their linear and their NLO properties. They are interesting for their linear optical properties because the contrast in refractive index between metals and dielectrics is quite large. This causes larger reflections at metal/dielectric interfaces than can be achieved at dielectric/dielectric interfaces. These reflections make it possible to tailor the transmittance spectra of multilayer structures more easily and with fewer layers than is possible with purely dielectric structures. The primary limitation that such structures face is that the absorption in the metal layers limits how thick the structure can be.

Metals are interesting for their NLO properties as well because the NLO response of metal is orders of magnitude larger than can be found in dielectric materials. Again, the challenge that limits the usefulness of this NLO response is absorption in the metal.

It is necessary for taking advantage of both the linear and NLO properties to have efficient multilayer structures that make the greatest use possible of a very small amount of metal. A number of structures such as MDPBGs and ITFs have been proposed to accomplish this task. These structures make use of structural resonances to create transmission windows in spectral regions that would otherwise be opaque or nearly opaque.

The focus of this present work was to build a greater understanding of how these structures can be used for linear and NLO applications. To this end, the three research objectives covered in this work were:

1) Develop, through WLC pump-probe measurements and through simulation, a comprehensive model that describes the NLO response of a thin Ag film
2) Perform a systematic study of the linear optical properties of low index MDPBGs, including the development of an algorithm to optimize a structure for an arbitrary transmission spectrum
3) Simulate and experimentally demonstrate the NLO response of an ITF, including a study of sensitivity to design parameters.

5.1.1 NLO response of a thin Ag film

White light continuum pump-probe measurements were carried out on a 20 nm thick Ag film. The change in complex refractive index over time was calculated from these measurements. The refractive index was fit to the Drude model at each point in time. Changes to the individual Drude parameters were correlated to changes in the electron and lattice temperatures of the Ag film as follows:

$$\begin{aligned}\varepsilon_\infty\left(\omega, T_l(t), T_e(t)\right) = 3.94 + \left(-0.26 + 4.0\times10^{-16}\omega\right)\times \\ \left\{(1.5\pm1.0)\times10^{-4}T_1(t) + (4.5\pm0.5)\times10^{-8}T_e(t)\right\}\end{aligned} \tag{5.1a}$$

$$\omega_p\left(T_l(t)\right) = 1.374\times10^{16} + (1.6\pm0.4)\times10^{11}T_l(t) \tag{5.1b}$$

$$\begin{aligned}\gamma_1\left(T_l(t), T_e(t)\right) = 5.12\times10^{13} + (8.5\pm1.0)\times10^{10}T_l(t) \\ + (3.0\pm0.2)\times10^{6}T_e^2(t)\end{aligned}. \tag{5.1c}$$

The changes in electron and lattice temperatures over were in turn fit to a two temperature model:

$$65T_e \frac{dT_e}{dt} = -3.0\times10^{16}(T_e - T_l) + P(t), \tag{5.2a}$$

$$2.4\times10^{6} \frac{dT_l}{dt} = 3.0\times10^{16}(T_e - T_l) - 5.0\times10^{4}(T_l - T_e). \tag{5.2b}$$

These equations were found to fully describe the NLO response of the 20 nm thick Ag film for all pump fluences and wavelengths.

This model could be used to predict the NLO response of a multilayer structure containing such a film. It has one key limitation, however. Because the refractive index of a film of Ag is dependent on its thickness, the way in which the Drude model parameters change is dependent on thickness as well. Thus, this model will be different for thicker or thinner Ag films. Furthermore, surface morphology and deposition conditions can have different effects on the refractive index, hence the model parameters, as well.

Regardless of this shortcoming, the NLO response of any continuous Ag film should take on the basic form of the above equations with only small differences in the magnitudes of the parameters.

5.1.2 Linear optical properties of MDPBGs

The linear optical properties of MDPBGs based on Ag were explored using a series of simulations and validated using a fabricated structure.

The effects of particular design variations on the transmittance and reflectance of an MDPBG were explored. The design variations included changing the thickness and refractive index of the dielectric material, changing the thickness and refractive index of Ag, changing the number of periods, and changing the Ag thickness and number of periods simultaneously in order to maintain a constant total thickness of Ag. It was shown that these design variations resulted in various tradeoffs between bandwidth and transmittance. The combination that resulted in the highest transmittance and widest bandwidth, was having many periods in which the layers of Ag were as thin as possible.

An optimization routine was introduced that permitted the design of an MDPBG for a particular transmittance spectrum. The routine adjusted each layer of the structure individually in order to match the desired transmittance spectrum. The routine was used to design a structure with a nearly flat transmittance band with greater than 50% transmittance and 125 nm bandwidth in the visible spectrum.

The optimized structure was then fabricated, and the transmittance of the resulting device matched reasonably well with the predicted values. The fabricated structure was shown to be robust against high temperatures and long exposure to air. The transmittance did not change significantly when heated to 150 ^{o}C or when exposed to air for 10 months.

5.1.3 NLO properties of ITFs

Two ITFs were fabricated and the NLO properties were measured using WLC pump-probe spectroscopy. The NLO response was compared to an isolated film of Ag of the same thickness as the Ag film in the ITF. It was shown that the NLO response of one of the ITFs was more than 30 times stronger than the response of the Ag film. The responses of the ITFs were compared to simulation and it was shown that the measured responses qualitatively matched the simulated responses; the magnitudes were off by about a factor of two, which is likely due to experimental error.

A series of ITF designs was simulated to demonstrate the effects of some design parameters on the linear optical properties. The parameters that were varied were the reflectance of the ¼ wave stack, the thickness of the spacer layer, the thickness of the Ag layer, and various combinations thereof. It was shown that the peak wavelength was located at or very near the wavelength where the round trip phase shift within the structure is a multiple of 2π. The transmittance and reflectance of the ITF at the peak wavelength is a function of how well the reflectance of the ¼ wave stack and the Ag film matched each other. If the reflectances match perfectly then the structure has maximized transmittance and zero reflectance at the peak. Otherwise, the structure has non-zero reflectance and the transmittance drops accordingly. The structures can be divided into the categories of under-matched, over-matched, and perfectly matched based on if the ¼ wave stack reflectance was less than, greater than, or equal to the reflectance of the Ag film.

The NLO responses of each of the ITF designs were also simulated, and again the matching of the ¼ wave stack to the Ag determines the nature of the response. A distinction was made between over-matched and under-matched structures in the NLO properties. It was shown that

the over-matched structures produce a greater change in transmittance than under-matched structures because of the way in which the reflectance of the Ag layer changes. It was also shown that the NLO response can be greatly increased by using a thinner layer of Ag that has been augmented by a second ¼ wave stack on top. An optimal ITF was designed that was slightly over-matched and used a thin layer of Ag in order to maximize the change in transmittance at the peak wavelength. This structure was shown to have an NLO response 2.3 times greater than that of the equivalent perfectly matched ITF.

5.2 Future work

The work presented in this dissertation is far from an exhaustive study of the linear and nonlinear optical properties of metal-dielectric multilayer structures. There are several immediately obvious directions in which this work could be expanded, ranging from further fundamental studies of the NLO properties of metals through further optimization and application of the structures. A list of directions for future work includes:

- NLO response of Ag with varying film thickness and surface roughness
- Optimization of Au or Cu in linear MDPBGs
- Systematic study of nonlinearity in MDPBGs
- Use of Au or Cu in NLO ITFs
- Inclusion of nonlinear dielectrics in ITFs
- Use of genetic algorithm to optimize NLO metal-dielectric multilayer structures

5.2.1 NLO response of Ag

The first possible area of study focuses on how the NLO response of Ag changes with film thickness and film roughness, respectively. These studies would fill in a major foundational gap encountered in the work of this dissertation. Because the NLO response of Ag is particularly sensitive to the damping parameter γ in the Drude model, and because γ is sensitive to both film thickness and film roughness, the NLO results from 20 nm Ag films may not accurately predict the NLO results from structures that contain films of any other thickness.

The object of the study would be to come up with a relationship between γ and the temperature dependent parameters $\Delta\gamma/\Delta T_e$ and $\Delta\gamma/\Delta T_l$. A limited form of this relationship was presented in section 2.7.2; however there were discrepancies between the theory and the measured values that might be accounted for by surface scattering processes. Since surface scattering is a function of film thickness and surface roughness, it should be possible to isolate this contribution from a series of measurements such as the ones proposed here.

As a side note, if the probe wavelengths are extended further into the infrared it may be possible to reduce the error in the Drude model parameters—particularly the uncertainty of the interplay between ω_p and the dispersion in ε_∞.

5.2.2 Optimization of Au and Cu in linear MDPBGs

The highest transmittances in MDPBGs have been achieved with Ag as the metal. This is because the absorbance in Ag is less than that of Au or Cu. However, the NLO response of Au and Cu is stronger than that of Ag, so it would be worthwhile to do a systematic study of the

linear optical properties to determine how best to maximize the transmittance. It is expected that the conclusions from Ag will carry over to the other metals, though there will be additional complications arising from the presence of the interband transitions in the visible spectrum.

5.2.3 Systematic study of nonlinear MDPBGs

A systematic study of the NLO properties of MDPBGs would be, in many ways, the ultimate culmination of the present work. The goal of this study would be to determine how best to use an MDPBG as a broadband NLO structure. It would build on the lessons learned in this work, making use of the NLO model of metal, the optimization of linear MDPBGs, and the NLO studies of ITFs. The result would ideally be an understanding of how the design of an MDPBG affects its NLO response and how the design can be manipulated in order to achieve a particular desired response.

5.2.4 Use of Au or Cu in NLO ITFs

Ag was chosen for the studies in this dissertation because it has the simplest NLO response. However, because the NLO response of Au and Cu is greater, it would be very interesting to incorporate them into ITFs in place of Ag. All of the design rules determined from the Ag structures would carry over directly to Au and Cu. The presence of interband transitions in the visible spectrum for these two alternative metals could lead to a very interesting variety ITF behaviors. For instance, depending on the peak wavelength the phase shift could move in the opposite direction or the transmittance might increase instead of decrease. Simulations making use of existing models for interband NLO contributions could quickly point to interesting wavelengths and structure designs.

5.2.5 Inclusion of nonlinear dielectrics in ITFs

Within an ITF there are regions in the dielectric layers, particularly the spacer layer, in which there is a large enhancement of the electric field intensity. For this reason, it would be interesting to incorporate dielectrics that themselves have NLO properties into ITFs as a complementary NLO contribution to that of the metal.

5.2.6 Genetic algorithm optimization

The final area of interest for future work is in the use of the genetic algorithm for optimizing the linear and nonlinear properties of metal-dielectric multilayer structures. The genetic algorithm is a very powerful tool that, if used well, can find optimal solutions in very large parameter spaces.

The genetic algorithm starts with a random population out of all of the possible structure configurations. The best structures out of this population are taken and interbred, producing a second generation of structures; ideally, the best of this second generation are better than the best of the first generation. The process is repeated until no further improvements are seen.

For example, the parameter space could be all MDPBGs consisting of five layers of Ag alternating with six layers of Al_2O_3. The Ag layer thicknesses could range between 10 and 40 nm, and the Al_2O_3 layer thicknesses could range between 0 and 300 nm. The initial population could consist of several hundred structures where the layer thicknesses of each are chosen randomly from these ranges. The quality of the structures could be measured by the average transmittance within the wavelength range of 450 to 650 nm. This is a straightforward, though

somewhat arbitrary, example that could be used to demonstrate the utility of the genetic algorithm for metal-dielectric multilayer structures.

A more complex example might be maximizing the NLO response of a structure that contains an arbitrary number of layers of Ag, Au, Cu, SiO_2, Al_2O_3, Ta_2O_5, and TiO_2, in arbitrary order with arbitrary layer thickness. Such a feat could not easily be accomplished using the analytical techniques employed in the current research, but is within the realm of possibility for the genetic algorithm.

5.3 Summary

The NLO response of metal shows promise for applications in nonlinear absorption and sensor protection. Metal-dielectric multilayer structures such as those presented in this work provide a way to gain access to this NLO response, overcoming the challenges of absorption and reflection that severely limit the usefulness of bulk metal in this regard. These structures are able to open up transmission windows in the visible spectrum through thicknesses of metal that would otherwise be opaque. In so doing, they amplify the NLO response of the metal.

Two types of structures were considered in the present work: MDPBGs and ITFs. MDPBGs are wide pass band structures that could be used for broadband NLO purposes. ITFs are narrow band structures that have very strong responses over a limited bandwidth. Both of these structures can be optimized for either linear or NLO properties, though much work remains to be done in this area.

5.4 Publications

Peer reviewed journals

1) S.-Y. Tseng, C. Fuentes-Hernandez, D. Owens, B. Kippelen, *"Variable splitting ratio 2 x 2 MMI couplers using multimode waveguide holograms,"* Optics Express, Vol. 15, No. 14, July 2007.

2) C. Fuentes-Hernandez, S.-Y. Tseng, D. Owens, B. Kippelen, *"Ultrafast optical image processing based on third-harmonic generation in organic thin films,"* Applied Physics Letters, Vol. 91, No. 13, September 2007.

3) D. Owens, C. Fuentes-Hernandez, B. Kippelen, "*Optical properties of one-dimensional metal-dielectric photonic band-gap structures with low index dielectrics,"* Thin Solid Films, Vol. 517, No. 8, February 2009.

4) N. Djellali, I. Gozhyk, D. Owens, S. Lozenko, M. Lebental, J. Lautru, C. Ulysse, B. Kippelen, J. Zyss, *"Controlling the directional emission of holey organic microlasers,"* Applied Physics Letters, Vol. 95, No. 10, September 2009.

5) D. Owens, C. Fuentes-Hernandez, J. Hales, J. Perry, B. Kippelen, *"A Comprehensive analysis of the contributions to the nonlinear optical properties of thin Ag films, "* Accepted for publication in Journal of Applied Physics.

6) D. Owens, C. Fuentes-Hernandez, J. Hales, J. Perry, B. Kippelen, *"Nonlinear optical properties of induced transmission filters,"* Accepted for publication in Optics Express.

7) C. Fuentes-Hernandez, L. Padilha, J. Hales, D. Owens, S. Webster, J. Cho, D. Hagan, E. Van Stryland, S. Marder, J. Perry, B. Kippelen, *"Linear and nonlinear optical properties of transparent copper photonic bandgap structures,"* submitted for publication in Optics Express.

Conference papers

1) D. Owens, C. Fuentes-Hernandez, and B. Kippelen *"Aperiodic metal-dielectric optical filters*,", in *Thin-Film Coatings for Optical Applications IV* (SPIE, San Diego, CA, USA, 2007), pp. 667404.

2) C. Fuentes-Hernandez, L. A. Padilha, D. Owens, S.-Y. Tseng, S. Webster, J.-Y. Cho, D. J. Hagan, E. W. Van Stryland, S. R. Marder, and B. Kippelen, *"Linear and nonlinear optical properties of highly transmissive one-dimensional metal-organic photonic bandgap structures,"* in *Linear and Nonlinear Optics of Organic Materials VIII* (SPIE, San Diego, CA, USA, 2008), pp. 70490O.

3) C. Fuentes-Hernandez, L. A. Padilha, D. Owens, S.-Y. Tseng, S. Webster, J.-Y. Cho, D. J. Hagan, E. W. VanStryland, S. R. Marder, and B. Kippelen, *"Nonlinear refraction and absorption in highly transmissive one-dimensional metal-organic photonic bandgap structures,"* in *Conference on Lasers and Electro-Optics/Quantum Electronics and Laser Science Conference and Photonic Applications Systems Technologies* (Optical Society of America, 2008), p. CThI6

4) C. Fuentes-Hernandez, S.-Y. Tseng, D. Owens, and B. Kippelen *"Ultrafast optical image processing through non-collinear third-harmonic generation in thin organic films,"*, in *Frontiers in Optics*(Optical Society of America, 2007), p. PDP_A6.

5) D. Owens, C. Fuentes-Hernandez, J. Hales, J. Perry, B. Kippelen, "A comprehensive study of the contributions to the nonlinear optical properties of thin Ag films," accepted for presentation in *Active Photonic Materials III* (SPIE, San Diego, CA, USA, 2010).

References

1. Zhang, X., et al., Determination of two-photon-generated free-carrier lifetime in semiconductors by a single-beam Z-scan technique. Applied Physics B-Lasers and Optics, 1997. **65**(4-5): p. 549-554.

2. Zhang, X.J., W. Ji, and S.H. Tang, Determination of optical nonlinearities and carrier lifetime in ZnO. Journal of the Optical Society of America B-Optical Physics, 1997. **14**(8): p. 1951-1955.

3. Bechtel, J.H. and W.L. Smith, 2-photon absorption in semiconductors with picosecond laser pulses. Physical Review B, 1976. **13**(8): p. 3515-3522.

4. Foldvari, I., et al., Nonlinear absorption of laser light in $BiTe_2O_5$ single crystal. Optics Communications, 1993. **102**(3-4): p. 245-250.

5. Taheri, B., et al., Nonlinear absorption of laser light in $Bi_{12}GeO_{20}$ single crystals. Optical Materials, 1994. **3**(4): p. 251-255.

6. Tutt, L.W. and T.F. Boggess, A review of optical limiting mechanisms and devices using organics, fullerenes, semiconductors and other materials. Progress in Quantum Electronics, 1993. **17**(4): p. 299-338.

7. Perry, J.W., et al., Enhanced reverse saturable absorption and optical limiting in heavy-atom-substituted phthalocyanines. Optics Letters, 1994. **19**(9): p. 625-627.

8. Perry, J.W., et al., Organic optical limiter with a strong nonlinear absorptive response. Science, 1996. **273**(5281): p. 1533-1536.

9. Tutt, L.W. and A. Kost, Optical limiting performance of C_{60} and C_{70} solutions. Nature, 1992. **356**(6366): p. 225-226.

10. Chen, P.L., et al., Picosecond kinetics and reverse saturable absorption of meso-substituted tetrabenzoporphyrins. Journal of Physical Chemistry, 1996. **100**(44): p. 17507-17512.

11. Sun, Y.P. and J.E. Riggs, Organic and inorganic optical limiting materials. From fullerenes to nanoparticles. International Reviews in Physical Chemistry, 1999. **18**(1): p. 43-90.

12. Christensen, N., Band structure of silver and optical interband transitions. Physica Status Solidi B-Basic Research, 1972. **54**(2): p. 551-563.

13. Christensen, N.E. and B.O. Seraphin, Relativistic band calculation and optical properties of gold. Physical Review B-Solid State, 1971. **4**(10): p. 3321-+.

14. Rosei, R. and D.W. Lynch, Thermomodulation spectra of Al, Au and Cu. Physical Review B, 1972. **5**(10): p. 3883-3894.

15. Rosei, R., Antonang.F, and U.M. Grassano, D bands position and width in gold from very low temperature thermomodulation experiments. Surface Science, 1973. **37**(1): p. 689-699.

16. Rosei, R., Temperature modulation of optical transitions involving fermi surface in Ag - Theory. Physical Review B, 1974. **10**(2): p. 474-483.

17. Rosei, R., C.H. Culp, and J.H. Weaver, Temperature modulation of optical transitions involving fermi surface in Ag - Experimental. Physical Review B, 1974. **10**(2): p. 484-489.

18. Winsemius, P., et al., Temperature dependence of optical properties of Au, Ag, and Cu. Journal of Physics F-Metal Physics, 1976. **6**(8): p. 1583-1606.

19. Drude, P., On the electron theory of metals. Annalen Der Physik, 1900. **1**(3): p. 566-613.

20. Ordal, M.A., et al., Optical properties of the metals Al, Co, Cu, Au, Fe, Pb, Ni, Pd, Pt, Ag, Ti and W in the infrared and far infrared. Applied Optics, 1983. **22**(7): p. 1099-1119.

21. Theye, M.L., Investigation of the optical properties of Au by means of thin semitransparent films. Physical Review B-Solid State, 1970. **2**(8): p. 3060-3078.

22. Beach, R.T. and R.W. Christy, Electron-electron scattering in intraband optical conductivity of Cu, Ag, and Au. Physical Review B, 1977. **16**(12): p. 5277-5284.

23. Parkins, G.R., W.E. Lawrence, and R.W. Christy, Intraband optical conductivity of sigma(omega, tau) of Cu, Ag, and Au - contribution from electron-electron scattering. Physical Review B, 1981. **23**(12): p. 6408-6416.

24. Smith, J.B. and H. Ehrenreich, Frequency dependence of the optical relaxation time in metals. Physical Review B, 1982. **25**(2): p. 923-930.

25. Dingle, R.B., The anomalous skin effect and the reflectivity of metals .1. Physica, 1953. **19**(3): p. 311-347.

26. Aspnes, D.E., E. Kinsbron, and D.D. Bacon, Optical properties of Au - sample effects. Physical Review B, 1980. **21**(8): p. 3290-3299.

27. Parmigiani, F., et al., Optical and electrical properties of thin silver films grown under ion bombardment. Physical Review B, 1986. **33**(2): p. 879-888.

28. Holstein, T., THEORY OF TRANSPORT PHENOMENA IN AN ELECTRON-PHONON GAS. Annals of Physics, 1964. **29**(3): p. 410-535.

29. Ricard, D., P. Roussignol, and C. Flytzanis, Surface-mediated enhancement of optical phase conjugation in metal colloids. Optics Letters, 1985. **10**(10): p. 511-513.

30. Hache, F., D. Ricard, and C. Flytzanis, Optical nonlinearities of small metal particles - surface mediated resonance and quantum size effects. Journal of the Optical Society of America B-Optical Physics, 1986. **3**(12): p. 1647-1655.

31. Hache, F., D. Ricard, and C. Girard, Optical nonlinear response of small metal particles - a self-consistent calculation. Physical Review B, 1988. **38**(12): p. 7990-7996.

32. Bloemer, M.J., J.W. Haus, and P.R. Ashley, Degenerate four wave mixing in colloidal gold as a function of particle size. Journal of the Optical Society of America B-Optical Physics, 1990. **7**(5): p. 790-795.

33. Dutton, T., et al., Picosecond phase conjugate reflectivity of gold colloids by degenerate 4-wave mixing. Journal of Physical Chemistry, 1990. **94**(3): p. 1100-1105.

34. Magruder, R.H., et al., Physical and optical properties of Cu nanocluster fabricated by ion implantation in fused silica. Journal of Applied Physics, 1994. **76**(2): p. 708-715.

35. Uchida, K., et al., Optical nonlinearities of a high concentration of small metal particles dispersed in glass - copper and silver particles. Journal of the Optical Society of America B-Optical Physics, 1994. **11**(7): p. 1236-1243.

36. Puech, K., et al., Picosecond degenerate four wave mixing in colloidal solutions of gold nanoparticles at high repetition rates. Optics Letters, 1995. **20**(15): p. 1613-1615.

37. Smith, D.D., et al., Cancellation of photoinduced absorption in metal nanoparticle composites through a counterintuitive consequence of local field effects. Journal of the Optical Society of America B-Optical Physics, 1997. **14**(7): p. 1625-1631.

38. Falconieri, M., et al., Large third-order optical nonlinearity of nanocluster-doped glass formed by ion implantation of copper and nickel in silica. Applied Physics Letters, 1998. **73**(3): p. 288-290.

39. Selvan, S.T., et al., Sol-gel derived gold nanoclusters in silica glass possessing large optical nonlinearities. Journal of Physical Chemistry B, 2002. **106**(39): p. 10157-10162.

40. Liao, H.B., W.J. Wen, and G.K.L. Wong, Preparation and optical characterization of Au/SiO2 composite films with multilayer structure. Journal of Applied Physics, 2003. **93**(8): p. 4485-4488.

41. Drachev, V.P., et al., Size dependent chi((3)) for conduction electrons in Ag nanoparticles. Nano Letters, 2004. **4**(8): p. 1535-1539.

42. Wang, Q.Q., et al., Optical resonant absorption and third-order nonlinearity of (Au,Ag)-TiO2 granular composite films. Journal of Physics D-Applied Physics, 2005. **38**(3): p. 389-391.

43. Ganeev, R.A. and A.I. Ryasnyansky, Nonlinear optical characteristics of nanoparticles in suspensions and solid matrices. Applied Physics B-Lasers and Optics, 2006. **84**(1-2): p. 295-302.

44. Porel, S., et al., Optical power limiting in the femtosecond regime by silver nanoparticle-embedded polymer film. Journal of Applied Physics, 2007. **102**(3).

45. Eesley, G.L., Observation of non-equilibrium electron heating in copper. Physical Review Letters, 1983. **51**(23): p. 2140-2143.

46. Elsayedali, H.E., et al., Time-resolved observation of electron-phonon relaxation in copper. Physical Review Letters, 1987. **58**(12): p. 1212-1215.

47. Schoenlein, R.W., et al., Femtosecond studies of nonequilibrium electronic processes in metals. Physical Review Letters, 1987. **58**(16): p. 1680-1683.

48. Brorson, S.D., et al., Femtosecond room-temperature measurement of the electron-phonon coupling constant λ in metallic superconductors. Physical Review Letters, 1990. **64**(18): p. 2172-2175.

49. Tokizaki, T., et al., Subpicosecond time response of third order optical nonlinearity of small copper particles in glass. Applied Physics Letters, 1994. **65**(8): p. 941-943.

50. Ahmadi, T.S., S.L. Logunov, and M.A. ElSayed, Picosecond dynamics of colloidal gold nanoparticles. Journal of Physical Chemistry, 1996. **100**(20): p. 8053-8056.

51. Hamanaka, Y., et al., Ultrafast relaxation dynamics of electrons in silver nanocrystals embedded in glass. Journal of Luminescence, 1998. **76-77**: p. 221-225.

52. Allen, P.B., Theory of thermal relaxation of electrons in metals. Physical Review Letters, 1987. **59**(13): p. 1460-1463.

53. Carpene, E., Ultrafast laser irradiation of metals: Beyond the two-temperature model. Physical Review B, 2006. **74**(2).

54. Sun, C.K., et al., Femtosecond tunable measurement of electron thermalization in gold. Physical Review B, 1994. **50**(20): p. 15337-15348.

55. Del Fatti, N., et al., Nonequilibrium electron interactions in metal films. Physical Review Letters, 1998. **81**(4): p. 922-925.

56. Link, S., et al., Electron dynamics in gold and gold-silver alloy nanoparticles: The influence of a nonequilibrium electron distribution and the size dependence of the electron-phonon relaxation. Journal of Chemical Physics, 1999. **111**(3): p. 1255-1264.

57. Bigot, J.Y., et al., Electron dynamics in metallic nanoparticles. Chemical Physics, 2000. **251**(1-3): p. 181-203.

58. Voisin, C., et al., Ultrafast electron dynamics and optical nonlinearities in metal nanoparticles. Journal of Physical Chemistry B, 2001. **105**(12): p. 2264-2280.

59. Del Fatti, N., et al., Electron dynamics and surface plasmon resonance nonlinearities in metal nanoparticles. Chemical Physics, 2000. **251**(1-3): p. 215-226.

60. Devizis, A. and V. Gulbinas, Ultrafast dynamics of the real and imaginary permittivity parts of a photoexcited silver layer revealed by surface plasmon resonance. Applied Optics, 2008. **47**(10): p. 1632-1637.

61. Kruglyak, V.V., et al., Spectroscopic study of optically induced ultrafast electron dynamics in gold. Physical Review B, 2007. **75**(3): p. 6.

62. Rotenberg, N., et al., Nonlinear absorption in Au films: Role of thermal effects. Physical Review B, 2007. **75**(15): p. 5.

63. Del Fatti, N., et al., Nonequilibrium electron dynamics in noble metals. Physical Review B, 2000. **61**(24): p. 16956-16966.

64. Berning, P.H. and A.F. Turner, Induced transmission in absorbing films applied to band pass filter design. Journal of the Optical Society of America, 1957. **47**(3): p. 230-239.

65. Macleod, H.A., Thin-film optical filters. 3 ed. 2001, Philadelphia, PA: Institute of Physics Publishing.

66. Smith, G.B., et al., Noble metal based transparent infrared reflectors - experiments and theoretical analyses for very thin gold films. Journal of Applied Physics, 1986. **59**(2): p. 571-581.

67. Kostlin, H. and G. Frank, Optimization of transparent heat mirrors based on a thin silver film between antireflection films. Thin Solid Films, 1982. **89**(3): p. 287-293.

68. Lee, T.K., et al., Linear and nonlinear optical properties of Au-polymer metallodielectric Bragg stacks. Journal of the Optical Society of America B-Optical Physics, 2006. **23**(10): p. 2142-2147.

69. Scalora, M., et al., Transparent, metallo-dielectric, one-dimensional, photonic band-gap structures. Journal of Applied Physics, 1998. **83**(5): p. 2377-2383.

70. Bloemer, M.J. and M. Scalora, Transmissive properties of Ag/MgF2 photonic band gaps. Applied Physics Letters, 1998. **72**(14): p. 1676-1678.

71. Sibilia, C., et al., Electromagnetic properties of periodic and quasi-periodic one-dimensional, metallo-dielectric photonic band gap structures. Journal of Optics a-Pure and Applied Optics, 1999. **1**(4): p. 490-494.

72. Keskinen, M.J., et al., Photonic band gap structure and transmissivity of frequency-dependent metallic-dielectric systems. Journal of Applied Physics, 2000. **88**(10): p. 5785-5790.

73. Kloppel, A., et al., Dependence of the electrical and optical behaviour of ITO-silver-ITO multilayers on the silver properties. Thin Solid Films, 2000. **365**(1): p. 139-146.

74. Ye, Y.H., G. Bader, and V.V. Truong, Low-loss one-dimensional metallodielectric photonic crystals fabricated by metallic insertions in a multilayer dielectric structure. Applied Physics Letters, 2000. **77**(2): p. 235-237.

75. Lopez, R., et al., Pulsed laser deposition of conductive metallo-dielectric optical filters. Applied Physics a-Materials Science & Processing, 2002. **74**(2): p. 307-310.

76. Xiao, M.F., A calculation of dispersion relation K(omega) for Ag/MgF2 one-dimensional photonic band-gap structure. Materials Letters, 2002. **56**(6): p. 945-947.

77. Choi, Y.K., et al., Improved transmittance in one-dimensional metallic photonic crystals. Physica B-Condensed Matter, 2003. **338**(1-4): p. 132-135.

78. Sarto, M.S., et al., Nanotechnology of transparent metals for radio frequency electromagnetic shielding. Ieee Transactions on Electromagnetic Compatibility, 2003. **45**(4): p. 586-594.

79. Jaksic, Z., M. Maksimovic, and M. Sarajlic, Silver-silica transparent metal structures as bandpass filters for the ultraviolet range. Journal of Optics a-Pure and Applied Optics, 2005. **7**(1): p. 51-55.

80. Kee, C.S., K. Kim, and H. Lim, Optical resonant transmission in metal-dielectric multilayers. Journal of Optics a-Pure and Applied Optics, 2004. **6**(1): p. 22-25.

81. Lee, J.H., et al., Optical and structural properties of TiO2/Ti/Ag/TiO2 and TiO2/ITO/Ag/lTO/TiO2 metal-dielectric multilayers by RF magnetron sputtering for display application. Journal of the Korean Physical Society, 2004. **44**(3): p. 750-756.

82. Wang, Z.G., Q.L. Chen, and X. Cai, Metal-based transparent heat mirror for ultraviolet curing applications. Applied Surface Science, 2005. **239**(3-4): p. 262-267.

83. Wu, Y.G., et al., One-dimensional heterostructural metallodielectric photonic band gap material for the modification of emission spectrum of BaF2 scintillator. Applied Physics Letters, 2004. **85**(19): p. 4337-4339.

84. Yu, J.F., et al., Absorption in one-dimensional metallic-dielectric photonic crystals. Journal of Physics-Condensed Matter, 2004. **16**(7): p. L51-L56.

85. Sarto, M.S., et al., Nanolayered lightweight flexible shields with multidirectional optical transparency. Ieee Transactions on Electromagnetic Compatibility, 2005. **47**(3): p. 602-611.

86. Wang, Z.G., et al., Optical properties of metal-dielectric multilayers in the near UV region. Vacuum, 2006. **80**(5): p. 438-443.

87. Zhang, L.T., et al., Optical properties of a periodic one-dimensional metallic-organic photonic crystal. Journal of Physics D-Applied Physics, 2006. **39**(11): p. 2373-2376.

88. Avrutsky, I., et al., Highly confined optical modes in nanoscale metal-dielectric multilayers. Physical Review B, 2007. **75**(24).

89. Bloemer, M., et al., Broadband super-resolving lens with high transparency in the visible range. Applied Physics Letters, 2007. **90**(17).

90. Husakou, A. and J. Herrmann, Steplike transmission of light through a metal-dielectric multilayer structure due to an intensity-dependent sign of the effective dielectric constant. Physical Review Letters, 2007. **99**(12): p. 4.

91. Iwanaga, M., Effective optical constants in stratified metal-dielectric metameterial. Optics Letters, 2007. **32**(10): p. 1314-1316.

92. Lee, G.J., et al., Design, fabrication, linear and nonlinear optical properties of metal-dielectric photonic bandgap structures. Journal of the Korean Physical Society, 2007. **51**(1): p. 431-437.

93. Scalora, M., et al., Negative refraction and sub-wavelength focusing in the visible range using transparent metallodielectric stacks. Optics Express, 2007. **15**(2): p. 508-523.

94. Zhang, J.L., et al., Omnidirectional transmission bands of one-dimensional metal-dielectric periodic structures. Journal of the Optical Society of America B-Optical Physics, 2008. **25**(9): p. 1474-1478.

95. Scalora, M., et al., Optical limiting and switching of ultrashort pulses in nonlinear photonic band-gap materials. Physical Review Letters, 1994. **73**(10): p. 1368-1371.

96. Bennink, R.S., et al., Accessing the optical nonlinearity of metals with metal-dielectric photonic bandgap structures. Optics Letters, 1999. **24**(20): p. 1416-1418.

97. Scalora, M., et al., Nonlinear pulse propagation in one-dimensional metal-dielectric multilayer stacks: Ultrawide bandwidth optical limiting. Physical Review E, 2006. **73**(1): p. 016603.

98. D'Aguanno, G., et al., Accessing quadratic nonlinearities of metals through metallodielectric photonic-band-gap structures. Physical Review E, 2006. **74**(3): p. 036605.

99. Ma, G.H. and S.H. Tang, Ultrafast optical nonlinearity enhancement in metallodielectric multilayer stacks. Optics Letters, 2007. **32**(23): p. 3435-3437.

100. Ergin, T., et al., Ultrafast time-resolved spectroscopy of one-dimensional metal-dielectric photonic crystals. Physical Review B, 2009. **79**(24): p. 6.

101. Larciprete, M.C., et al., Accessing the optical limiting properties of metallo-dielectric photonic band gap structures. Journal of Applied Physics, 2003. **93**(9): p. 5013-5017.

102. Lepeshkin, N.N., et al., Enhanced nonlinear optical response of one-dimensional metal-dielectric photonic crystals. Physical Review Letters, 2004. **93**(12).

103. Du, G.Q., et al., Optical nonlinearity enhancement in heterostructures with thick metallic film and truncated photonic crystals. Optics Letters, 2009. **34**(5): p. 578-580.

104. Liao, H.B., et al., Large third-order nonlinear optical susceptibility of Au-Al2O3 composite films near the resonant frequency. Applied Physics B-Lasers and Optics, 1997. **65**(4-5): p. 673-676.

105. Boyd, R.W., Nonlinear Optics. 2 ed. 2003, San Diego, CA: Academic Press.

106. Campbell, C.T., Ultrathin metal films and particles on oxide surfaces: Structural, electronic and chemisorptive properties. Surface Science Reports, 1997. **27**(1-3): p. 1-111.

107. Anders, A., et al., Smoothing of ultrathin silver films by transition metal seeding. Solid State Communications, 2006. **140**(5): p. 225-229.

108. Lin, Z., L.V. Zhigilei, and V. Celli, Electron-phonon coupling and electron heat capacity of metals under conditions of strong electron-phonon nonequilibrium. Physical Review B, 2008. **77**(7): p. 17.

109. Groeneveld, R.H.M., R. Sprik, and A. Lagendijk, Femtosecond spectroscopy of electron-electron and electron-phonon energy relaxation in Ag and Au. Physical Review B, 1995. **51**(17): p. 11433-11445.

110. Savaloni, H. and A.R. Khakpour, Substrate temperature dependence on the optical properties of Cu and Ag thin films. European Physical Journal-Applied Physics, 2005. **31**(2): p. 101-112.

111. Groeneveld, R.H.M., R. Sprik, and A. Lagendijk, Ultrafast relaxation of electrons probed by surface plasmons at a thin silver film. Physical Review Letters, 1990. **64**(7): p. 784-787.

112. Del Fatti, N., et al., Coherent acoustic mode oscillation and damping in silver nanoparticles. Journal of Chemical Physics, 1999. **110**(23): p. 11484-11487.

113. Sigalas, M.M., et al., METALLIC PHOTONIC BAND-GAP MATERIALS. Physical Review B, 1995. **52**(16): p. 11744-11751.

114. Fan, S.H., P.R. Villeneuve, and J.D. Joannopoulos, Large omnidirectional band gaps in metallodielectric photonic crystals. Physical Review B, 1996. **54**(16): p. 11245-11251.

115. Fleming, J.G., et al., All-metallic three-dimensional photonic crystals with a large infrared bandgap. Nature, 2002. **417**(6884): p. 52-55.

116. Wood, B., J.B. Pendry, and D.P. Tsai, Directed subwavelength imaging using a layered metal-dielectric system. Physical Review B, 2006. **74**(11): p. 8.

117. Eriksson, T.S., et al., Infrared Optical-Properties of Evaporated Alumina Films. Applied Optics, 1981. **20**(15): p. 2742-2746.

118. Bayindir, M., B. Temelkuran, and E. Ozbay, Tight-binding description of the coupled defect modes in three-dimensional photonic crystals. Physical Review Letters, 2000. **84**(10): p. 2140-2143.